The
Philosophical Magazine

FIRST PUBLISHED IN 1798

A Journal of Theoretical Experimental and Applied Physics

Vol. 3 October 1958 No. 34
Eighth Series

UNIVERSITY OF HAWAII
LIBRARY
NOV 12 '58

£1 5s. 0d., plus postage
Annual Subscription £13 10s. 0d., payable in advance

ALERE FLAMMAM

Printed and Published by
TAYLOR & FRANCIS LTD
RED LION COURT, FLEET STREET, LONDON, E.C.4

THE PHILOSOPHICAL MAGAZINE

Editor

Professor N. F. Mott, M.A., D.Sc., F.R.S.

Editorial Board

Sir Lawrence Bragg, O.B.E., M.C., M.A., D.Sc., F.R.S.
Sir George Thomson, M.A., D.Sc., F.R.S.
Professor A. M. Tyndall, C.B.E., D.Sc., F.R.S.

Authors wishing to submit papers for publication in the Journal should send manuscripts directly to the Publishers.

Manuscripts should be typed in *double* spacing on one side of quarto (8×10 in.) paper, and authors are urged to aim at absolute clarity of meaning and an attractive presentation of their texts.

References should be listed at the end in alphabetical order of authors and should be cited in the text in terms of author's name and date. Diagrams should normally be in Indian ink on white card, with lettering in soft pencil, the captions being typed on a separate sheet.

A leaflet giving detailed instructions to authors on the preparation of papers is available on request from the Publishers.

Authors are entitled to receive 25 offprints of a paper in the Journal free of charge, and additional offprints can be obtained from the Publishers.

The *Philosophical Magazine* and its companion journal, *Advances in Physics*, will accept papers for publication in experimental and theoretical physics. The *Philosophical Magazine* publishes contributions describing new results, letters to the editor and book reviews. *Advances in Physics* publishes articles surveying the present state of knowledge in any branch of the science in which recent progress has been made. The editors welcome contributions from overseas as well as from the United Kingdom, and papers may be published in English, French and German.

An Uncommon Growth Feature in Diamond[†]

By A. HALPERIN [‡]
Royal Holloway College, Englefield Green, Surrey

[Received April 29, 1958]

ABSTRACT

Uncommon growth features which extend as terraces from the edges of growth sheets on octahedral faces of a diamond are described. One of these features is extraordinarily flat, probably down to atomic dimensions over its whole area (about $\frac{1}{4} \times \frac{1}{2}$ mm). From the characteristics of this feature it is concluded that in the last stage of growth of the diamond, when trigons are formed on its surface, growth sheets become frozen and growth proceeds only to the fixed edges.

§ 1. INTRODUCTION

THE object of this report is to describe an uncommon type of growth on octahedral faces of diamonds. One of the features was found to be unique with regard to some of its characteristics, and considerations as to its formation might add to our knowledge of the growth of diamond in its last stage. This feature will therefore be described in some detail.

§ 2. OBSERVATIONS

Figure 1, Pl. 67, is a high dispersion multiple-beam interferogram (Tolansky 1948) and shows a growth pyramid on one of the main faces of a ' portrait stone ' of exceptionally fine surface quality. Some results of the optical surface examination of this stone have been reported elsewhere (Omar 1953, Tolansky 1953, Tolansky and Halperin 1954). The subject of the present paper is the feature in the shape of a tongue which emerges as an extended terrace from one of the layers of the growth pyramid to the right of the figure. We shall refer to this feature as ' the terrace '.

The terrace is shown with higher magnification in fig. 2, Pl. 67, which was taken by phase contrast illumination (Zernike 1942). It consists of a very flat area surrounded to the right and on part of its upper side by a groove packed with triangular growth pits, or trigons (Sutton 1928, Halperin 1954). The vertical lines (*a*, *b*, *c*, *d* and *e*) are the edges of the growth layers of the growth pyramid. The difference between the high concentration of trigons on the surrounding surface compared with their absence on the surface of the terrace itself is very striking.

[†] Communicated by Professor S. Tolansky, F.R.S.

[‡] While on study leave. Present address : Department of Physics, The Hebrew University, Jerusalem, Israel.

Multiple-beam Fizeau fringes across this smooth feature are shown in fig. 3, Pl. 68. These are very sharp and of high precision.

A kink downwards of the fringes in fig. 3 means a descending step on the crystal surface. This was confirmed by independent interferometric methods, including that of fringes of equal chromatic order (Tolansky 1948).

Advancing from the left to the right steps down the growth pyramid. On the terrace itself, the fringe continues in a straight line except for minor small kinks at the right where some small features are present. These small features (see fig. 2) were established to be percussion figures (Tolansky and Halperin 1954). The surface of the terrace in general is flat to much better than $\lambda/200$ (5461 Å), and is probably flat down to within atomic dimensions.

On reaching the right boundary of the terrace there is an abrupt fall to a level lower than the surrounding crystal surface. This corresponds to the ' belt ' or ' trough ' surrounding the terrace (see fig. 2).

On passing this region the fringe turns up and then continues on the surface of the crystal surrounding the terrace. The trigons over which the fringes pass are clearly very shallow indeed.

An interesting fact is that each of the growth steps *a*, *b*, *c*, *d*, and *e* (fig. 2) continues from one side to the other side across the terrace. It is of special interest that the step *e* is just continued into the trough surrounding the terrace which is on a lower level (see below).

§ 3. MEASUREMENT OF STEP HEIGHTS

The sharpness of the fringes in fig. 3 permits of an accurate determination of the height of the right edge of the terrace above the general crystal level, and the depth of the trough. It is more difficult to estimate the height of the steps at the growth edges. In this case the steps are comparatively shallow and the presence of the numerous trigons gives the fringes a kinked appearance. Results are listed in the table, in which the numbers in the first column are the serial numbers of the photographic plates used for the determinations.

It may be seen from the table that the steps are of about equal height above and below the terrace, within the limits of accuracy. This is especially correct for the sum of all the five steps, the first of which (*a*) starts to the left side of the terrace, and *e* is the last step after which the level of the crystal surface to the right of the terrace is reached.

This sum which amounts in average to 1020 Å proves to be of importance when comparing with the height of the right end of the terrace above the surface level. This was also evaluated from the above-mentioned three photographs and was found to be 1050 Å, The values fit surprisingly, which shows that the surface of the terrace is in a perfect octahedral plane of the crystal, while the surrounding crystal surface deviates in the average from this orientation due to the steps. The average slope of the growth pyramid is easily obtained from the known magnification on the photograph and from the calculated step heights. It is found to amount to $2{\cdot}5 \times 10^{-4}$ rad or less than a minute of an arc.

Number of plate	Step height						Fringe
	a	*b*	*c*	*d*	*e*	sum	
145 (fig. 2)	200 Å	160 Å	210 Å	260 Å	230 Å	1060 Å	upper
101	200	180	210	200	230	1020	
127	210	180	180	250	230	1050	
Mean value	200	170	200	240	230	1040	
145 (fig. 2)	200	180	220	260	200	1060	lower
101	130	160	160	270	200	920	
127	190	180	200	270	190	1030	
Mean value	170	170	190	270	200	1000	

Note : all the numbers are given to nearest 10 Å.

The depth of the trough is found to be fairly constant compared with the *neighbouring* crystal surface, and amounts to nearly 600 Å. This includes the part of the trough between the steps *d* and *e*. Even more, the height of the step *e* itself is found to be on the bottom of the trough the same as on its upper part (which is 600 Å higher !).

A similar terrace on another crystal is shown in fig. 4, Pl. 68. This is a high dispersion multiple-beam interferogram. This was also found on an octahedral face of a fine ‘ portrait stone ’. There are, however, a few differences between the two features. The surface of this terrace, although flat compared to the stepping-down surface around, is not quite as perfect as the first terrace. The main difference, however, seems to be that there are but few trigons on the crystal surface surrounding this second terrace.

§ 4. DISCUSSION

The characteristics of the terraces and the general topography of the crystal surfaces show definitely that these are growth features, and by no means etch-figures. It seems also sure that the terrace cannot be an enclosure of small crystals or an impression of neighbouring crystal on the surface. Such effects could not result in a perfect true octahedral plane of the crystal as the surface of the terrace was shown to be.

Growth on the terrace in the final stage originated in centres on the terrace. Such growth centres are clearly seen in fig. 4, and should necessarily be assumed also for the terrace in fig. 2, the surface level of which is higher than the surrounding crystal surface (see fig. 3 ; note that even on the left side the fringe kinks slightly upwards on reaching the terrace), indicative of a growth ledge.

As to the mode of formation of the terrace, it seems that for some reason conditions were more favourable here for fast growth on the part of the advancing growth wave. Under such conditions, presumably of higher supersaturation and higher temperature, no trigons should form (Halperin 1954), and the undisturbed fast advancing growth sheets then form the terrace. If, during the piling up of growth sheets, it should happen that upper sheets fail to conform to the edge of the lower sheets, then a lower step surrounding the upper part of the terrace is left. This may be seen clearly in fig. 4.

If the level of the surrounding crystal surface reaches the level of the lower part surrounding the terrace, irregularities may be formed when the surrounding growth sheets conform with the terrace. This might explain the high concentration of trigons in the belt of the terrace in fig. 2.

The continuation in straight lines of the edges of growth sheets across the terrace (fig. 2) might be explained by assuming that at the conditions at which the surface becomes embedded with trigons, growth sheets do not advance any more, and growth proceeds only to the fixed edges. This assumption explains also why the step *e* (fig. 2) is just continued in a straight line from the crystal surface down into the groove which is on a level 600 Å lower. On the other hand conditions were probably different for the other terrace (fig. 4). In this case there were no trigons on the surface, which resulted in advance of the growth sheets in different rates in the separate sections across the terrace.

ACKNOWLEDGMENTS

I wish to express my thanks to the Hebrew University, Jerusalem for granting a study leave and to the Humanitarian Trust, London, for a Fellowship which enabled me to carry out the work. The work was carried out at Royal Holloway College under the direction of Professor S. Tolansky, and I wish to thank him for his help and assistance with the research.

REFERENCES

HALPERIN, A., 1954, *Proc. phys. Soc. Lond.* B, **67**, 538.
OMAR, M., 1953, *Thesis*, London University.
SUTTON, J. R., 1928, *Diamond* (London : Thomas Murby and Co.).
TOLANSKY, S., 1948, *Multiple-beam Interferometry of Surfaces and Films* (Oxford : Clarendon Press) ; 1953, *Research*, **6**, 8.
TOLANSKY, S., and HALPERIN, A., 1954, *Proc. phys. Soc. Lond.* B, **67**, 473.
ZERNIKE, F., 1942, *Physica*, **9**, 686.

The Decay of Neodymium-147†

By P. Rice Evans
Bedford College, University of London

[Received May 23, 1958]

Abstract

The β transitions from ^{147}Nd have been studied in the new prolate spheroidal field spectrometer. Three components of the spectrum have been separated by β–γ coincidence techniques. The γ-rays have been studied in a scintillation counter and coincidences between conversion lines and γ-rays have been recorded. On the basis of these results a new mode of decay for ^{147}Nd is proposed.

§ 1. Introduction

The β-decay of neodymium-147 is accompanied by many γ-rays and has a half-life of 11 days. At least four level schemes have been proposed for its daughter promethium-147, which also decays by a β^- transition of energy 229 kev to the ground state of samarium-147 (Agnew 1950).

Kondaiah (1951), using irradiated powder sources in the Slätis–Siegbahn spectrometer, studied the β spectrum and deduced that there were two main partial spectra with energies 350 (32%) and 780 kev (65%). From photoelectron data he noted γ-rays with energies 92, 309, 391 and 520 kev. To explain these he postulated a third β transition of energy 470 kev.

Emmerich and Kurbatov (1951), also using an irradiated source in a lens spectrometer, concluded that the β spectrum consisted of three components with energies 825, 600 and 380 kev. Rutledge *et al.* (1952) found conversion lines indicating eleven γ-rays. Recently, Hans *et al.* (1955), using scintillation counters and γ–γ coincidence techniques, have found two new γ-rays at 600 and 690 kev. They proposed a new decay scheme consistent with their results.

The present work was undertaken to seek for an unambiguous decay scheme. The isotope ^{147}Pm lies in a region where the nuclear surface deformation is relatively small (Bohr and Mottleson 1953) and thus a knowledge of the ordering of the levels may throw light on the nature of the coupled system.

§ 2. Experimental Detail

The β-rays were studied with a new large prolate spheroidal magnetic field intermediate image spectrometer (Evans *et al.* 1958). In the present work it has been used in conjunction with a scintillation spectrometer, enabling β-rays in coincidence with the selected γ-rays to be studied.

---

† Communicated by Professor H. O. W. Richardson.

A Harshaw mounted NaI(Tl) crystal ($1\frac{1}{2}$ in. × 1 in) was placed 22 mm behind the source to detect coincidence rays. This crystal subtended 12% of 4π at the source. The electronic equipment consisted of two E.M.I. 9541B 13-stage photomultipliers feeding pulses into a fast–slow coincidence circuit after Bell *et al.* (1952) and L. R. Jenkin (private communication). The resolving time employed was $2\tau = 25$ mμsec.

The β-ray source was made by distillation of $NdCl_3$ *in vacuo* on to aluminium foil of thickness 0·25 mg/cm². This foil had previously been backed with a much thinner nylon film to provide strength. By this means a thin source of diameter 9 mm was made of the fission product.

§ 3. The γ Spectrum

The crystal spectrometer was calibrated with the known γ-rays of ^{141}Ce (145 kev), ^{203}Hg (279 kev), ^{22}Na (511 kev) and ^{137}Cs (661 kev). Thus the ratio of peak to total response was found empirically and the crystal efficiencies were taken from Bell's (1955) graphs.

In the spectrum (fig. 1 and table 1) there are intense γ-rays with peaks of energies 91, 190, 275, 320, 400, 440, 530 and 685 kev. Their intensities were estimated by employing a mosaic analysis of the pulse height

Fig. 1

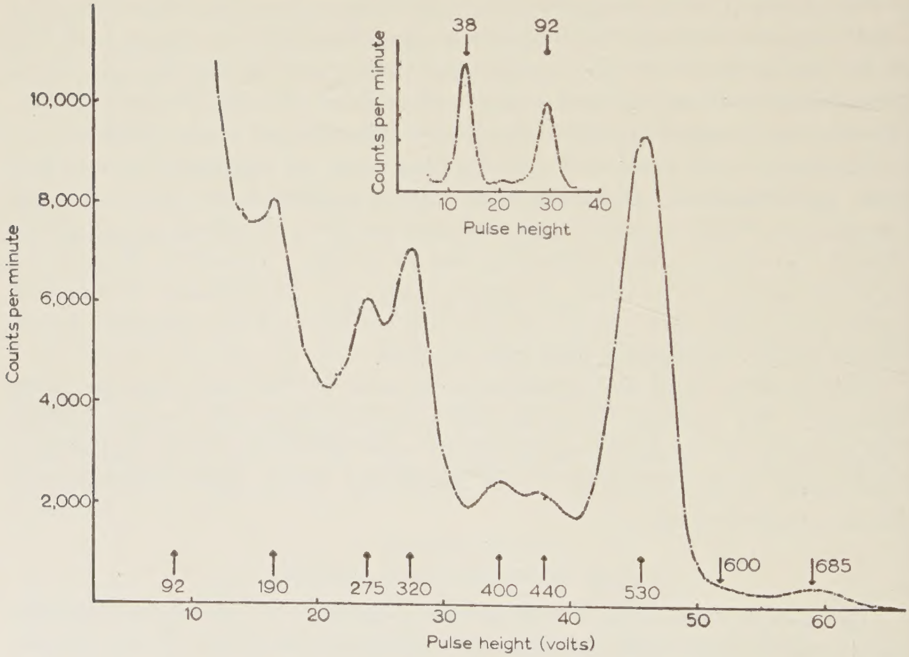

The γ-ray spectrum taken with a NaI(Tl) scintillation spectrometer. The channel width was 0·5 v and the source was 11 cm away from the crystal. The inset shows the intense 91 kev γ-ray and the 38 kev x-ray.

spectrum, the Compton and back scatter background being subtracted for each γ-ray in turn.

Table 1. The γ-Rays

Gamma ray	Estimated energy kev	Relative intensity	Conversion data of Rutledge *et al.*
K x-ray	38	160	—
γ_1	91	100	91·2 kev
γ_2	—	4·2	120·5
γ_3	190	0·9	197·1
γ_4	—	—	231·2
γ_5	—	—	259·8
γ_6	275	3·2	273·2
γ_7	—	—	300·8
γ_8	320	9·6	318·2
γ_9	400	5	398·4
γ_{10}	440	6·2	441·3
γ_{11}	530	57·0	532·2
γ_{12}	610	1·1	—
γ_{13}	685	4·3	—

The spectrum was taken with a source-crystal distance of 11 cm. γ_2 was not seen in the present work, but its intensity relative to γ_8 was calculated from the γ–γ coincidence spectra of Hans *et al.* γ_{12} was not resolved in the spectrum but its presence was noted when the spectrum was analysed.

The spectrum would agree well with that of Hans *et al.* but for the disagreement concerning γ_3. The latter authors assigned an energy of 165 kev to a small peak, similar to that shown near 190 kev in fig. 1, which we tentatively identify with a γ-ray of 197 kev whose K conversion line was found by Rutledge *et al.* This identification corresponds to a transition of about this energy between levels G and E in the energy level scheme in fig. 3. We identify the peak at about 400 kev with the 398 kev γ-ray seen by Rutledge *et al.* This is in disagreement with Hans *et al.*, who suggest it is a 409 kev transition to the ground state.

§ 4. MEASUREMENTS ON THE β SPECTRUM

The spectrometer was adjusted to give a transmission of about 1·6% at a resolution of about 2·4%. The total spectrum was recorded and the Fermi plot of the high energy region is shown by curve (*a*) in fig. (2). The end point is at 802 kev.

To separate the partial spectra, the crystal spectrometer was placed just behind the source and the pulse height analyser window adjusted to accept all pulses lying under the photoelectric peak of the required γ-ray. Thus it was possible to select only β-rays in coincidence with the chosen

γ-rays or with γ-rays of higher energy whose Compton electrons contribute to the ordinate of the peak.

The allowed Fermi plots of the various spectra are shown in fig. 2 and the results are summarized in table 2.

Fig. 2

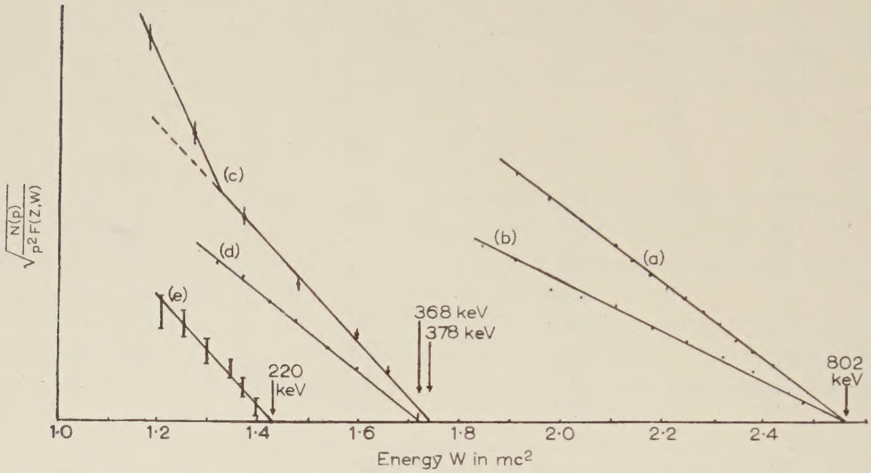

Fermi–Kurie plots. (*a*) Total spectrum, (*b*) β spectrum in coincidence with 91 kev γ-ray, (*c*) β spectrum in coincidence with 318 and 273 kev γ-ray, (*d*) β spectrum in coincidence with 530 kev γ-ray, (*e*) β spectrum in coincidence with 685 kev γ-ray.

Table 2. The Partial β-Spectra

β-ray	Maximum energy	Intensity %	log *ft*	Observations
β_1	802	76	7·4	End point of total spectrum In coincidence with 91 γ-ray
β_2	404	1·2	8·3	Postulated
β_3	362	20	6·9	In coincidence with 532 γ-ray In coincidence with 318 γ-ray Not in coincidence with 273 γ-ray
β_4	220	2·8	7·0	In coincidence with 683 γ-ray

The β spectrum appears to consist of three major components with energies 800, 370 and 220 kev. The β-ray intensities have been determined from the γ-ray intensities, assuming the veracity of the proposed energy level scheme. A weak fourth β-transition of energy 400 kev is postulated to help feed level *E* in the scheme.

The log *ft* values for the transitions were obtained with the help of Moszkowski's (1951) curves, using the β-transition intensities in table 2 in which the contribution of internal conversion to the γ-transition intensity was taken into account only in the case of the strongly converted 91 kev ray.

Coincidences between conversion lines and γ-rays were also looked for and the results are shown in table 3.

Table 3. Coincidences between Conversion Electrons Selected Magnetically and γ-Quanta Selected by Scintillation Pulse Height

1. Coincidences with the *L*-line of the 91 kev γ-ray					
Spectrometer setting	Below foot of line	On peak of line	Beyond line	Energy of selected γ-ray kev	Conclusion. Is conversion line in coincidence ?
Magnet current	1·35	1·48	1·53		
Spectrometer counting rate	1500	3900	1700		
Coincidence rate	2·5±0·4	4·5±0·5	3·3±0·4	273	Yes
,,	12·9±1	19·2±1	11·2±0·8	318	Yes
,,	—	2·4±0·2	1·0±0·2	398	Yes
,,	—	3·2±0·3	2·1±0·24	440	Yes
,,	6·2±0·6	9·0±0·9	8·8±0·9	530	No
2. Coincidences with *K*-line of 273 kev γ-ray					
Magnet current	2·60	2·67	—	—	—
Coincidence rate	1·8±0·2	1·6±0·2	—	530	No
3. Coincidences with *K*-line of 318 kev γ-ray					
Magnet current	2·80	2·98	3·1	—	—
Coincidence rate	0·32±0·08	1·67±0·3	0·11±0·05	273	Yes

To obtain an estimate of the *K* shell conversion coefficient for the 91 kev transition, the areas under the γ-ray and x-ray peaks on the scintillation spectrum were compared (fig. 1). A correction of about 12% was made for the pre-absorption in Perspex and aluminium. Bergstrom's (1955) values for the fluorescence yield and Davisson's (1955)

γ-ray absorption coefficients were used. The small unknown contribution to the x-ray peak by other transitions was neglected. The value obtained for the K shell coefficient was $K = 1{\cdot}6 \pm 0{\cdot}2$, which coincides with the value given by Hans *et al.* (1955).

We adopted the value 6·88 found by Smith and Mitchell (1952) for the $K/L+M$ ratio, in order to determine the intensity of the 91 kev transition to the ground state. From these values it would appear that the 91 kev transition is magnetic dipole.

§ 5. The Decay Scheme

The nine quanta seen in the present study, together with the four extra seen by Rutledge *et al.* have been fitted into a scheme of six excited levels (fig. 3). At least three of these levels are fed by β-rays.

Fig. 3

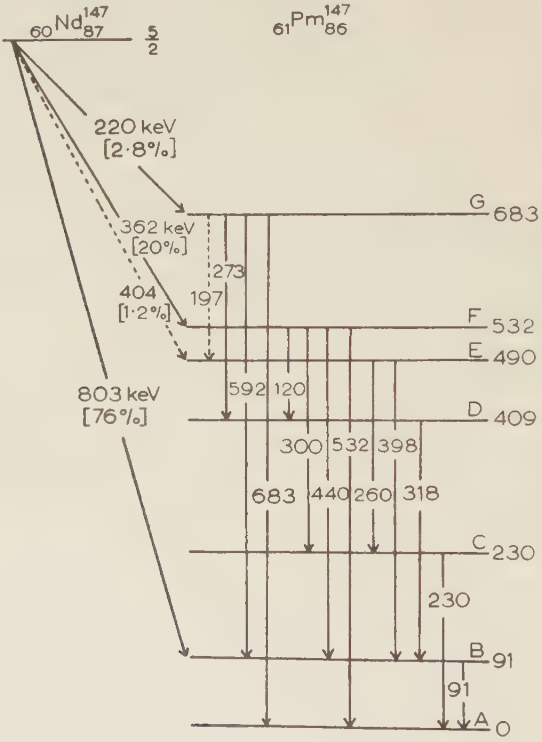

The proposed decay scheme.

The absence of a β^- transition to the ground state has been noticed by previous workers. Here also we find that the energy end points measured in the Fermi analysis of the total spectrum and of the spectrum in coincidence with the 91 kev γ-ray are the same. For intensity reasons this γ-ray can only go to the ground state of ^{147}Pm.

The level *C* at 230 kev is fixed solely by the energy measurements of Rutledge *et al.* It appears to be fed by the 260 and 300 kev γ-rays from levels *E* and *F*.

The level *D*, also located at 410 kev by Hans *et al.*, is a well-populated level but it is not fed by β rays. It de-excites to level *B* by emission of the 320 kev quantum, which is in coincidence with that of 91 kev. Level *D* is fed by the 273 kev and 120 kev γ transitions from levels *G* and *F*. The former ray is shown in table 3 to be in coincidence with the 320 kev conversion electron, whilst the 120 kev γ-ray, which is normally unresolved in the complete pulse height spectrum, has been shown by Hans *et al.* also to be in coincidence with the 320 kev γ-ray.

Level *E* is postulated to explain coincidences which were obtained between the 398 kev γ-ray and the *L* conversion line of the 91 kev transition. The energy combination $231{\cdot}2 + 259{\cdot}8 = 491$ also suggests a level at 491 kev.

Level *F* is fed by a β transition of energy 362 kev, whilst level *G* is justified by the presence of the 685 kev γ-ray which, according to fig. 1, is in coincidence with a β decay of energy 220 kev. We suggest that the 610 kev γ-ray de-excites this level going to the first excited state and is therefore of 592 kev. The 273 kev quantum, which has been shown to be in coincidence with the 320 kev γ-ray, must also be emitted from the level *F*. As already stated, it seems likely that the 197 kev γ-ray is a transition from level *G* to level *E*, although the energy fit is not exact.

§ 6. DISCUSSION

Little can be said of a definite nature concerning the spins and parities of the excited levels in ^{147}Pm until the intensities of the internal conversion lines be further studied.

Agnew (1950) has shown that there is a first forbidden, allowed shape, β transition from ^{147}Pm to the ground state of ^{147}Sm. Since this ground state has been measured to be $\frac{7}{2}$ by spectroscopic measurements (Murakawa 1954) and by paramagnetic resonance methods (Bogle and Scovil 1952), the possible spins for the ground state of ^{147}Pm are $\frac{5}{2}$, $\frac{7}{2}$ or $\frac{9}{2}$. Recently, Kedzie *et al.* (1957) have deduced, from paramagnetic resonance measurements, a spin of $\frac{5}{2}$ for the ground state of ^{147}Nd. The additional evidence in the present paper supports the conclusion of previous workers that the 91 kev γ transition from the first excited level is predominantly M1 and the *ft* value also indicates that the β transition to the first excited level is first forbidden.

With these results it is difficult to explain the absence of a β transition to the ground state. The possibility of an *l* forbidden transition seems unlikely since the odd neutron concerned with the ground state of ^{147}Nd probably lies in the $f\,\frac{7}{2}$ shell.

It is of interest to note that the ratio of the energies of the 273·3 and 120·5 γ rays is 2·267, which is close to the ratio 2·285 predicted for a rotational band with spins $\frac{5}{2}$, $\frac{7}{2}$ and $\frac{9}{2}$. Further, it is known (Bohr and

Mottelson 1955) that the experimental values are slightly less than the predicted ratios due to vibration–rotation interactions.

With this interpretation, the most likely spin for the ground state of ^{147}Nd would be $\frac{11}{2}$. This would be possible according to Nilsson's (1955) calculations of the independent particle energy levels in a spheroidal field for a nuclear deformation (δ) of about 0·2. However, this is contrary to expectation, since an $\frac{11}{2}$ state is considered unlikely for pairing energy reasons.

In conclusion, although it would seem that the energies of the proposed levels in ^{147}Pm are well founded, little is known of their spins. If the ground state spin values of $\frac{5}{2}$ and $\frac{7}{2}$ are accepted for ^{147}Nd and ^{147}Sm, it would appear that there is an unknown selection rule influencing the β transition probabilities.

ACKNOWLEDGMENTS

It is a great pleasure for me to thank Professor H. O. W. Richardson for his advice and generous encouragement. I am indebted to Bedford College for the provision of sustentation during the course of this work. Finally, I would like to acknowledge the interest taken by Mr. N. J. Freeman, Dr. D. K. Butt and Dr. I. R. Williams.

REFERENCES

AGNEW, H., 1950, *Phys. Rev.*, **77**, 655.
BELL, P. R., 1955, *Beta and gamma spectroscopy* (Ed. K. Siegbahn), p. 154.
BELL, R. E., GRAHAM, R. L., and PETCH, H. E., 1952, *Canad. J. Phys.*, **30**, 35.
BERGSTROM, I., 1955, *Beta and gamma spectroscopy*, p. 630.
BOGLE, G. S., and SCOVIL, H. E. D., 1952, *Proc. phys. Soc. Lond.* A, **65**, 368.
BOHR, A., and MOTTELSON, B., 1953, *Dan. Mat. Fys. Medd.*, 27, No. 16 ; 1955, *Beta and gamma spectroscopy*, p. 487.
DAVISSON, C. M., 1955, *Beta and gamma spectroscopy*, p. 857.
EMMERICH, W. S., and KURBATOV, J. D., 1951, *Phys. Rev.*, **83**, 40.
EVANS, P. R., FREEMAN, N. J., MCGINTY, G. K., ARMITAGE, B. H., and RICHARDSON, H. O. W., 1958 (to be published).
HANS, H. S., SARAF, B., and MANDEVILLE, C. E., 1955, *Phys. Rev.*, **97**, 1267.
KEDZIE, R. W., ABRAHAM, M., and JEFFRIES, C. D., 1957, *Phys. Rev.*, **108**, 54.
KONDAIAH, E., 1951, *Phys. Rev.*, **81**, 1056.
MOSZKOWSKI, S. A., 1951, *Phys. Rev.*, **82**, 35.
MURAKAWA, K., 1954, *Phys. Rev.*, **93**, 1232.
NILSSON, S., 1955, *Dan. Mat. Fys. Medd.* 29, No. 16 *and Phys. Rev.*, **99**, 1615.
RUTLEDGE, W. C., CORK, J. M., and BURSON, S. B., 1952, *Phys. Rev.*, **86**, 775.
SMITH, A. B., and MITCHELL, A. C. G., 1952, *Phys. Rev.*, **87**, 1128.

The Use of Magnetic Models in the Interpretation of Domain Effects on an Electron Beam†

By M. BLACKMAN and N. D. LISGARTEN
Physics Department, Imperial College, London, S.W.7

[Received May 28, 1958]

ABSTRACT

A magnetic unit has been constructed which consists of an array of oppositely magnetized steel wires and its effect on an electron beam has been studied. The phenomena observed are similar to the domain effects found when magnetic crystals are examined in the same apparatus, and are used in interpreting some of the features of the domain effects.

§ 1. INTRODUCTION

IT has been shown by Germer (1942) that a high voltage electron beam can be employed to investigate the magnetic leakage fields near the surface of a cobalt crystal. Recently, Blackman and Grünbaum (1956, 1957), using a refined version of this technique, were able to demonstrate the existence of magnetic domains in cobalt in a very direct manner. Investigations of single crystals of hematite and magnetite using the electron technique have also been carried out by Blackman *et al.* (1957).

One of the methods used to show the domain effects was to form a shadow of the crystal using a divergent electron beam, the axis of the cone of divergent rays being approximately parallel to the face of the crystal investigated. The magnetic leakage field distorts the geometrical shadow and the edge of this then becomes a ' pattern ' of more or less periodic cycloidal character. This phenomenon was interpreted (Blackman and Grünbaum 1956, 1957) in terms of the effect of a linear array of magnetic poles on an electron beam. This simple assumption gave satisfactory semi-quantitative results in that the cycloidal nature of the pattern followed ; also the magnitude of the domain spacings in hexagonal cobalt agreed with that found using the magnetic powder method. The magnetic shadow patterns found in magnetite and hematite can also be interpreted in the same way, though there are at present no independent measurements of the size of the magnetic regions in these crystals.

It still remains, however, to be explained why the picture of a linear array of poles gives such a satisfactory explanation. If one considers the magnetic effects associated with the hexagonal face of cobalt, for instance, one would expect that domains of a type similar to those near the edge would also exist in the face itself. The same considerations would also be expected to apply in the cases of hematite and magnetite. It would seem that the effect of domains in the face of the crystal is less important than in those near the edge.

---

† Communicated by the Authors.

To investigate this point, it was decided to construct a model consisting of an assembly of small bar magnets which would give a satisfactory representation of the magnetic features of a finite two-dimensional array of magnetic domains. The model was roughly of the same size as that of the crystals normally used and its magnetic effects on the electron beam were investigated in the same way as with a crystal. The model did in fact show magnetic patterns of the same type as those obtained with the crystals.

§ 2. CONSTRUCTION AND USE OF THE MODEL

A number of lengths, each about 1 cm long and $\frac{1}{2}$ mm diameter, were cut from a coil of steel wire. Each separate length was placed in a magnetic field of about 10 000 oersted, with its axis parallel to the direction of the field. To ensure satisfactory uniformity of magnetization, each length of wire was mounted on a wooden jig so as to occupy a position mid-way between the pole-pieces of an electromagnet, and each was allowed to remain in the field for the same time.

The magnetized wires were then mounted in rows on strips of adhesive tape, each row having 15 wires arranged with unlike poles adjacent. The rows of wires were then packed together within a rectangular brass frame so that the poles were arranged in a square array, the poles being of alternate kind along rows and columns. This arrangement allowed for the examination of either a single row or any number of rows up to a maximum of fifteen. Thus the full array contained 225 wires. The model with 12 rows is shown in fig 1†.

The model was mounted in the specimen holder of an electron diffraction camera ; the arrangements for observing the magnetic shadow patterns were similar to those previously described for experiments on hematite and magnetite (Blackman *et al.* 1957). As in these experiments, the electron beam was either parallel to, or made a small angle with, one of the faces of the model containing the array of poles, and was approximately perpendicular to the axes of the wires.

The shadow patterns obtained with a single row and with two rows of magnetized wires are shown in figs. 2 (*a*) and 2 (*b*). Here the arrangement was such that a line linking the poles in any one row would be perpendicular to the electron beam. The pattern obtained from an assembly of 12 rows each containing 15 wires is shown in fig. 2 (*c*).

The effect of rotating the single-row and two-row assemblies through 90° about an axis parallel to the axes of the magnetized wires is shown in figs. 3 (*a*) and 3 (*b*). The pattern shown in fig 3 (*a*) is similar to that found with a single magnetized wire and the pattern of fig. 3 (*b*) to that with two adjacent wires with their poles in opposite directions. In the case of the extensive assembly, referred to above, patterns were photographed for a number of positions during the rotation and several of these are shown in fig. 4. The first pattern (0°) was obtained when the electron beam was parallel to one of the sides of the (rectangular) assembly. It can be seen that the number of the periodic features of the pattern increases as the angle of rotation approaches 45° and then decreases. The number at 90° is not the same as that at 0°—as it would be if the number of poles in rows and columns were equal. It can also be seen that the spacing is less regular for the 90° position than for the 0° position. On further rotation the patterns repeat in that the number of periodic features are the same, but there are differences in details.

---

† All figures are Plates.

Departures from a completely regular arrangement of poles can be observed in the model. The model consists of a set of rows in each of which the magnetic wires are firmly fixed in position ; any irregularity in the arrangement of wires in a row position will also lead to an irregularity in the spacing between neighbouring poles in a direction perpendicular to the row. For the initial position (0°), the electron beam was parallel to the directions of the rows and this gives the most regular pattern. The less regular patterns obtained for the setting of the model 90° from the intial position can be associated with the deviations from the regular spacing of the poles in each row. Similarly, differences which are observed in patterns for equivalent orientations of the model can also be associated with such imperfections.

Apart from the small disturbances due to irregularities in arrangement, the patterns show a number of periodic magnetic features ; this number is a minimum in the 0° position and a maximum in the neighbourhood of the 45° position. Observations were also made with an arrangement in which magnets were situated only on the periphery. This assembly (of 17 by 15 magnets) proved to be sufficiently rigid inside the brass frame. Figures 5 (*a*), 5 (*b*) and 5 (*c*) show the 0°, 45° and 90° positions. It will be seen that the magnetic effects are essentially the same as those for a complete model ; this shows that the peripheral magnetic field is chiefly responsible for the magnetic effects produced by the complete model when the arrangement is regular or very nearly so.

The effect of a pronounced irregularity was investigated in the following manner. A middle row of an extensive model (12 by 15 magnets) was changed for one in which the spacing between the magnets was increased by replacing some of the magnets by copper wires of the same diameter. The actual stacking arrangement in the row was

S C N C S C C N C C S C N C S,

where S refers to a magnet with its south pole, N to a magnet with its north pole, on the face to be examined, and C to a copper wire. The magnetic pattern with the electron beam parallel to the face of the specimen is shown in fig. 6 (*a*). The features are now characteristic of the modified row and not of the edge of the model. When the glancing angle of incidence of the electron beam was increased, the pattern changed progressively to that characteristic of the edge (figs. 6 (*b*), 6 (*c*), 6 (*d*)). For comparison, a corresponding set of experimental results on a regular model is shown in fig. 7.

Another informative experiment which can be carried out with the regular models is one in which the distance between the axis of the electron beam and the face is varied, the axis of the beam being kept parallel to the face of the crystal. As the distance is increased from its normal value, the magnetic features diminish in magnitude, the cycloidal curves becoming progressively undulatory (see fig. 8). The same effect be achieved by increasing the height of the brass housing instead of moving the beam relative to the model; in this way it was found that the magnetic effects became inappreciable at a distance of about 1 mm above the face, i.e. roughly equal to the period of the spacing of the magnetic poles on the face of the model.

When the beam is brought so close to the surface that an appreciable part of the divergent cone is intercepted, additional features are found (fig. 9). The general background also produced by the electrons is now much more prominent and a series of points (or streaks) of enhanced intensity appear. Some of these are definitely associated with the cusps on the magnetic pattern and move in a regular fashion as the model is rotated.

§ 3. Summary and Discussion

From the experiments with an extensive and a peripheral model (figs. 4 and 5) it can be concluded that the main magnetic features in the electron shadow patterns which are periodic in character are due to the fringe magnetic field. It follows that the effect of those magnets of an extensive model which are not on the periphery are small compared with those on the edge. Hence the magnetic field above the surface must fall off appreciably faster with distance from the surface for regions on the face of the model as compared with regions on the edge of the model.

A large departure from a regular packing, e.g. by doubling the spacing between neighbouring magnetic poles in a particular region of the model, does produce a local magnetic field sufficiently extensive to affect the pattern. That the effect is, however, local and of limited extent is shown by its disappearance when the angle of incidence of the electron beam is changed (see fig. 6).

The above results show that the interpretation originally given for the magnetic patterns observed using the hexagonal face of cobalt (Blackman and Grünbaum 1956, 1957) is essentially correct. This interpretation was based solely on the assumption of a fringe magnetic field. The present experiments show that the results on cobalt are consistent with a regular arrangement of domains on the hexagonal face with a spacing period approximately equal to that given by the shadow pattern. A similar interpretation can be given for the patterns from magnetite and hematite (Blackman *et al.* 1957). In hematite, however, the patterns found appeared to be in general less regular and correspond in fact to the 'weak field' effect shown in fig. 8. In more recent work on hematite crystals from Elba, much more regular shadow patterns have been obtained which are characteristic of a relatively higher remanent magnetization.

The 'strong field' effects which are observed when an appreciable part of the divergent beam is affected by the magnetic field of the model (fig. 9) have not been observed with the magnetic iron oxides, but do appear in the case of cobalt (Blackman and Grünbaum 1958), an example being shown in fig. 10.

The behaviour of the shadow pattern when the model is rotated at glancing incidence (fig. 4) provides an instructive example of the influence of the whole fringe field on the electron beam ; the extra features come in at well defined angles as the model is rotated from the 0° position to the 45° position. A change of the angle of incidence has a marked effect (except near the symmetrical positions 0°, 45°, 90° etc.) since at higher angles of (glancing) incidence the electrons interact only with a part of the fringe field and not with the whole fringe field. In the symmetrical positions the magnetic effects overlap so as to produce practically the same pattern at all angles of incidence where the magnetic effects are appreciable.

The change in the spacing of the periodic features in the shadow patterns when the model is rotated (fig. 4) shows that care has to be exercised in deducing the spacing of the regular arrangement from these shadow patterns. When the spacing is reasonably regular, the pattern giving the largest period can be used to give the spacing of the poles on the surface. Irregularities can, however, be important in practical cases and a large series of rotation patterns would be needed before the spacing on the surface could be assessed. The rotation experiments might also have to be supplemented by others in which the angle of incidence is varied. The values obtained from experiments on crystals such as hematite or magnetite would be the projection of the spacing of the magnetic regions on the surface and would be *larger* than the actual value, except in the case where the magnetic axis is perpendicular to the surface.

REFERENCES

BLACKMAN, M., and GRÜNBAUM, E., 1956, *Nature, Lond.*, **178,** 584; 1957, *Proc. roy. Soc.* A, **241,** 508; 1958, *Ibid.*, **245,** 408.

BLACKMAN, M., HAIGH, G., and LISGARTEN, N. D., 1957, *Nature, Lond.*, **179,** 1288.

GERMER, L. H., 1942, *Phys. Rev.*, **62,** 295.

The Cleavage Surfaces of Type I and Type II Diamonds†

By Eileen M. Wilks
The Clarendon Laboratory, Oxford

[Received May 20, 1958]

Summary

The cleavage surfaces of 75 type I and 75 type II diamonds have been examined using microscopy and multiple-beam interferometry. The work confirms an earlier qualitative observation that the surface of a type II diamond exhibits a more regular cleavage pattern. There are in general, more cleavage lines on type I diamonds, and also a greater number of the so-called river systems. The results suggest that impurities within the lattice lead to a more broken substructure in the type I diamonds. It is also shown that birefringence and counting properties are not appreciably reflected in the cleavage patterns, and that very few type II diamonds show evidence of a laminated structure.

§ 1. Introduction

Many investigations have been made on the differences between type I and type II diamonds, but apart from the work of Halperin (1956) which showed that the density of trigons is less on type II diamonds, little has been done on the various surface features of the two types. However, we have previously noted that a type II diamond had a more regular cleavage pattern than a type I (Wilks 1952, Tolansky 1953) and this has subsequently been confirmed by Seal (1956). In the present paper we report a systematic study of the cleavage surfaces of type I and type II diamonds. Robertson *et al.* (1934) originally classified diamonds into two types depending on whether their absorption edge in the ultra-violet was at 3000 Å or 2250 Å. Although this classification is not entirely adequate, see for example Clark *et al.* (1956), it is still a useful criterion with which other physical properties such as infra-red absorption, thermal conductivity and counting efficiency may be correlated, and we shall therefore use this classification.

Diamond cleaves very readily along the octahedral planes; and although other cleavage planes have been reported (Sutton 1928, Ramaseshan 1946), they are not very common. An attempt to cleave diamond along one of these other planes was unsuccessful, so only (111) planes have been studied in the present investigation. On commencing the work it soon became apparent that the cleavage surfaces of both type I and type II industrial diamonds are so complex that it is impossible to compare their characteristics in any quantitative manner; the surfaces are very irregular, many regions show evidence of conchoidal fracture, and the overall impression is merely one of imperfection. However, gem quality diamonds exhibited more ordered cleavage patterns, and significant differences between the two types could be detected, therefore all the stones examined in detail were of good quality. The cleavage surfaces were obtained by cleaving octahedral diamonds in the usual way (e.g. Grodzinski 1944); in all, about 75 cleavage surfaces of each type were examined. Of these 25 of each type were studied in detail; a thin layer of silver about 500 Å thick was evaporated on to the surfaces, which were then examined using microscopy and multiple-beam interferometry (Tolansky 1948).

---

† Communicated by Professor Tolansky, F.R.S.

§ 2. General Cleavage Characteristics

Figures 1–4, Pls. 73–74, show typical examples of cleavage surfaces obtained from both types of stone; figs. 1 and 2 are a photomicrograph and interferogram respectively of a type I diamond and figs. 3 and 4 are similar pictures for a type II diamond. The surfaces are covered by a network of cleavage lines and the resulting patterns are rather complex. However, a comparison of figs. 2 and 4 clearly shows that the cleavage patterns of type I stones are more complicated and the quality of the Fizeau fringes more variable than on type II diamonds. It may also be noted that the patterns of even type II stones are more complicated than those of several other crystals such as mica, selenite and calcite (Tolansky 1948).

The quality of the Fizeau fringes is more variable over type I surfaces because there are usually several prominent cleavage lines such as A in fig. 1 which may be several microns wide. The steps associated with these lines are responsible for a considerable variation in fringe definition, thus the definition is good on one side of A but poor on the other. As fringes of some definition could usually be obtained over the entire cleavage surface, it may be estimated that these lines separate surfaces whose levels differ by the order of 10–50 microns. On type II stones there are fewer such cleavage lines; on the surface of the stone shown in fig. 3, there are none at all, and the fringe definition is good over almost the whole surface (fig. 4). There are occasionally steps as high as 1/10 mm on type II stones, for example XY on fig. 3; they are usually near an edge and are probably connected with the initiation of cleavage.

An attempt was made to assess these differences more quantitatively by examining in greater detail 20 surfaces from 10 stones of each type. Straight lines were drawn over representative areas and a count made of the number of prominent cleavage steps which they crossed. It was thus found that the linear concentration of the prominent cleavage lines was four times greater on type I stones than on type II.

On examining the parts of the surfaces bounded by prominent cleavage lines it was seen that they contain regions in which lesser cleavage lines run more or less parallel to each other, and the average area of these regions is about three times greater on type II stones. These regions were examined by constructing cross sections approximately at right angles to the cleavage lines over a total distance of 2·5 mm, on four representative stones of each type. The height of each cleavage step was measured with Fizeau fringes, and fig. 5 shows a histogram of the number of steps with a given height. (Step heights of less than 100 Å are omitted, because the overall complexity of the type I stones limited the accuracy of measurement to 50 Å.) The results show that there are about three times as many steps greater than 500 Å on the type I stones. The mean distance between the cleavage lines with step heights greater than 500 Å is of the order of 15 and 40 microns for type I and type II stones respectively. On the other hand there does not appear to be any significant difference in the number of steps of height less than about 500 Å.

Fig. 5

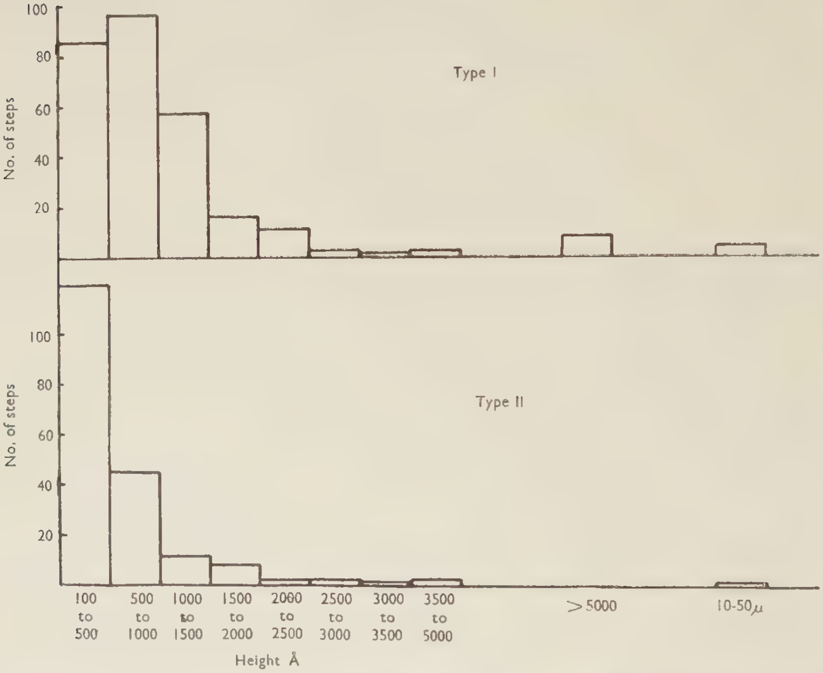

Histogram of the number of cleavage steps in equivalent distances on type I and type II diamonds.

§ 3. The Cleavage Lines

As is seen in figs 1 and 3 the general pattern of the cleavage lines resembles the 'river systems' characteristic of both amorphous and crystalline substances (Zapffe and Worden 1949 a and Keis *et al.* 1950), and are more curved on type I stones. The step height along a given cleavage line is not constant; thus the height along the line B on the type I stone whose interferogram is shown in fig. 6, Pl. 75, varies from zero to 2800 Å over a distance of 1·0 mm, while on the type II stone shown fig. 7, Pl. 75, the height along the line Z falls from 1100 Å to zero in a distance of 0·4 mm. In both cases it follows that the surfaces on either side of the cleavage lines are inclined to each other; the angular inclination being of the order of one minute of arc.

A quite common feature on the cleavage surfaces of both type I and type II diamonds is visible in figs. 8 and 9, Pl. 76. Figure 8 shows the surface of a stone (a type II diamond) in which a system of river lines breaks out from a line boundary in the upper part of the picture, and subsequently coalesces into a fewer number of more pronounced lines. Several rather similar systems are seen in fig. 9 (a type I diamond), although the boundaries marking the commencement of the lines are not so sharply defined. These patterns quite closely resemble cleavage systems observed by Zapffe and Worden (1949 b) in ammonium dihydrogen phosphate and by Pratt (1956) in sodium chloride. As has been discussed by several authors (Fisher 1954, Pratt 1954, Gilman 1955 and Hirsch 1956), such groups of river lines may be associated with the presence of a twist boundary between adjacent sub-grains of the crystal; each line being initiated by screw dislocations emerging in the surface.

Although recent work by Gilman (1957) and Forty (1957) shows that the stress around the tip of a cleavage crack in crystalline materials may initiate plastic flow and produce dislocations, it seems unlikely that any plastic flow will be introduced into diamonds by the cleavage process. Hence the surface pattern will be determined by the defects and dislocations already present in the crystal prior to cleavage. In this connection it may be noted that the variation of step height along a cleavage line implies misorientations between sub-grains of the diamond and therefore the presence of twist boundaries.

Two variants of the above type of behaviour have also been observed. In fig. 10, Pl. 77 (a type I diamond) where the cleavage has passed from the top of the picture to the bottom, a system of river lines is initiated in the left centre of the picture, but instead of beginning on one boundary as in the previous photographs, it commences on a series of parallel boundaries which are clearly visible. Pratt (private communication) has remarked that the wedge shaped mark on fig. 8 shows some resemblance to features observed on cleaved surfaces of zinc, which are believed to arise from twinning caused by plastic flow subsequent to cleavage. The line boundary in fig. 11, Pl. 77 is also suggestive of local twinning; evidence that such may be the case has been given by Pandya and Tolansky (1954) who observed the effect of etch on these lines. The markings on zinc are not reflected on the opposite cleavage face and this is usually taken as evidence that plastic flow occurred after cleavage (Pratt 1953). However, all the present markings on diamond are reflected, in particular the line in fig. 11 is reflected as one of a series of thin dark lines crossing the opposite face (line E in fig. 1), so that any twinning must have been present in the stone initially.

Several workers have observed groups of cleavage lines on type II diamonds which are both straight and parallel; it has been suggested that type II stones are laminated (Robertson *et al.* 1934, Ramachandran 1946, Custers 1951, Pandya and Tolansky 1954), the straight lines being traces of the planes dividing lamallae of more perfect crystal. However, it is not at all clear what would give rise to such a structure, although Champion (1953) has proposed that the planes separating lamellae contain an excess concentration of impurity atoms. In the present work no sets of straight lines were observed on any type I stone. Out of the 75 type II surfaces examined only two from the same stone and one from another (a counter) showed such systems, and then only over a fraction of their area (fig. 12, Pl. 78). The spacing of these lines varied from about 5 microns to 30 microns; these figures being in agreement with the values given by the previously mentioned workers. On one of these surfaces the steps were almost of constant height (about 1000 A) for the order of 1 mm, and on the other two the heights were much smaller, 50 A or less; there is no obvious correlation of these lines with any other property of the stones.

§ 4. THE SURFACES OF COUNTING AND BIREFRINGENT DIAMONDS

Nine of the diamonds examined showed conduction properties under the influence of ionizing radiations; six were type II with moderate to good counting efficiency, the other three were type I with low counting efficiency. In general, the cleavage characteristics of these stones were not significantly different from non-counting type I and type II diamonds. There was, however, one exception. One of the type II counters (a stone of 1 ct) exhibited a series of parallel cleavage lines; these extended over about 1 mm^2 of its surface (fig. 13, Pl. 78); an interferogram of this region (fig. 14, Pl. 78) shows that the step height associated with these lines is no more than 50 A. Two of the counting stones which had absorption spectra intermediate between a type I and a type II, exhibited cleavage surfaces which had some regions typical of type I stones and others typical of type II stones. This is in accord with electron microscope studies by Seal (1956), and with a deduction of Ahearne (1954) based on the counting properties of 'mixed' stones.

The effect of birefringence on the cleavage properties was also studied by examining six surfaces from strongly birefringent stones and six surfaces from non-birefringent stones. One of the birefringent diamonds contained a prominent inclusion, which was probably responsible for the birefringence; cleavage had occurred so that the inclusion stood out as a projection on one of the surfaces, and there was a corresponding hole on the other surface. Except for this feature there was no obvious difference between the cleavage patterns exhibited by the birefringent and non-birefringent stones, which were all typical examples of type I cleavage. Thus, if impurities are responsible for the differing cleavage patterns, they are not usually sufficiently concentrated to produce a visible strain in the lattice.

§ 5. Discussion

It has been shown that there is a marked difference between the cleavage surfaces of type I and type II diamonds, those of type I being more complex and irregular. It is usually assumed that the essential difference between type I and type II stones is that the former contain a greater concentration of impurities (Sutherland *et al.* 1954). Hence, the fact that cleavage lines with step heights greater than about 500 Å are more common on type I stones, suggests that the steps are associated with a localized concentration of impurities. On the other hand, a consideration of fig. 1 suggests that a considerable part of the complexity of a type I cleavage pattern arises from the generation of river systems of the kind shown in figs 9 and 10, and these appear to be associated with screw dislocations rather than with impurity atoms. Thus it would appear that the impurities in a type I stone lead to a more disordered system of sub-grains, and hence to a greater concentration of dislocations in the boundaries.

A rather similar conclusion has been reached by Halperin (1956) who showed that there is a greater density of trigons on the natural faces of type I than on those of type II diamonds. This again suggests a greater density of screw dislocations emerging in the surface of the type I stones. Also we have recently observed on each surface of a pure octahedron gem stone groups of trigons which are geometrically related to an inclusion in the centre of the crystal (Frank *et al.* 1958). The position of the trigons suggests that they arise from dislocations whose common origin is in the strained region surrounding the inclusion. At present there is not much evidence as to the difference in the impurity content of type I and type II diamonds, but an analysis of the combustion products of several diamonds suggests that the concentrations may differ by about a factor 10 (Raal, 1957). Unless the distribution of the impurities within the crystal is known, it is hardly possible to relate this figure with the linear concentration of the cleavage steps, but the figures are at least not inconsistent. As cleavage lines with step heights less than about 500 Å occur in about equal numbers on both types of stones, they cannot readily be associated with the impurity content. Rather they must be due to some other form of lattice defect common to all diamonds, possibly in the form of dislocation networks.

It has also been shown that any birefringence and counting properties of the diamonds are not appreciably reflected in the cleavage patterns. The surfaces seldom give evidence of a strongly laminated structure, although the most striking example of such a structure was observed in a counting diamond where it has previously been suggested that such a structure might be expected (Champion 1953).

Acknowledgments

I would like to thank Industrial Distributors (Sales) Limited for the loan of the diamonds and for a research grant. I also wish to thank

Dr. F. C. Champion and Mr. W. F. Cotty for their cooperation concerning the counting diamonds.

My thanks are also due to Professor S. Tolansky, F.R.S. (in whose laboratory this work was first started) and to the late Sir Francis Simon, F.R.S., for their interest and encouragement.

REFERENCES

AHEARNE, A. J., 1954, *Phys. Rev.*, **96,** 828.
CHAMPION, F. C., 1953, *Proc. roy. Soc.* A, **220,** 485.
CLARK, C. D., DITCHBURN, R. W., and DYER, H. B., 1956, *Proc. roy. Soc.* A, **234,** 363.
CUSTERS, J. F. H., 1951, *Research*, **4,** 131.
FISHER, J. C., 1954, *see* BILBY, B. A., and SMITH, E., 1956, *Acta Met.*, **4,** 379.
FORTY, A. J., 1957, *Proc. roy. Soc.* A, **242,** 392.
FRANK, F. C., PUTTICK, K., and WILKS, E. M., 1958 (to be published).
GILMAN, J. J., 1955, *Acta Met.*, **3,** 277; 1957, *Trans. Amer. Inst. min.* (*metall.*) *Engrs*, **209,** 449.
GRODZINSKI, P., 1944, *Miner. Mag.* **27,** 186, 47.
HALPERIN, A., 1956, *Acta cryst., Camb.*, **9,** 265.
HIRSCH, P. B., 1956, *Progr. metal Phys.* **6,** 236.
KEIS, J. A., SULLIVAN, and IRWIN, G. R., 1950, *J. appl. Phys.*, **21,** 716.
PANDYA, N. S., and TOLANSKY, S., 1954, *Proc. roy. Soc.* A, **225,** 40.
PRATT, P. L., 1953, *Acta Met.*, **1,** 692; 1954, *See* BILBY, B. A., and SMITH, E.; 1956, *Ibid.*, **4,** 379; 1956, Unpublished work quoted in *Progr. metal Phys.*, **6,** 268.
RAAL, F. A., 1957, *Amer. Miner.*, **42,** 354.
RAMACHANDRAN, G. N., 1946, *Proc. Indian. Acad. Sci.* A, **24,** 65.
RAMASESHAN, S., 1946, *Proc. Indian Acad. Sci.* A, **24,** 114.
ROBERTSON, R., FOX, J. J., and MARTIN, A. E., 1934, *Phil. Trans.* A. **232,** 463.
SEAL, M., 1956, *Proc. Stockholm Conf. on Electron Microscopy*, 341.
SUTHERLAND, G. B. B. M., BLACKWELL, D. E., and SIMERAL, W. G., 1954, *Nature Lond.*, **174,** 901.
SUTTON, J. R., 1928, *Diamond* (London).
TOLANSKY, S., 1948, *Multiple Beam Interferometry of Surfaces and Films* (Oxford) 1953, *Research*, **6,** 8.
WILKS, E. M., 1952, *Ph.D. Thesis*, London.
ZAPFFE, C. A., and WORDEN, C. O., 1949 a, *Acta cryst., Camb.*, **2,** 377; 1949 b, *Ibid.*, **2,** 383.

On the Escape of Impurities from Solids†

By ROBERT ENGLMAN
H. H. Wills Physics Laboratory, University of Bristol

[Received June 19, 1958]

ABSTRACT

It is shown how the distribution of impurities in a semi-infinite solid may be determined from observations of the escape-rate across the surface. The results are applicable to other diffusion processes.

§ 1. INTRODUCTION

THE object of this paper is to propose a method for determining the distribution of impurities (ions or atoms) in a crystal by the measurement of their rate of escape. The basic result is given by eqn. (5), which represents an explicit expression for the original distribution $f(x,0)$ in terms of $(\partial/\partial t)N(t)$ the rate of change of the total number of impurities. The practically minded reader may well wish to omit the mathematical reasoning of § 3.2 leading up to eqn. (5) and concentrate on § 5, where we discuss some practical problems related to the interpretation of experimental data.

Before we turn to our main object it is essential to discuss some aspects of the diffusion of impurities out of a semi-infinite crystal across a plane boundary surface.

§ 2. DIFFUSION ACROSS A BOUNDARY

2.1

The mechanism which is responsible for the large scale movement of impurities consists in jumps across distances of the order of crystal spacings (~ 1 Å). For our purposes there is no need to specify *how* these jumps occur. The reason for this as regards the interior of the crystal is a matter of common knowledge : Owing to the minute distances and very great frequencies (say, 10^7 per second) of the jumps we can afford to treat the large scale movements of the impurities by the diffusion approximation. In this approximation the details of the mechanism enter into the expression for the probability of the displacement of the impurity over a given distance and time interval only through the coefficient of diffusion D. It is basic to what follows, that the value of D (or better : the diffusion coefficient corresponding to the drift of impurities in a direction normal to the surface) be known for the crystal studied. This value will best be found empirically. Experimental methods for determining the diffusion coefficient, as well as its theoretical meaning, were reviewed by Lidiard (1957).

---

† Communicated by the Author.

2.2

To discuss the effect of the boundary we must in the first instance return to the microscopic description. We regard the surface layer of atomic sites (let these be denoted by $r=0$) as perfectly absorbing, if the chance of the return of an impurity into the body of the crystal (i.e. to layers labelled by the integers $r>0$), at any step after reaching the surface layer, is nil. For a perfectly reflecting boundary the same probability is one and for a partially absorbing one a value intermediate between these two.

We now require the probability $P_n(r'\rightarrow r)$ that an impurity initially at r' will, after n jumps and in the presence of the boundary, reach the layer r. If we disregard jumps within layers and count only those which bring the particle from one layer to another, then our problem becomes essentially one dimensional. We consider the impurities performing in the interior an uncorrelated random walk with equal probabilities ($\frac{1}{2}$) for the forward and backward steps. Let ϵ be the probability that the particle after reaching the boundary layer will escape and $1-\epsilon$ the probability that the next step of the particle is inwards.

For this model the required probability $P_n(r'\rightarrow r)$ has been obtained by Shenton (1955). Our interest in his results is limited to the range where the total number of jumps is enormously larger than the net number of lattice layers traversed by the particle. (This means that $|r-r'|/n \ll 1$ and, of course, defines the validity of the diffusion approximation.) A saddle point integration of his formula (6) leads to the result for the probability (not normalized)

$$P_n(r'\rightarrow r) \simeq \exp\left[-\frac{(r-r')^2}{2n}\right] - \frac{(1-2\epsilon)\exp[2(r+r')/n]-1}{(1-2\epsilon)-\exp[2(r+r')/n]}\exp\left[-\frac{(r+r')^2}{2n}\right]. \quad . \quad . \quad (1)$$

Here the first term is the familiar probability corresponding to an infinite medium. The second term arises from the presence of the boundary.

Now, in the case under consideration, $(r+r')/n$ will tend to zero and the fraction in the second term will, for any $\epsilon \neq 0$, tend to *one*, with it. (More exactly, the criterion for this limit is that $(r+r')/n \ll \epsilon$.)

For $\epsilon=0$ we have the case of a perfectly reflecting boundary. Then the fraction tends to -1 as $(r+r')/n$ tends to zero.

The gross meaning of these results is that for the purposes of diffusion across a surface we may, after an initial lapse of time, regard any surface, other than those nearly perfectly reflecting, as a perfectly absorbing boundary. The quantitative restrictions implicit in this statement, which are those stated in the brackets above, will be discussed later. Bearing these restrictions in mind and applying ourselves to such situations that the probability of the impurities leaving the surface is not too low (this probability may effectively be controlled by the temperature), we shall write the fraction in (1) as 1.

2.3

The following intuitive argument makes the conclusions of the previous section clearer.

Consider once again a particle starting a random walk from the lattice layer r. Supposing for a moment that the boundary is perfectly reflecting, we ask how many times does the particle hit the boundary in n jumps? It may be shown that for very large n, and when also r^2 is of the order, or less than, n, the number of collisions with the boundary is of the order $\sqrt{n}$. Bearing in mind that the particles from the rth layer arrive predominantly when $n \gtrsim r^2$, we can say that the imperfectly absorbing character of the boundary may be ignored if $\epsilon\sqrt{n} > 1$.

This carries the corollary that, whereas for particles arriving from depths greater than ϵ^{-1} layers the character of the boundary makes no essential difference, the escape of particles starting from shallower depths than that will be restricted by the boundary.

§ 3. THE DISTRIBUTION DENSITY

3.1

So far we have treated the migration of individual impurities in microscopic terms. We now introduce the macroscopic measures x and t of distance and time and the initial distribution density $f(x, t=0)$. We find, by virtue of the discussion of the previous paragraph, the following integral relation for the distribution density at any time t, subject to the condition $f(0,t)=0$.

$$\begin{aligned} f(x,t) &= \frac{1}{\sqrt{2\pi Dt}} \int_0^\infty f(x',0) \left\{ \exp\left[-\frac{(x-x')^2}{2Dt} \right] - \exp\left[-\frac{(x+x')^2}{2Dt} \right] \right\} dx', \\ &= \frac{1}{\sqrt{2\pi Dt}} \int_{-\infty}^{\infty} \exp\left[-\frac{(x-x')^2}{2Dt} \right] f(x',0)\, dx', \qquad \ldots\ldots \quad (2) \end{aligned}$$

where $f(x,0) = -f(-x,0)$.

This is of course the well-known solution of the problem of diffusion in a semi-infinite medium in terms of a mirror distribution of diffusing 'holes' (Carslaw and Jaeger 1948). We treat here the converse problem, the determination of $f(x,0)$ from experimentally measurable quantities. The tools needed for the derivation of the results are the theory of the Fourier and Mellin-transforms and the Wiener–Hopf technique for integral equations. An account of these is given in Titchmarsh's (1937) book. (We do not claim, though, to maintain the standard of rigour set in that book.)

3.2

For the sake of convenience in the proof we assume that for large $|x|$, $f(x,0) = [\exp(-\alpha|x|)]$, $\alpha > 0$. Then the Laplace transform of $f(x,t)$

$$N(u,t) = \int_0^\infty dx \exp(xu) f(x,t)$$

is regular for all u, such that $\operatorname{Re} u < \alpha$, and tends to zero for $\operatorname{Re} u \to -\infty$.

We now write down the bilateral Laplace transform of eqn. (2). Using the Faltung rule and writing $F(u)$ for the bilateral Laplace transform of $f(x,0)$, we find easily

$$N(u,t) - N(-u,t) = \exp(\tfrac{1}{2}Dtu^2)F(u).$$

The crux of the problem is how to separate $N(u,t)$ and $N(-u,t)$.

We note now that the regions of regularity of these two functions together cover the whole complex plane and, moreover, have a strip in common. Laurent's theorem, as applied to the common strip of regularity $-\alpha < \operatorname{Re} u < \alpha$, allows us to find $N(u,t)$; in fact

$$N(u,t) = \frac{1}{2\pi i}\int_{c-i\infty}^{c+i\infty} \exp(\tfrac{1}{2}Dtw^2)F(w)\frac{dw}{w-u},$$

where c is in the strip and greater than $\operatorname{Re} u$.

Differentiating with respect to time, and putting $u=0$, we get $(\partial/\partial t)N(0,t) \equiv \dot{N}(t)$ which is minus the rate of escape of particles across unit surface. This is

$$\dot{N}(t) = \frac{D}{4\pi i}\int_{c-i\infty}^{c+i\infty} \exp(\tfrac{1}{2}Dtw^2)wF(w)\,dw$$
$$= \frac{D}{2\pi i}\int_0^\infty \exp(-\tfrac{1}{2}Dtv^2)vF(iv)\,dv \quad . \quad . \quad . \quad . \quad . \quad (3)$$

after a simple change of the path of integration and because the integrand is even.

We take now the Mellin transform of this equation. Then

$$M(s) = \int_0^\infty t^{s-1}\dot{N}(t)\,dt$$
$$= \frac{D}{2\pi i}\int_0^\infty v^{1-2s}F(iv)\,dv\left(\frac{2}{D}\right)^s\Gamma(s)$$

since

$$\int_0^\infty t^{s-1}\exp(-\tfrac{1}{2}Dt)\,dt = (2/D)^s\Gamma(s).$$

Cross-multiplying and using the Mellin inversion formula, we find

$$v^2F(iv) = \int_{c'-i\infty}^{c'+i\infty} (\tfrac{1}{2}D)^{s-1}\frac{M(s)}{\Gamma(s)}v^{2s}\,ds. \quad . \quad . \quad . \quad . \quad (4)$$

$F(iv)$ may be inverted by the Fourier sine transform theorem. Explicitly

$$f(x,0) = \frac{1}{\pi i}\int_0^\infty dv \sin xv \int_{c'-i\infty}^{c'+i\infty} ds(\tfrac{1}{2}v^2D)^{s-1}\frac{1}{\Gamma(s)}\int_0^\infty t^{s-1}\dot{N}(t)\,dt, \qquad (5)$$

where c' may be chosen at will.

It is also true that this solution is the only one which has the postulated asymptotic behaviour. We have thus established the existence of a unique solution of the specified form. Actually the restriction that $f(x, 0) = O[\exp(-|\alpha n|)]$ was introduced only to achieve simplicity in the proof. The final result (5) can be shown to hold good under much less restrictive conditions, in fact for practically any situation that may be of physical interest.

§ 4. A SIMPLE EXAMPLE

We briefly illustrate now the result for a simple case, when the initial distribution function is the Dirac delta $\delta(x-a)$. The escape rate corresponding to this distribution is to be found from (2). It may be verified that

$$\dot{N}(t) = -\frac{a}{\sqrt{2\pi D}}\, t^{-3/2} \exp(-a^2/2Dt).$$

The Mellin transform of this is $-\pi^{-1/2}(2D/a^2)^{1-s}\Gamma(\frac{3}{2}-s)$.

Substituting into eqn. (4), we see that

$$F(iv) = -\frac{4}{\sqrt{\pi}} \int_{-i\infty}^{i\infty} 2^{-2s}(av)^{2(s-1)} \frac{\Gamma(\eta - s)}{\Gamma(s)}\, ds.$$

To evaluate this integral we bend the path of integration round so that the contour encircles all the poles of $\Gamma(\frac{3}{2}-s)$, namely, $s = \frac{3}{2}+m$, where m is zero or a positive integer. Summing all residues we see that

$$F(iv) = 2i \sin av,$$

which is the sine transform of the delta function, as required.

§ 5. EXPERIMENTAL CONSIDERATIONS

5.1

The implication of eqn. (5) is clear. Given $\dot{N}(t)$ as an analytic function or a continuous curve, the function $f(x, 0)$ can be found by repeated integrations to any desired degree of accuracy. The integrations will best be performed by numerical means : the values of $\Gamma(s)$ for complex arguments will be found in one of the references (N.B.S.C.L.) given at the end of the paper.

It will be noted that $1/\Gamma(s)$ diverges as $|s|$ tends to infinity along a line parallel to the imaginary axis. The convergence of the integration over s in (5) will be ensured by the factor $M(s)$. To convince ourselves that this is so under fairly representative conditions, we have in fact calculated the integrand for an exponentially decreasing distribution of impurities and found that the modulus of the integrand decreases exponentially as $s \to \pm i\infty$. Even if this is not the case, as for example for the delta function distribution of the previous paragraph where the integrand in question oscillates finitely as $s \to \pm i\infty$, we can save the situation by a judicious change of the path of integration. Thus in the case of §4 we displace the path of integration from the imaginary axis to two rays in the fourth and first quadrants of the complex plane respectively, taking care that no pole of the integrand is crossed by this displacement. The integral of §4 now converges rapidly and there should also be no difficulty in carrying out the corresponding integration numerically.

5.2

In practice, the limitations to the straightforward applications of the formula are threefold. First, the crystal even if it be regarded as of infinite extent laterally will have a finite depth (say, of magnitude L). Even if the farther surface is considered closed or reflecting, the conditions of diffusion will be different from those in an infinitely deep medium. This will then set an upper limit to the useful duration of observations, this limit being the characteristic time of arrival of the impurities from the far end, namely $L^2/2D$.

The second restriction arises from the inexactness of the boundary condition $f(0,t)=0$ or of the assumption of a perfectly absorbing boundary. Referring to the discussion in §2 and noting that the majority of particles will arrive from the r'th lattice place to the boundary in about r^2 jumps, we see that measurements should only be taken after a time corresponding to

$1/\sqrt{n}<$ (the probability of the particle leaving the crystal after reaching the boundary layer).

(The wide variety of possible experimental situations hardly allows us to be more specific than this.)

5.3

Finally we take account of the fact that in any experiment a finite number of readings will be taken. The question is now what is the best timing of these observations between the two limits already established, which will result in the most faithful curve for the initial distribution.

Briefly, the answer is that the observations should be uniformly distributed on a $t^{-1/2}$ scale of time. The following plausible reasoning may be presented in support of this.

To any term $A_m \sin(m\pi x/2L)$ in the distribution curve there will correspond a term

$$A_m \frac{D\pi m}{4L} \exp\left(-\frac{D}{8}\frac{\pi^2}{L^2}m^2 t\right)$$

in the empirical curve and *vice versa*. This may be proved from various formulae of §3, but can be obtained most simply from the result

$$f(x,0)=\frac{1}{i\pi}\int_0^\infty dv \sin xv \int_{c'-i\infty}^{c'+i\infty} dt\dot{N}(t)\exp\left(\tfrac{1}{2}Dv^2t\right),$$

which in turn follows from (3) and is a variant of (5).

Now any arbitrary $f(x, 0)$ corresponding to a crystal of finite depth L may be Fourier analysed into

$$\sum_m A_m \sin \frac{m\pi}{2L}, \qquad m = 1, 2, 3, \ldots .$$

Moreover, the first M of the infinite terms will also yield a good approximation (in a well-defined sense) to the distribution curve. We may therefore use the M available readings to determine the first M coefficients A_m. (This argument seems reasonable, though we have not really proved, for example, the existence of a unique solution for a medium of finite depth.)

We now make the plausible assumption about A_m that *a priori* they are all of the same order of magnitude (and do not, say, increase exponentially with m). Then suppose that M readings of $\dot{N}(t)$ are taken so that we have M equations to solve for A_m

$$\dot{N}(t_l) = \frac{D\pi}{4L} \sum_m m A_m \exp(-m^2 t_l), \qquad l = 1, 2, \ldots M$$

with t_l in units of $8L^2/\pi^2 D$.

Suppose now that t_l is so arranged as to be monotonically decreasing with l and also that $\dot{N}(t_l)$ does not change too radically with l. Then consideration of the leading terms in the inverse matrix of the above system of equations shows that after a few m's

$$\frac{m\,.\,A_m}{1\,.\,A_1} \propto \exp(m^2 t_m - t_1).$$

A reasonable way of ensuring that $m\,.\,A_m$ does not increase with m is that we take

$$t_m \propto 1/m^2,$$

or that readings are taken uniformly on the $t^{-1/2}$ scale.

The conclusions that we draw from this argument are that, if by a Fourier analysis of a distribution of depth L we want to discern irregularities of the order $2L/\pi M$, a rational choice is to make at least M observations, starting at a time $8L^2/\pi^2 D M^2$ and continuing until $8L^2/\pi^2 D$ with a distribution of observations proportional to $t^{-1/2}$. Arguing that the result will not be strongly dependent on the method of calculation, one concludes that the same procedure is a reasonable one for the use of formula (5) as well. It is not suggested that a least square fitting of a sum of exponentials possesses any obvious advantage over direct numerical integration of formula (5).

Finally we note that excluding readings before t_M rules out in effect the Fourier components whose wavelengths are less than about $\sqrt{Dt_M}$.

ACKNOWLEDGMENTS

My colleague, Dr. K. P. Sinha, very kindly drew my attention to this topic. I am grateful to senior members of the Department (Dr. D. Bohm, Dr. R. G. Chambers and Professor F. C. Frank) for devoting their time to discussion of this paper and to the Referee for valuable suggestions.

REFERENCES

CARSLAW, H. S., and JAEGER, J. C., 1948, *Conduction of Heat in Solids* (Oxford: Clarendon Press).

LIDIARD, A. B., 1957, *Handbuch der Physik*, XX (Berlin: Springer-Verlag), p. 245.

SHENTON, L. R., 1955, *Proc. Camb. phil. Soc.*, **51**, 442.

TITCHMARSH, E. C., 1937, *Theory of Fourier Integrals* (Oxford: Clarendon Press).

N.B.S.C.L. *Table of Gamma Functions for Complex Arguments.* (N.B.S. Appl. Math. Series, No. 34, U.S. Gov. Printing Office.)

The Ductile–Brittle Transition in the Fracture of α-Iron : I†

By N. J. Petch
Metallurgy Department, Houldsworth School of Applied Science,
University of Leeds

[Received March 5, 1958]

Abstract

A criterion for the transition in fracture mode from ductile to cleavage is calculated for fracture at a notch. It is concluded that the temperature-dependence of this transition probably arises more from that of the Peierls–Nabarro stress required to move a free dislocation in a α-iron than from the temperature-dependence of the locking of a dislocation source. The transition temperature is found to be a function of grain size, the friction on a free dislocation, the strength of the dislocation locking, the degree of triaxiality of the applied stress and the elastic constants.

§ 1. Introduction

Two distinct types of fracture are known for α-iron. Brittle fracture occurs at lower temperatures and ductile fracture at higher temperatures. The transition between the two is fairly sharp and the transition temperature, which in fracture from a notch occurs around room temperature. is of very great technological importance, since it indicates the susceptibility of the steel to catastrophic brittle fracture in service.

In the change from ductile to brittle, two transitions should really be distinguished (Parker 1957). There is the transition in the energy consumed in taking the specimen from the unstrained to the fractured condition and the transition in the appearance or mode of fracture. This second refers to the change from the matt ductile fracture to the bright 'crystalline' appearance produced by cleavage of the individual crystals. The present paper refers mainly to this transition in mode of fracture in impact tests on notched specimens.

In recent years, it has been suggested that in polycrystals both types of fracture originate in cracks produced by the high stresses generated at the head of a pile-up of dislocations against a grain boundary (Zener 1948, Mott 1953, 1956 a, b, Petch 1953, 1954, 1956, Stroh 1954, 1955 a, b, 1957). The formation of these cracks may possibly take place by coalescence of the dislocations in the pile-up. It has further been suggested that cleavage occurs when the fracture stress can propagate the cracks produced by the dislocations as Griffith cracks, so that break-out of the fracture across the grain takes place. On the other hand, in ductile fracture, it is thought that the dislocation cracks cannot propagate in this way, so further

---

† Communicated by the Author.

deformation with the production of further small cracks is necessary until eventually the bridges between these give way and they link together into a major crack. Thus, it is thought that the distinction between ductile and cleavage fracture lies in the propagation of the dislocation cracks and that the ductile to cleavage transition occurs when the ductile fracture stress becomes capable of Griffith propagation of a dislocation crack.

Very recently, Cottrell (private communication) has suggested that the initial cracks may form by coalescence of dislocations on intersecting slip planes rather than on one slip plane. For the purpose of the present paper, it makes little difference which mechanism actually operates.

One factor in the stress required for Griffith propagation of a dislocation crack is the effective surface energy associated with the extension of the crack. This term consists of the true surface energy and the plastic work done by the crack as it extends. The amount of this plastic work is related to the number of dislocation sources operated by the passage of the crack, so the weaker the dislocation locking, the greater the plastic work term and the more difficult is Griffith propagation.

Stroh (1955 b, 1957) has developed a theory of the ductile–brittle transition on this basis. As the temperature is raised, the operation of sources becomes easier and Stroh considers that the transition temperature occurs when there is a rapid change in the number of sources operated by the crack. However, this leaves unexplained some known features of the transition, so a new calculation is attempted in the present paper. In this, it is shown that the temperature-dependence of the transition in fracture mode probably arises more from that of the stress required to move a free dislocation than from the temperature-dependence of the dislocation locking.

§ 2. THE CRITERION FOR THE DUCTILE–CLEAVAGE TRANSITION

Consider the fracture of a notched specimen such as used in the Izod or Charpy impact tests. The transition in mode of fracture from fully ductile to fully cleavage occurs over a range of temperature and is closely merged with the energy transition. Within this temperature range, the fracture is first ductile near the notch, but changes to cleavage as it advances. It is thought that this happens as the fracture gathers speed and moves into a region of greater triaxiality of stress. Thus, the essential condition for the occurrence of cleavage in these tests seems to be that the fracture stress ahead of an advancing ductile fracture should eventually become capable of Griffith propagation of a dislocation crack produced in this location†.

Suppose a crack is wedged open by n' dislocations on a slip plane that makes an angle θ with the crack. The components of the applied stress normal and parallel to the crack are σ_1 and σ_2 respectively. Stroh (1957) has shown that the applied stress will cause this crack to spread if

---

† The Robertson (1953) test is somewhat different. It is concerned with the change of a cleavage fracture into a ductile one. Because of the greater velocity of a cleavage crack, this change should occur at a somewhat higher temperature than the initiation of cleavage ahead of a ductile fracture.

$$n'\mathbf{b}\{(\sigma_1{}^2+\sigma_2{}^2)^{1/2}+\sigma_1 \sin\theta\}=4\gamma', \qquad (1)$$

where **b** is the Burgers vector and γ' is the effective surface energy associated with the growth of the crack.

Let σ be the tensile stress where a dislocation crack forms ahead of the advancing ductile fracture. A triaxial tension will be generated at this location, so let $q\sigma$ be the uniaxial stress equivalent to σ for the production of shear stress. For simplicity, suppose that the operative slip plane and direction are at 45° to σ and that the dislocation crack is normal to it (fig. 1). This is fairly close to what may happen with slip on {110} and cleavage on {100}.

Fig. 1

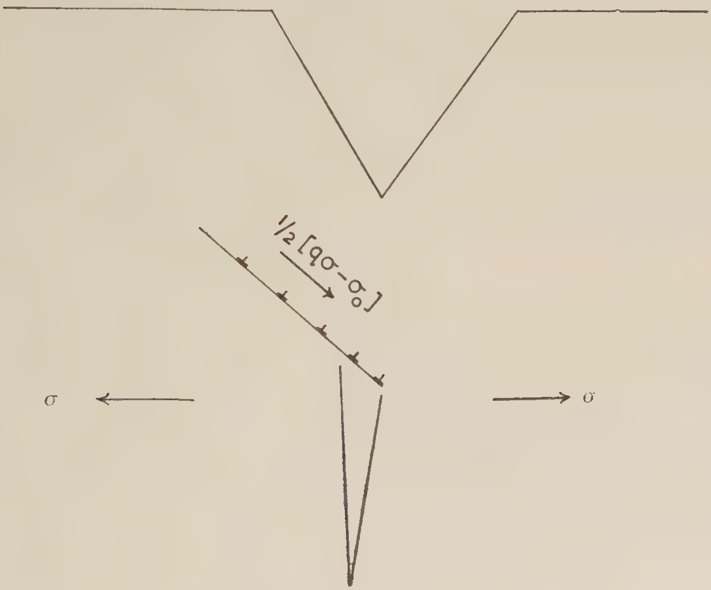

The formation of a crack.

Then, from (1), the dislocation crack will spread if

$$n'\mathbf{b}\sigma(1+1/\sqrt{2})=4\gamma'. \qquad (2)$$

The next question is the value of n'. Dislocation sources in α-iron are operated in highly localized stress concentrations. Also, the movement of a free dislocation on a glide plane is opposed by a friction that requires a shear stress $\frac{1}{2}\sigma_0$ to overcome it. Thus, in fig. 1, dislocations will not be able to leave the region of high stress at the source to move along the glide plane if the back shear stress near the source is $\frac{1}{2}(q\sigma-\sigma_0)$.

This back stress is produced by the dislocations on the glide plane and by the dislocation crack. Now, the most difficult step in the coalescence of dislocations is the coalescence of the first two of them (Stroh 1955 a) and the stress required to add subsequent dislocations falls progressively. Thus, eventually, the number of dislocations held on the glide plane will be small and the back stress will be mainly due to the dislocation crack.

Taking the back shear stress at a source half the grain diameter l away from the crack as $\mu n'\mathbf{b}/\pi(1-\nu)l$ (Stroh 1955 a), where μ is the rigidity modulus and ν is Poisson's ratio, and supposing that cracks form at both ends of the slip plane, the number of dislocations that can be fed into a crack before dislocation movement down the slip plane is arrested is given by

$$\tfrac{1}{2}(q\sigma-\sigma_0)=2\mu n'\mathbf{b}/\pi(1-\nu)l,$$

or

$$n'=\pi(1-\nu)(q\sigma-\sigma_0)l/4\mu\mathbf{b}. \quad . \quad . \quad . \quad (3)$$

From Eshelby *et al.* (1951), this is the same number of dislocations as can be packed into a length $\frac{1}{2}l$ by an applied shear stress $\frac{1}{2}(q\sigma-\sigma_0)$.

Consider now the value of σ. With un-notched α-iron specimens, the strain for ductile fracture is nearly independent of grain size and the fracture stress σ_f is given by

$$\sigma_f=\sigma_0+k^*l^{-1/2}, \quad . \quad . \quad . \quad . \quad . \quad . \quad . \quad . \quad (4)$$

where k^* is a constant (Petch 1956). This ductile fracture stress is at least approximately a shear stress criterion (Zener 1948, Dorn 1948), so in the present case we put

$$q\sigma=\sigma_0+k^*l^{-1/2}. \quad . \quad . \quad . \quad . \quad . \quad . \quad . \quad (5)$$

Equation (4) is similar in form to the lower yield point equation

$$\sigma_{\mathrm{l.y.p.}}=\sigma_0+kl^{-1/2}. \quad . \quad . \quad . \quad . \quad . \quad . \quad . \quad (6)$$

This equation arises because the propagation of the yield point involves the unlocking of dislocation sources by the concentrated stress ahead of a pile-up of dislocations against a grain boundary and σ_0 in it is the friction on a free dislocation at the yield point. Since the fracture stress in (4) is also the flow stress at the fracture strain and flow after the yield point presumably still involves the operation of sources in regions of stress concentration, the similarity between (4) and (6) suggests that σ_0 in (4) represents friction on a free dislocation at fracture. This will be greater than the yield point value because of the strain-hardening prior to fracture. Experimentally, it is observed that increasing the friction by lowering the temperature to −115°C (Petch 1956, Heslop and Petch 1956) or by quench-ageing (Midgley and Petch, unpublished), which treatments have little effect on the fracture strain, increases σ_0 at fracture by very nearly the same amount as the increase in σ_0 at the lower yield point.

From (2), (3) and (5), it follows that the ductile fracture will change to cleavage if

$$\sigma=16\mu\gamma'/\pi(1-\nu)(1+1/\sqrt{2})k^*l^{1/2}, \quad . \quad . \quad . \quad . \quad (7)$$

or

$$\sigma\simeq 4\mu\gamma'/k^*l^{1/2}.$$

With smaller values of σ, the dislocation cracks cannot spread and the fracture will remain ductile.

If the cracks form by coalescence of the dislocations on intersecting slip planes, there will be a small difference in the numerical factor in this expression.

Rewriting with (5), the condition for change to cleavage is

$$\sigma_0 \simeq \left(\frac{4q\mu\gamma'}{k^*} - k^*\right) l^{-1/2}. \qquad \ldots \ldots \quad (8)$$

It is useful to consider how the various factors in this cleavage criterion exert their influence.

Increase in grain size favours cleavage because the number of dislocations wedging the dislocation crack open is greater, so the crack is easier to propagate, eqn. (2). This is, however, partly compensated for by the lower fracture stress available for propagation, eqn. (5).

The spread of a dislocation crack depends upon the tensile stress at fracture, eqn. (2), whereas the ductile fracture stress involves a resultant shear stress. Thus, factors that increase the tensile stress relative to the resultant shear stress favour cleavage. The friction stress σ_0 and the factor q are in this category, eqn. (5).

Increase in the effective surface energy γ' favours ductile fracture, since the break-out of the dislocation crack becomes more difficult, eqn. (2). Such an increase in γ' will arise if the dislocation locking is weakened, because more dislocation sources will then be operated by the concentrated stress at the tip of the growing crack.

§ 3. THE TRANSITION TEMPERATURE

Temperature-dependence comes into the transition criterion (8) mainly through γ' and σ_0. An increase in temperature increases γ' by weakening the dislocation locking and decreases σ_0, and both these changes favour ductile fracture.

Experimental evidence suggests that the temperature-dependence of σ_0 is more important than that of γ' in the transition temperature of notched specimens.

Previous work has shown that the friction on a free dislocation in α-iron has a temperature-independent part σ_0^* and a temperature-dependent part $\sigma_0^\dagger$. The former arises from the resistance of random solute atoms, fine precipitates and lattice defects to dislocation movement (Cracknell and Petch 1955) and is about 2 tons in^{-2} in annealed mild steel. It has been suggested that $\sigma_0^\dagger$ represents an appreciable Peierls–Nabarro stress and it varies from 2 tons in^{-2} at room temperature to 24 tons in^{-2} at − 196°C when the strain rate has an ordinary value, 10^{-4} sec^{-1} (Heslop and Petch 1956). At high strain rates, $\sigma_0^\dagger$ increases considerably (Heslop and Petch 1958), so that in a notch the value of σ_0 at the lower yield point will amount to a major part of σ_0 at fracture.

The lower yield point value of σ_0 is given by

$$\sigma_{\mathrm{l.y.p.}} = \sigma_0 + kl^{-1/2}.$$

In this, the constant k is also of interest since it measures the stress required ahead of a dislocation pile-up to unlock a source, so the temperature variations of k and of γ' have a common cause. Thus, the temperature-dependence of $\sigma_{\text{l.y.p.}}$ gives information on the temperature-dependence of σ_0 and γ'. With notched specimens, it is the dependence within the range of about 0 ± 50°c that is of interest, since this covers the normal range of the observed transition temperatures.

Measurements of $\sigma_{\text{l.y.p.}}$ for a mild steel at 18, -23 and -79°c are shown in fig. 2. The composition of the steel (weight %) was 0·11 C, 0·51 Mn, 0·05 S, 0·029 P, 0·02 Si, 0·0085 N, and the strain rate was 10^{-4} per sec.

Fig. 2

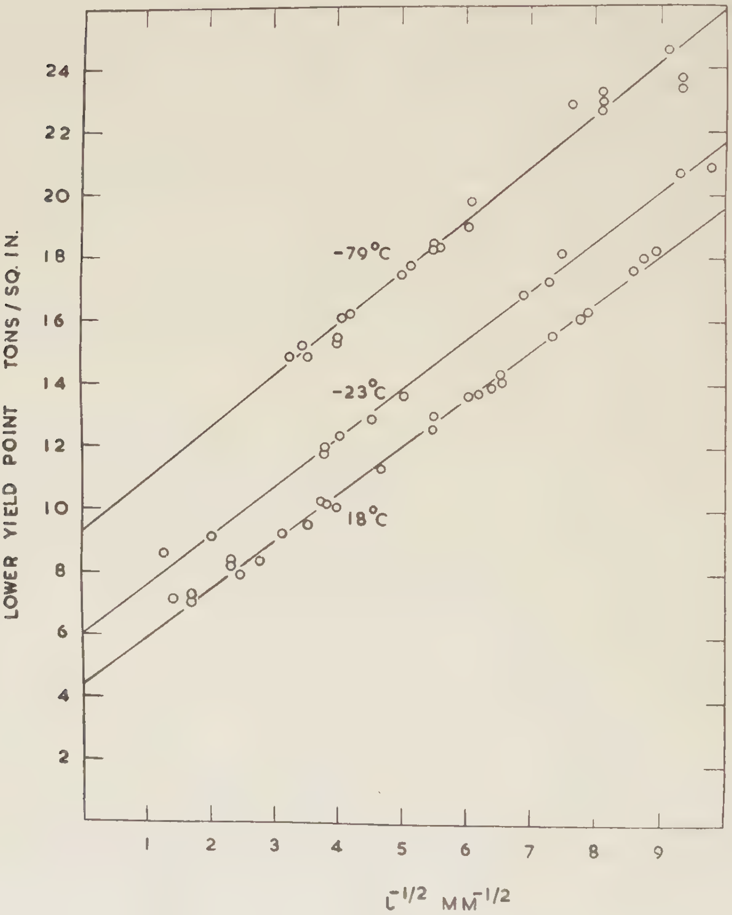

The dependence of the lower yield point on grain size.

It is clear that the temperature-dependence of $\sigma_{\text{l.y.p.}}$ in the range of interest is predominantly due to σ_0; the slope k is almost constant, showing that the dislocation locking strength is almost constant. Below about -150°c, k changes more rapidly. Baron (1956) has measured yield points at a strain rate of $10^2\,\mathrm{sec}^{-1}$, which is approaching that in a notch. These do not give the variation with grain size for one steel, instead they give single values for different steels of different grain size, but they suggest that the change in $\sigma_{\mathrm{l.y.p.}}$ in the temperature range of interest is even greater than at $10^{-4}\,\mathrm{sec}^{-1}$ and is still predominantly due to σ_0. Thus, unless there is great sensitivity to any alteration in the locking strength, the temperature-dependence of the transition criterion in notched specimens must arise mainly from σ_0 rather than from γ' and to obtain the transition temperature T_c we must examine the temperature-dependence of σ_0.

The temperature-variation of the Peierls–Nabarro stress $\sigma_0^\dagger$ arises partly from an increase in the width w of the dislocation as the temperature T rises. If the temperature range is not too wide, this increase is probably fairly linear, so giving

$$w = w_0(1+\alpha T)$$

and

$$\sigma_0^\dagger = A\exp - w_0(1+\alpha T),$$

where A and α are constants. This suggests $\sigma_0^\dagger = \mathrm{const.}\exp - \alpha T$ as a possible form for the temperature-dependence of $\sigma_0^\dagger$.

Previous measurements (Heslop and Petch 1956) agree very well with this relationship, although some divergence begins to show at −196°C. Provided σ_0^* is not too great, the whole σ_0 approximately obeys a similar relationship. Thus, with B and β as constants,

$$\ln \sigma_0 = \ln B - \beta T.$$

From (8), taking γ' as constant, it then follows that the criterion for the ductile–cleavage transition is

$$\ln B - \beta T = \ln\left(\frac{4q\mu\gamma'}{k^*} - k^*\right) l^{-1/2}.$$

Thus, the transition temperature is given by

$$\beta T_c = \ln B - \ln\left(\frac{4q\mu\gamma'}{k^*} - k^*\right) - \ln l^{-1/2}. \quad . \quad . \quad . \quad . \quad (9)$$

Less accurately, the temperature-dependence of $\sigma_0^\dagger$ may be taken as linear if the temperature range is not too wide. This gives

$$\sigma_0 = \sigma_0^* + C - \epsilon T,$$

where C and ϵ are constants, and so leads in (8) to

$$\epsilon T_c = \sigma_0^* + C - \left(\frac{4q\mu\gamma'}{k^*} - k^*\right) l^{-1/2}.$$

Summarizing the principles of this calculation of the transition temperature, it is thought that change to cleavage occurs when the tensile stress available at fracture becomes capable of Griffith propagation of a dislocation crack and that temperature affects the transition at a notch mainly through the friction stress σ_0, which is one term determining the fracture stress available for Griffith propagation. This makes the transition temperature a function of grain size, the friction on a free dislocation, the strength of the dislocation locking, the degree of triaxiality of the applied stress and the elastic constants.

The strain rate ahead of the advancing ductile fracture will have an effect on the transition temperature through its influence on the friction term and on the strength of the dislocation locking. Thus, any comparison of the transition temperatures of different steels must be made at the same ductile fracture velocity. This velocity will depend upon test conditions, such as the geometry of the specimen, and on the amount of plastic strain required prior to fracture. In a standardized notched impact test, taking the transition temperature at a constant percentage cleavage in the fracture area, the ductile fracture velocity when the change to cleavage occurs should normally be about constant. If, however, the test conditions are altered, or if the amount of plastic strain prior to ductile fracture changes drastically, then the ductile fracture velocity will alter and the transition temperatures will not be strictly comparable.

§ 4. THE GRAIN BOUNDARY OBSTACLE

From Stroh (1957), the length c of a dislocation crack when wedged open by n' dislocations on a slip plane that makes an angle θ with the crack is given by

$$c^2-\{1-2(c_1/c_2)^{1/2}\sigma_1(\sigma_1{}^2+\sigma_2{}^2)^{-1/2}\sin\theta\}c_2c+c_1c_2=0,$$

where

$$c_1=n'^2\mathbf{b}^2\mu/8\pi(1-\nu)\gamma',$$

$$c_2=8\gamma'\mu/(\sigma_1{}^2+\sigma_2{}^2)\pi(1-\nu),$$

and σ_1 and σ_2 are the components of the applied stress respectively normal and parallel to the crack.

Application of (8) to experimental measurements of the transition temperature for notched impact tests gives $\gamma'=50\,000$ ergs cm^{-2} (Heslop and Petch 1958). With an average grain size, this value of γ', $n'\sim 500$, $\sigma\sim 50$ tons in^{-2} and the orientation of fig. 1, the size of the dislocation crack that just does not spread is $\sim 10^{-4}$ cm, which is about 1/10th the grain diameter. Thus, the dislocation crack is smaller than the grain diameter until it breaks out as a cleavage crack. When this break-out does take place, there remains another barrier to passage of the crack across the specimen. This barrier is the grain boundary.

The spread of the dislocation crack as far as the first grain boundary takes place under the combined action of its own concentration of the applied stress and of the wedging by the dislocation. In the second grain, a new crack has to be nucleated and this then has to spread without help from the wedging action, if the grain boundary region connecting the cracks remains unbroken. The tensile stress σ_b required will be close to the Griffith stress for propagation of a crack of width about $\frac{1}{2}l$. This gives

$$\sigma_b=\{16\mu\gamma'/\pi(1-\nu)l\}^{1/2}.$$

Thus, from (7), the fracture stress that just permits spreading of the dislocation crack can ensure propagation across the second grain if

$$\frac{16\mu\gamma'}{\pi(1-\nu)(1+1/\sqrt{2})k^{*}l^{1/2}}=\left(\frac{16\mu\gamma'}{\pi(1-\nu)l}\right)^{1/2},$$

or

$$\gamma'=\pi(1-\nu)(1+1/\sqrt{2})^{2}k^{*2}/16\mu. \quad . \quad . \quad . \quad . \quad (10)$$

Experimentally, $k^{*}=2\times10^{8}$ c.g.s. units (Petch 1956 a), so $\gamma'=21\,000$ ergs cm^{-2} in (10). With lower values of γ', the cleavage crack may be held up at the grain boundary.

Thus, in notched impact tests, with $\gamma'=50\,000$ ergs cm^{-2}, it appears probable that once a dislocation crack breaks out across one grain, it will normally be able to induce cleavage across the second grain. The two cleavage cracks will of course be inclined to one another and the grain boundary region between them will remain to be broken.

If the length of crack that is able to form in the first grain before the boundary is reached is only a small part of the grain diameter, or if the second grain is particularly unfavourably oriented, the crack may be halted by the boundary.

In the fracture of un-notched specimens, γ' may possibly be less than 21 000 ergs cm^{-2} at the low temperature of the fracture transition (about −200°c) and the first cleavage crack may then be arrested at the grain boundary. Thus, below the fracture mode transition temperature for un-notched specimens, there is possibly another transition associated with whether or not the fracture stress is greater or less than σ_b.

ACKNOWLEDGMENT

During the preparation of the present paper it has been a pleasure to discuss the problem of brittle fracture with Dr. A. H. Cottrell, F.R.S., who has developed ideas that are in some respects similar to those discussed here.

REFERENCES

BARON, H. G., 1956, *J. Iron St. Inst.*, **182**, 45.

CRACKNELL, A., and PETCH, N. J., 1955, *Acta Met.*, **3**, 186.

DORN, J. E., 1948, *Fracturing of Metals* (Amer. Soc. Metals), p. 32.

ESHELBY, J. D., FRANK, F. C., and NABARRO, F. R. N., 1951, *Phil. Mag.*, **42**, 351.

HESLOP, J., and PETCH, N. J., 1956, *Phil. Mag.*, **1**, 866; 1958, *Ibid.*, **3**, 1128.

MOTT, N. F., 1953, *Proc. roy. Soc.* A, **220**, 1; 1956 a, IUTAM Madrid Colloquium, *Deformation and Flow of Solids* (Berlin: Springer-Verlag), p. 53; 1956 b, *J. Iron St. Inst.*, **183**, 233.

PARKER, E. R., 1957, *Brittle Behaviour of Engineering Structures* (New York: John Wiley), p. 11.

PETCH, N. J., 1953, *J. Iron St. Inst.*, **174**, 25; 1954, *Progress in Metal Physics, V* (London: Pergamon Press), p. 1; 1956, *Phil. Mag.*, **1**, 186.

ROBERTSON, T. S., 1953, *J. Iron St. Inst.*, **175**, 361.

STROH, A. N., 1954, *Proc. roy. Soc.* A, **223**, 404; 1955 a, *Ibid.*, **232**, 548; 1955 b, *Phil. Mag.*, **46**, 968; 1957, *Advanc. Phys.*, **6**, 418.

ZENER, C., 1948, *Fracturing of Metals* (Amer. Soc. Metals), p. 3.

The Orientation Dependence of Cyclic Work-Hardening in Aluminium Crystals[†]

By P. CHARSLEY and N. THOMPSON
H. H. Wills Physics Laboratory, University of Bristol

[Received June 20, 1958]

ABSTRACT

Crystals of aluminium have been subjected to several hundred slow cycles of stress: the rate of decrease of the width of the hysteresis loop is taken as a measure of cyclic work hardening. The manner of hardening depends on the orientation of the crystal and is qualitatively similar to the hardening observed in uni-directional straining.

§ 1. INTRODUCTION

OBSERVATIONS of the deformation under repeated reversed stresses of face-centred cubic metals have been reported by Thompson *et al.* (1956), Paterson (1955) and Scholl (1957). Paterson subjected copper crystals to alternate tensile and compressive stresses so that the shear strain amplitude was constant at $8{\cdot}3\times10^{-3}$; each crystal was observed for between 20 and 40 such cycles. From measurements of the stress amplitude, shear stress–shear strain curves were plotted; they exhibited a marked orientation dependence which was similar to that found in tensile tests.

In the experiments of Thompson *et al.* (hereinafter referred to as I) on crystals of aluminium the conditions were more closely related to those of a fatigue test than in Paterson's experiments. Reversed stressing experiments were carried out at a constant stress amplitude for several hundred cycles; the strains were kept small so that the width of the hysteresis loop was of the order 1×10^{-4}. It was found that after the initial few cycles at a new stress amplitude, the loop width steadily decreased with further cycling. For a number of cycles ranging about 10 to 1000 an empirical relation was found between the loop width W and the number of cycles n of the form

$$W = An^{-q} \quad . \quad . \quad . \quad . \quad . \quad . \quad . \quad . \quad . \quad . \quad (1)$$

where q is a constant.

The experiments described in this paper are a continuation of those described in I: it is shown that the value of q in eqn. (1) is appreciably dependent on the specimen orientation and that, for certain orientations, its magnitude is strongly dependent upon the stress amplitude.

§ 2. SPECIMEN PREPARATION AND EXPERIMENTAL PROCEDURE

Single crystals of aluminium (99·995% purity) about 8 cm long and 9 mm in diameter were grown by two methods. Specimens A to E were grown from the melt, and I, M and N by the strain-anneal method. The crystal orientations were determined by back-reflection Laue photographs and are shown in fig. 1. The crystals were lightly machined to make them accurately straight and cylindrical; heavily electropolished in a 2 : 1 mixture of methanol and nitric acid and then annealed *in vacuo* for approximately 10 hours at 600°c.

[†] Communicated by the Authors.

The specimens, fitted with duralumin knobs, were tested in the apparatus described in I, except in the case of specimens I, M and N which were tested in a modified form of the apparatus suitable for low temperautre work.

The basic procedure was the same in all experiments described here. For each new specimen a few complete hysteresis loops were plotted at small stresses, such that the loop widths were of the order 1×10^{-5}. The initial direction of stressing was sometimes in tension and sometimes compression; the initial direction sometimes affected the early stress–strain behaviour but appeared not to affect subsequent behaviour. After these preliminary cycles, the stress amplitude (which was always equal in tension and compression to within about 0·2%) was increased step-wise by the addition of small load increments, until a loop width of about 1×10^{-4} was obtained. Observations after this were almost always confined to the width of the hysteresis loop and its variation with the number of cycles. All observations were at room temperature.

Fig. 1

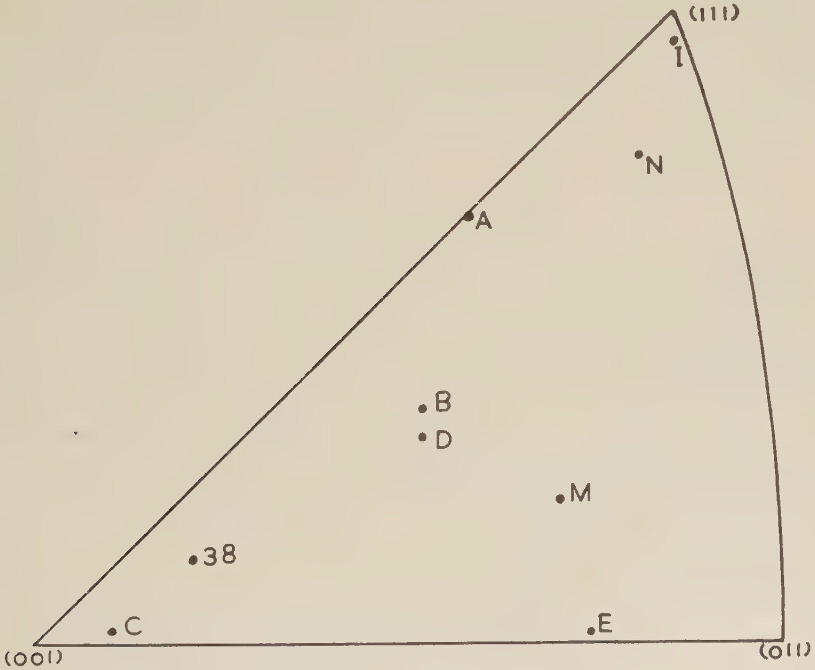

The orientations of the specimens.

When the loop width at a given stress amplitude had decreased to a small value a stress increment was added and a new series of observations begun. The stress increment was added during an odd half-cycle, i.e. when the loading was in the direction in which the tests had begun on that particular specimen.

§ 3. EXPERIMENTAL RESULTS

The general behaviour of the loop width after the addition of a stress increment has been outlined in I. In this paper we are only concerned with the behaviour after the first few cycles at a new stress amplitude and in this case the loop width steadily decreased for some thousands of cycles.

It was not always found that eqn. (1) above was completely satisfactory over many hundreds of stress cycles though it often was. For the purposes of comparing the cyclic hardening behaviour of different crystals, however, a value of the exponent q was calculated on the assumption that the equation had been obeyed between 10 and 400 cycles (a convenient but arbitrary range). Thus the value of q is a measure of the rate of cyclic work hardening; a large positive value of q indicates a rapid decrease in the loop width with number of cycles of stress.

§ 4. ORIENTATION DEPENDENCE OF q

In the table are shown the values of q obtained at various stress levels for the different specimens examined. In the first group are specimens oriented in such a way that slip on more than one system would be expected, at small strains, in a tensile test. These specimens are N, I and C together with some results on specimen 38 from I. The values of q are large and show very little variation with stress amplitude. Specimen N shows a remarkably constant value of q and the curves of loop width versus number of cycles for this specimen are shown in fig. 2. These curves illustrate the way in which results on specimens in this group were a good fit to eqn. (1).

Specimens B, D and M are all oriented near the centre of the stereographic triangle; slip on a single system only would be expected up to quite high strains in a tensile test. In contrast to specimens in the last group, the value of q is seen to be strongly stress dependent. At the lowest stress amplitude on specimens M and D the loop width was constant, within the experimental error of $\pm 1 \times 10^{-6}$, between about 5 and 200 cycles, after which observations were stopped. This behaviour is shown for the case of specimen M in fig. 3.

As the stress amplitude is raised, the value of q increases to a maximum and then decreases again. There is some diversity among the results about the detail of this behaviour and this possibly reflects differences in orientation. Specimen M, which was investigated for a greater range of stresses than the other specimens shows clearly the decrease in q as the

Resolved shear stress (g/mm²)	N	I	C	38	B	D	M	E	A_1	A_2
100–120	0·48	—	—	—	—	0	0		—	—
120–140	0·46	—	—	—	0·20	—	0·06	—	—	0·20
140–160	0·46	—	0·24	—	0·30	—	0·17	0·31	0·13	—
160–180	—	—	—	—	0·24	0·09	0·16	0·23	—	0·16
180–200	0·48	—	—	—	0·17	0·12	0·11	—	0·17	0·17
200–220	—	0·53	0·31	—	—	0·13	—	0·11	0·17	—
220–240	0·43	—	—	—	0·14	0·11	0·08	0·12	0·16	—
240–260	—	0·53	0·29	0·3	—	—	0	0·11	0·18	—
260–280	—	—	—	—	—	—	—	—	—	—
280–350	—	—	0·34	0·34 0·40	—	—	Small negative value	—	—	—

Fig. 2

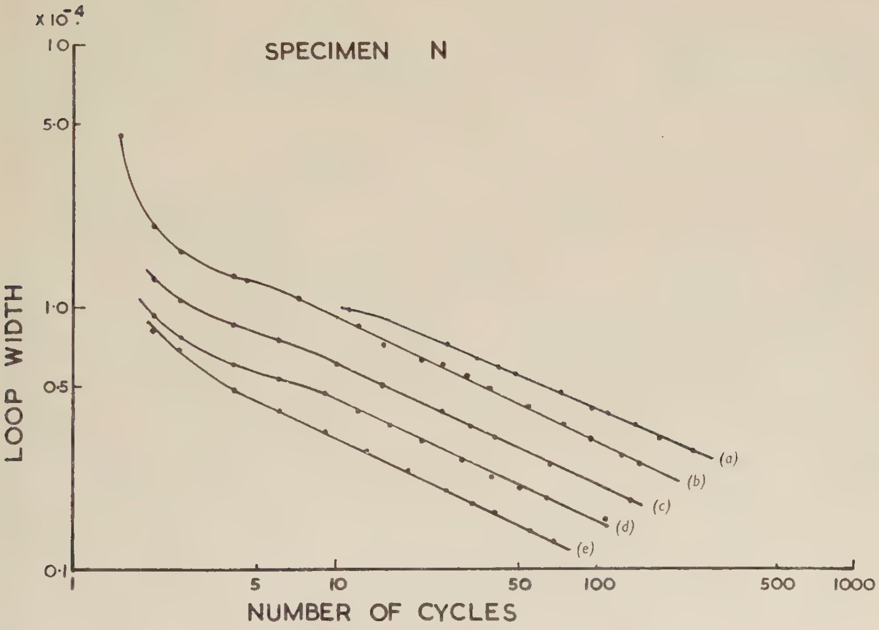

Cyclic work-hardening curves for specimen N. Maximum cyclic resolved shear stresses, in g/mm² : (*a*) 230 ; (*b*) 190 ; (*c*) 145 ; (*d*) 120 ; (*e*) 95.

stress amplitude is raised. At the two highest stress amplitudes investigated the loop width began to increase with cycling after about 100 cycles. Except at the highest stresses the results on specimens on this group fitted eqn. (1) very well.

Specimen E, oriented nearly on the [100]-[110] boundary, behaved similarly to specimens in the previous group but no early stage of low hardening was observed. Only at the highest stresses did the results fit eqn. (1) at all well.

Fig. 3

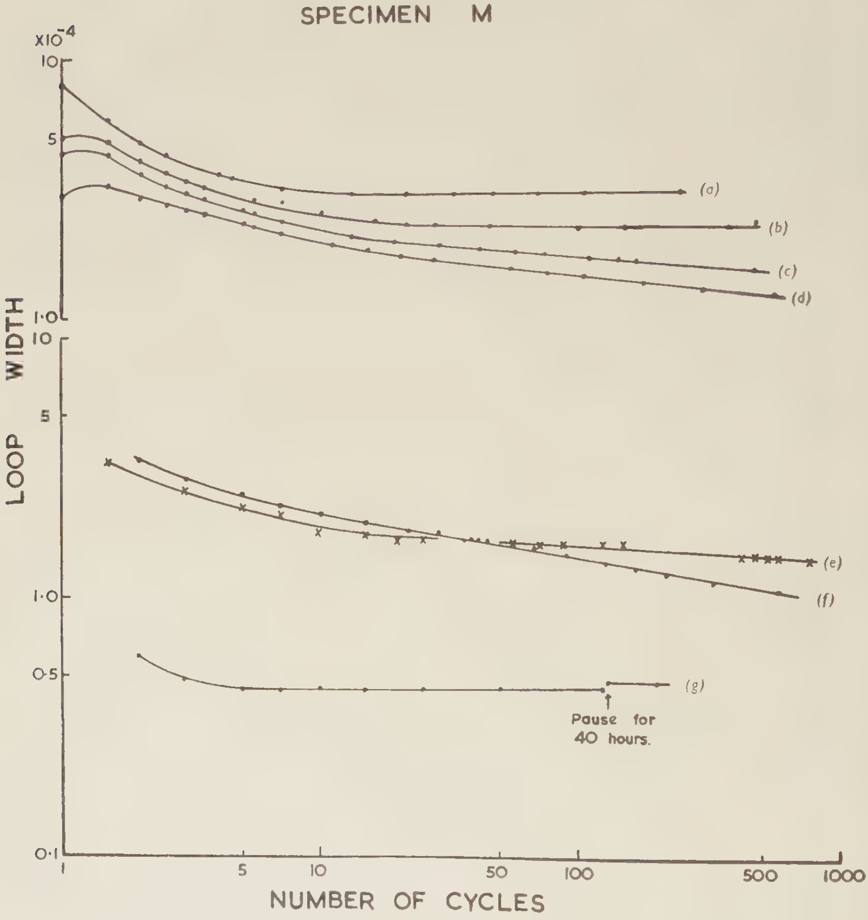

Cyclic work-hardening curves for specimen M. Maximum cyclic resolved shear stresses, in g/mm^2 : (*a*) 285 ; (*b*) 255 ; (*c*) 225 ; (*d*) 195 ; (*e*) 135 ; (*f*) 150 ; (*g*) 115. (The origin of the top curves has been displaced relative to the lower curves for clarity.)

Specimens A_1 and A_2 cut from the same crystal were oriented on the [100]-[111] boundary. In spite of the fact that these two specimens had appreciably different mechanical histories, the values of q obtained at similar stress amplitudes are in good agreement on the two specimens. Thus it would appear that the value of q is not strongly dependent upon previous history. The actual values of q were intermediate between those of the first and second groups of specimens and the results fitted eqn. (1) well.

§ 5. Observations of Slip Markings

When mechanical observations were finished on each specimen the surfaces were examined microscopically. Marked differences in the patterns of slip markings were found between specimens of different orientations. Specimens of the first group showed slip markings on more than one system; the slip markings on the primary system often occurred in groups separated by relatively slip-free regions in which slip on another system could sometimes be seen. The slip markings on specimen 1 occurred on three systems almost equally. Specimens on the second group showed slip markings uniformly spaced along the specimen with no apparent slip on other systems. Since these results are very similar to those obtained by Honeycombe (1951/2) in unidirectional stressing, and Paterson (1955), no more will be said about this point.

Specimen M showed slip bands in certain regions quite different in detail from those seen on other specimens. In fig. 4 (*a*), Pl. 79 is shown the type of marking which was seen on all the other specimens and on some regions of M; fig. 4 (*b*), Pl. 79 shows the quite different markings also seen on M. The surface is rumpled and they closely resemble typical fatigue slip bands.

§ 6. Discussion

In so far as the different experimental conditions permit a comparison, the above results on aluminium are in qualitative agreement with Paterson's results on copper. Although the total number of cycles and the strain amplitudes were very different the cumulative (absolute) strains were similar in the two sets of experiments. In both investigations the general pattern of surface slip markings runs parallel to that found in unidirectional stressing, as regards its orientation dependence. In both, orientations in which multiple slip is favoured show a high rate of cyclic hardening (a high, stress-independent q in our case) while in a tensile test the stress–strain curve rises steeply, almost linearly, with stress. Orientations near the centre of the stereographic triangle give a rate of hardening which is very dependent on stress; in our case the value of q was very small, or zero, at low stresses and increased, and the decreased again, as the stress amplitude was raised. In Paterson's experiments and in unidirectional tensile experiments this behaviour of q was closely paralleled by the variation of the rate of hardening with increased stress.

These considerations lead us to explain the orientation dependence of the rate of decrease in loop width with the number of stress cycles in terms of slip occurring on secondary systems. We suppose that the loop width at a given stress amplitude results from the movement to-and-fro of a given set of dislocations and that cyclic work-hardening is a result of the formation of sessile Lomer–Cottrell dislocations by the reaction of some of these dislocations with dislocations on secondary slip planes in the manner proposed by Mott (1952). The sessile dislocations reduce the loop width in two ways; they decrease the number of dislocations able to move to-and-fro under the alternating stress and reduce the slip distance of those still free to move. The rapid hardening which occurs at all stresses when the orientation approaches [100], [111] or the [100]–[111] boundary arises from the relatively high shear stresses on secondary slip planes. Thus sessile dislocations are produced frequently even at low stresses. For crystals of a central orientation, at low stresses the hardening is very small because there are very few dislocations free to move on the secondary slip systems. As the stress increases more dislocations move on secondary slip systems and the value of q increases; this corresponds to the short stage of linear hardening in the tensile stress–strain curve.

The results on specimens D and M indicate that as the stress is further increased the value of q decreases until eventually the loop width increases with further cycling. This can perhaps be explained by the breaking down of Lomer–Cottrell barriers in the manner suggested by Friedel (1955) or Seeger *et al.* (1957) to explain the parabolic hardening stage in the tensile stress–strain curve. The change in appearance of the slip markings on specimen M further suggests that the breakdown is a result of cross-slip as proposed by Seeger *et al.* The observations on this specimen suggest that the change in appearance of the slip bands and the widening of the hysteresis loop are closely correlated.

REFERENCES

Friedel, J., 1955, *Phil. Mag.*, **46,** 1169.
Honeycombe, R. W. K., 1951/2, *J. Inst. Met.*, **80,** 49.
Mott, N. F., 1952, *Phil. Mag.*, **43,** 1151.
Paterson, M. S., 1955, *Acta Met.*, **3,** 491.
Scholl, H., 1957, *Z. Metallk.*, **48,** 258.
Seeger, A., Diehl, J., Mader, S., and Rebstock, H., 1957, *Phil. Mag.*, **2,** 323.
Thompson, N., Coogan, C. K., and Rider, J. G., 1956, *J. Inst. Met.*, **84,** 73.

The Climb of a Dislocation in a Twisted Whisker†

By F. R. N. Nabarro and P. J. Jackson
Department of Physics, University of the Witwatersrand, Johannesburg

[Received June 16, 1958]

SUMMARY

Gomer's observation that twisted mercury whiskers have periodic imperfections separated by distances closely related to the pitch of the twist is explained by considering a dislocation which is approximately parallel to, but displaced from, the axis of the whisker. This dislocation is straight in cartesian coordinates, but helical in the coordinates provided by the crystal lattice.

§ 1. INTRODUCTION

GOMER (1958) has shown, by a series of elegant experiments in a field emission electron microscope, that mercury whiskers grow as single crystals with axis [110] in the pseudo-cubic face-centred system, and attain lengths l of order 0·01 cm and radii r of order 70 Å. The presence of an axial screw dislocation of strength $b = 3 \times 10^{-8}$ cm is revealed in the following manner. According to Eshelby (1953) such a dislocation will cause the top and bottom of the whisker to be rotated with respect to one another through an angle $bl/\pi r^2$, about 15 complete turns. When the electric field in the microscope is increased, l increases and r decreases, and the angle of twist should increase by an observable amount, of order 0·15 radians. Twists of just this order are observed experimentally.

When the field is further increased, the whisker breaks, often at some point along its length. Field emission can be observed from the end of the stump, and, unexpectedly, the orientation of the pattern is unchanged. Gomer remarks that "the lack of pattern rotation observed after partial pull-off is probably due to insufficient statistics or preferential breakage points". The aim of the present paper is to explain the occurrence of imperfections which are spaced regularly along the whisker with a separation equal to one half of the pitch of the Eshelby twist.

§ 2. CLIMB OF A DISLOCATION IN A TWISTED WHISKER

The explanation is based on the idea that a whisker grown by sublimation will contain a concentration of vacant lattice sites in excess of the equilibrium value. The screw dislocation along its axis therefore tends to adopt a helical form and absorb vacancies by climb (Seitz 1950, Weertman 1957). The novel feature is that a geometrically straight, but eccentric, dislocation parallel to the axis of a twisted whisker is in fact a helical dislocation in lattice coordinates. As it moves out from the centre, still remaining straight, it absorbs vacancies. Initially the straight form of the dislocation is stable, because it is the form having the smallest line energy. However, the lattice, which has two-fold symmetry round the axis, is twisted, and the actual direction of motion of the dislocation coincides with an easy direction of motion at a series of points separated by half the pitch of the twist. Figure 1 shows $1\frac{1}{4}$ turns of the twisted whisker, and five positions of the dislocation. As the

---

† Communicated by the Authors.

Fig. 1

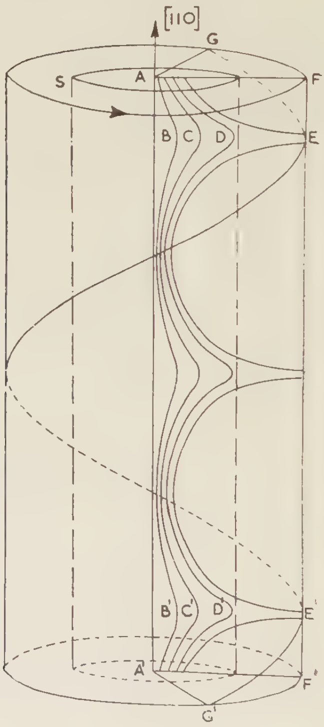

Motion of a dislocation in a twisted whisker. The five positions of the dislocation (AA′, BB′, CC′, DD′ and EE′) are all taken to lie in the plane of the figure, although the outer portions of EE′ probably deviate from this plane. It is assumed for illustration that the easy motion of the dislocation is in the $(1\bar{1}0)$ plane. GG′ is the trace of the twisted $(1\bar{1}0)$ plane. The cylinder S represents the limit of stability of a screw dislocation.

straight dislocation moves outwards, its inclination to the [110] lattice direction increases, and its character develops an edge component. The edge components are always attracted towards the free surface, and the screw components are attracted when they are close enough. The outward bulges in position BB′ are thus unstable. They move towards the surface, attracting vacancies from neighbouring portions of the whisker, and may reach the surface while the rest of the dislocation is still close to the axis. The edge-like portions of the dislocation where it comes closest to the surface produce longitudinal compression between the dislocation and the surface. On the opposite side of the whisker is a region of dilatation where fracture is initiated when the whisker is pulled. The possible points of fracture are thus separated by one half of the pitch of the Eshelby twist. Since the Eshelby twist is reduced by the migration of the dislocation towards the surface, it must be assumed that the instability of this motion leads to a configuration in which bulges reaching to the surface are joined by long portions of dislocation which are displaced only negligibly from the axis. The dislocation itself may act as a diffusion short circuit (Turnbull 1955).

It is still necessary to explain why the growth of the whisker stops at one of the possible fracture points. During the phase of rapid growth, the rate of deposition of atoms on the tip of the whisker first increases exponentially with time, and then reaches a limiting maximum value. It is almost certain that the excess of vacant lattice sites will be greatest at the highest rate of deposition, so that the rate of motion of the dislocation away from the axis will be greatest near the tip. When the end of the dislocation ceases to lie on the growing surface, and reaches the cylindrical surface, growth stops. This will generally happen when the remainder of the dislocation is still embedded in the crystal, so that the Eshelby twist will still be present.

§ 3. EDGE COMPONENT OF AN ECCENTRIC DISLOCATION

Eshelby has shown that if a screw dislocation of strength b lies a distance ξ from the axis of a circular cylinder of radius r, the cylinder suffers a uniform twist of $(1-\xi^2/r^2)b/\pi r^2$ per unit length. Consider a row of atoms in the lattice which originally lay a distance b apart on a line parallel to the axis and distant ξ from it. This line is now inclined at an angle $(1-\xi^2/r^2)b\xi/\pi r^2)$ to the axis, and the Burgers vector of the dislocation has magnitude b in the direction of this line. The dislocation thus has an edge-like component of its Burgers vector in a direction tangential to the dislocation of $(1-\xi^2/r^2)b^2\xi/\pi r^2$. When the whisker moves a distance $d\xi$, it absorbs a volume of vacancies $(1-\xi^2/r^2)b^2\xi d\xi/\pi r^2$ per unit length. The volume change when unit length of the dislocation moves from the axis to the surface is $b^2/4\pi$. This represents an absorption of one vacancy per 4π planes, independent of the diameter of the whisker. The proportionality to b^2 shows that this is a non-linear elastic effect.

The sign of the effect may be seen by considering the process by which the screw dislocation might be inserted into a perfect whisker. Let a cut AA′G′G be made in the whisker as in fig. 2. Let the material on the near side of this cut be displaced with respect to the material on the far side by a distance b in the direction AA′. The Burgers vector for the circuit indicated by the arrow in fig. 2 is then b in the direction A′A. The traction exerted on the lower face of the cut is in this direction, and, from the symmetry of the stress tensor, the traction on the upper surface of the whisker in the state of anti-plane strain must have the direction opposite to the arrow. If the traction on this end is released, the whisker twists in the direction of the arrow, as indicated in fig. 1. Thus the introduction of a left-handed screw dislocation into a cylinder causes the lattice to develop a right-handed twist. The Burgers vector is now tilted so that in addition to the axial component in the direction A′A there is a tangential component in the direction of that arrow. This represents the insertion of additional matter in the cut AA′F′F, which is annihilated by vacancies as the dislocation moves from AA′ towards the surface.

Fig. 2

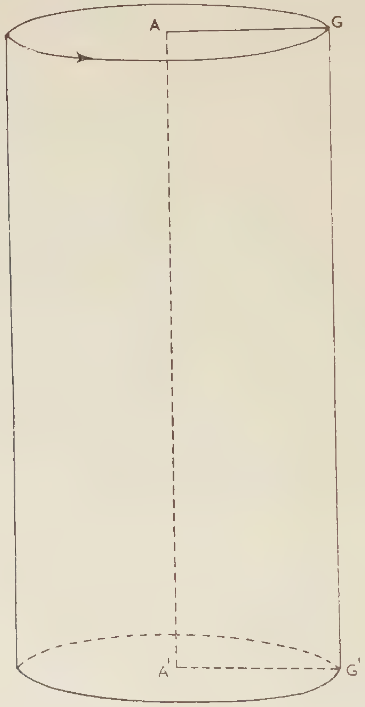

Insertion of a screw dislocation into a perfect whisker.

ACKNOWLEDGMENT

We are indebted to Dr. Gomer and the Institute for the Study of Metals for allowing us to see the manuscript of his paper before publication.

REFERENCES

ESHELBY, J. D., 1953, *J. appl. Phys.*, **24**, 176.
GOMER, R., 1958, *J. chem. Phys.*, **28**, 457.
SEITZ, F., 1950, *Phys. Rev.*, **79**, 1003.
TURNBULL, D., 1955, *Defects in Crystalline Solids* (London), p. 203.
WEERTMAN, J., 1957, *Phys. Rev.*, **107**, 1259.

On the Stability of Dislocations in Metal Whiskers†

By J. P. Hirth and F. C. Frank
H. H. Wills Physics Laboratory, University of Bristol

[Received June 25, 1958]

Abstract

The possibility of thermally activated slip of dislocations out of metal whiskers is considered. Such an event provides a mechanism for the cessation of whisker growth. It is found that a single axial dislocation will be in unstable elastic equilibrium if it has an edge component with respect to the whisker axis greater than a critical amount. Metastable dislocations with edge components less than this critical amount have an expectation time for slip out of the whisker which is dependent on whisker radius, temperature, and the elastic properties of the whisker material. The effects on whisker morphology predicted by this mechanism are discussed.

The occurrence of metal whiskers is now a well chronicled phenomenon, such filamentary forms having been observed for example in growth from a supersaturated vapour phase (Sears 1953) in spontaneous growth from the bulk phase (Compton *et al.* 1951), in growth due to the reduction of metal salts (Brenner 1956), and in growth from the vapour phase in the presence of an inert gas (Sears and Coleman 1957). Results of orientation determinations of whiskers spontaneously grown from the bulk phase (Treuting and Arnold 1957) are consistent with theories such as those of Eshelby (1953 a) and Frank (1953) which show that spontaneously grown whiskers do not require the presence of a dislocation with screw orientation with respect to the whisker axis to account for growth. However, the mechanisms advanced to explain whisker growth from the vapour or liquid phases (Sears 1955, Brenner and Sears 1956, Newkirk and Sears 1955) all postulate that an axial screw dislocation is present in the whiskers. The demonstration by Eshelby (1953 b) that such an axial screw dislocation would be in metastable elastic equilibrium in the whisker enhances the feasibility of these mechanisms. In the following discussion consideration will be given to the possibility that a metastable dislocation may slip out of a whisker under thermal activation. Although the removal of a single axial dislocation from a whisker may not directly affect the strength of the whisker, the removal is effective as a mechanism for the cessation of whisker growth.

Screw dislocations owe their stability on the axis to the torsion of the cylinder which they cause. Edge dislocations cause no analogous secondary effect, and are in unstable equilibrium on the axis.

---

† Communicated by the Authors.

Consider a dislocation in a right circular cylinder whisker of an idealized isotropic material as depicted in fig. 1 where the dislocation at a point is displaced an amount $\xi(z)$ from the axis of the whisker in the slip plane xz. If the Burgers vector $\mathbf{b}$ of the dislocation is directed at an angle ϕ to the whisker axis, there will be an angle ϕ' which will be the limiting angle for which the dislocation will be in metastable elastic equilibrium when lying on the whisker axis. Letting the dislocation be displaced a uniform distance ξ along the whisker length L, the energy per unit length of the dislocation is given by

$$W(\xi)=\frac{\mu b^2}{4\pi}\left\{\cos^2\phi\left[\ln\frac{(R^2-\xi^2)}{r_0R}-\frac{(R^2-\xi^2)^2}{R^4}\right]+\frac{\sin^2\phi}{(1-\nu)}\left[\ln\frac{(R^2-\xi^2)}{r_0R}-\frac{1}{2}\right]\right\}, \quad . \quad . \quad . \quad (1)$$

where ν is Poisson's ratio, μ is the shear modulus, and b is the magnitude of the Burgers vector, neglecting terms in r_0, the radius of the core of the dislocation. The term containing $\cos^2\phi$ is the expression due to Eshelby (1953 a) for the elastic energy of a screw dislocation displaced an amount ξ from the axis of a cylindrical rod of finite length, and the term containing $\sin^2\phi$ is Koehler's (1941) solution of the analogous problem for an edge dislocation in a cylindrical rod of infinite length. In the latter case there is no additional energy term due to the restriction to finite length because there is no net moment developed at the ends when this restriction is invoked, so that the end effects are confined to a length $\sim 2R$ at the ends following St. Venant's principle. ϕ' is the value of ϕ for which $(\partial W/\partial\xi)_{\xi=0}=0$, i.e. that given by $\tan^2\phi=1-\nu$. For metals ϕ' thus lies in the range 35°–45°, a typical value being $\phi'=39{\cdot}2°$ for copper. Thus a $\frac{1}{2}[110]$ dislocation on the axis of copper whiskers of [110] or [111] orientation would be in metastable equilibrium, but it would be in unstable equilibrium if the axis were [100].

Fig. 1

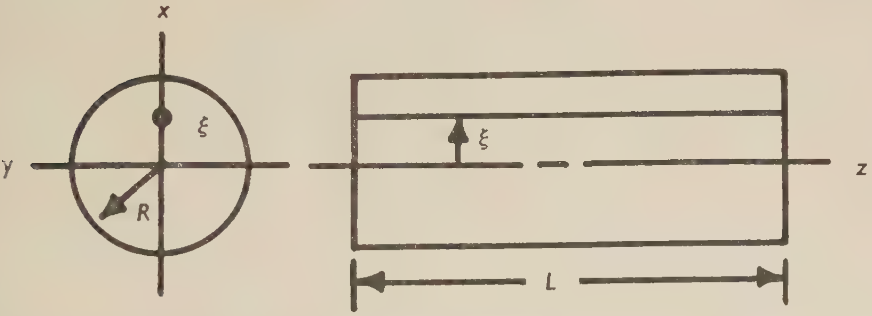

Dislocation displaced an amount ξ from the axis of a whisker of radius R and length L.

Considering now the metastable cases $\phi<\phi'$, we remove the restriction that the dislocation line displaces parallel to itself. We shall assume that the energy is now given to a sufficient approximation by the sum of two terms, one being a line tension for the dislocation multiplied by its increase in length, the other the work done against Eshelby's radial restoring force, represented by $W(\xi)\,dz$ for axial element of length dz. This implies that the torsion in the whisker, which is the source of Eshelby's restoring force, varies along the whisker in accordance with the variation of ξ. An extreme case indicates the degree of justification of this assumption. Suppose the dislocation line runs along the axis to a certain point, where it runs out of the whisker on a radial line. This may be made, imaginarily, by welding together the ends of a dislocated and an undislocated whisker.

Fig. 2

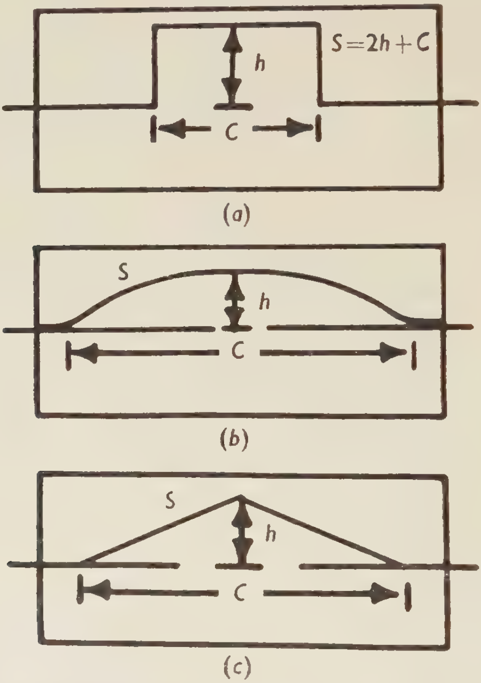

Configurations of dislocation loops of arc length s in a section of length c of a whisker.

Evidently there will be a transition from the condition of uniform torsion to zero torsion occurring essentially within a diameter or two of the exit point. Our approximation is considered to be justified whenever the length of the displaced loop is more than a few diameters of the whisker. Hence we estimate the increase of energy in the formation of a displaced loop as in figs. 2 (a, b, c) as

$$\Delta W = \int_{-c/2}^{c/2} W(\xi)\,dz + (s-c)\frac{\mu b^2}{4\pi}\ln\frac{R}{r_0}. \quad . \quad . \quad . \quad . \quad (2)$$

We wish to examine whether the dislocation can escape from the whisker by thermal agitation.

In general, ΔW will have a maximum with respect to the amplitude of displacement. This is large for a long loop, by reason of the first term, and for a short loop, by reason of the second. It will be least for a loop of intermediate length, and of a particular optimum shape. This least value of the maximum energy will be the activation energy for escape. For simplicity, we assume a simple arbitrary displacement function

$$\xi = h(1-2|z|/c),\ |z| < \tfrac{1}{2}c;$$

$$\xi = 0,\ |z| > \tfrac{1}{2}c,$$

for which

$$\Delta W = \frac{\mu b^2 c}{4\pi}\left\{\left[\cos^2\phi + \frac{\sin^2\phi}{(1-\nu)}\right]\left[\ln\left(1-\frac{h^2}{R^2}\right) + \frac{R}{h}\ln\frac{(1+h/R)}{(1-h/R)} - 2\right]\right.$$
$$\left. + \cos^2\phi\left[\frac{2}{3}\left(\frac{h}{R}\right)^2 - \frac{1}{5}\left(\frac{h}{R}\right)^4\right] + \left[\left(1+\frac{h^2}{c^2}\right)^{1/2} - 1\right]\ln\frac{R}{r_0}\right\}, \quad . \quad . \quad (3)$$

and find the value of h and c for which ΔW is simultaneously a maximum with respect to the first and a minimum with respect to the second: the corresponding values are denoted by ΔW^*, h^*, c^*. Other trial displacement functions $\xi = h\cos\pi z/c$, and $\xi = h(1-2|z|/c)^{1/2}$, gave very similar results. All such functions must over-estimate the activation energy. The similarity of results indicates that the over-estimate is not large.

The rate of escape from a length L (the reciprocal of the expectation time for escape, τ) is taken to be

$$\tau^{-1} = \omega\left(\frac{L}{c}\right)\exp\left(-\Delta W^*/kT\right), \quad . \quad . \quad . \quad . \quad . \quad . \quad . \quad (4)$$

where ω is the vibration frequency for the dislocation loop, and (L/c) is an estimate of the effective number of portions of the dislocation line which can independently reach the activation position. It is sufficient for our purposes that the factors multiplying the exponential be estimated in order of magnitude. The dislocation is assumed to be pinned on the axis at the ends of the whisker. Were it not so, it is doubtful whether it could be stable at a free end at all.

For illustration the particular case of copper whiskers grown from the vapour will now be treated. $\nu = 0{\cdot}34$, $\mu = 4\times10^{11}$ dyne cm^{-2}, $b = 2{\cdot}5\times10^{-8}$ cm, and $L = 10^{-1}$ cm are taken as typical values and ω is approximated by

$$\omega \cong \frac{1}{2\pi}\left(\frac{1}{m}\frac{\partial^2\Delta W}{\partial h^2}\right)^{1/2}, \quad . \quad . \quad . \quad . \quad . \quad . \quad . \quad . \quad (5)$$

where m is the effective mass of the dislocation $\simeq \rho b^2 c$, and ρ is the density. The solutions to eqns. (4) and (5) are presented in table 1 for a $\frac{1}{2}$ [110] dislocation in a [110] axis whisker, $\phi = 0°$, and in a [111] axis whisker, $\phi = 35{\cdot}25°$. For $\phi = 0°$, $\omega = 10^7$ sec^{-1}, and $h^* = 0{\cdot}75R$; for $\phi = 35{\cdot}25°$, $\omega = 10^6$ sec^{-1}, and $h^* = 0{\cdot}32R$. It can be seen from table 1 that the probability of a dislocation slipping out of a whisker is negligible for values of R greater than an essentially critical value.

The whisker axes [110] and [111] in the above illustration are those observed in experiment (Brenner 1956). In general, whisker axes observed in experiment are confined to those directions which are zone axes of low indices, doubtless indicating that surface energy is one of the important factors governing whisker morphology.

Table 1. Time Required for a Loop of a $\frac{1}{2}$ [110] Dislocation to Slip out of a Copper Whisker at 700°c

Whisker axis	[111]			[110]		
R (cm)	10^{-6}	$5{\cdot}8\times10^{-6}$	10^{-5}	10^{-7}	$3{\cdot}1\times10^{-7}$	10^{-6}
τ (sec)	$2{\cdot}4\times10^{-7}$	$3{\cdot}6\times10^{3}$	$1{\cdot}6\times10^{15}$	$2{\cdot}7\times10^{-8}$	$3{\cdot}6\times10^{3}$	10^{43}
c^* (cm)	$7{\cdot}3\times10^{-5}$	$4{\cdot}9\times10^{-4}$	$9{\cdot}6\times10^{-4}$	$5{\cdot}0\times10^{-7}$	$1{\cdot}5\times10^{-6}$	$6{\cdot}5\times10^{-}$

Once the dislocation has intersected the whisker surface it will be acted on by an effective stress tending to drive the dislocation along the whisker axis and out of the whisker. This stress can be computed by equating the work done by the stress in moving the dislocation a fixed distance along the axis to the energy change accompanying such an operation. In the case $\phi=0$ the dislocation has no screw component with respect to the cylindrical surface and the effective stress is given by

$$\sigma_e=\frac{\mu b}{4\pi R(1-\nu)}\left(\ln\frac{R}{r_0}-1\right). \quad . \quad . \quad . \quad . \quad . \quad . \quad . \quad (6)$$

In the case $\phi=90°$, the dislocation is pure screw with respect to the cylindrical surface so that energy will be required for the formation of a step in the surface of height equal to the Burgers vector of the dislocation. The stress is now given by

$$\sigma_s=\frac{\mu b}{4\pi R}\left(\ln\frac{R}{r_0}-1\right)-\frac{\gamma}{R}, \quad . \quad . \quad . \quad . \quad . \quad . \quad . \quad (7)$$

where γ is the surface energy per unit area. In the general case

$$\sigma=\sigma_e\cos\phi+\sigma_s\sin\phi. \quad . \quad . \quad . \quad . \quad . \quad . \quad (8)$$

Table 2 lists values of σ_e and σ_s for various values of R, again considering copper as an example and taking γ to be $1{\cdot}4\times10^3$ dynes cm^{-2}. The resulting stresses are of the order of or greater than the yield strength.

Table 2. Effective Stress acting on a Dislocation Intersecting the Cylindrical Surface of a Copper Whisker

R (cm)	10^{-6}	10^{-5}	10^{-4}	10^{-3}
σ_e dynes cm^{-2}	$2{\cdot}4\times10^{9}$	$5{\cdot}1\times10^{8}$	$7{\cdot}8\times10^{7}$	$1{\cdot}1\times10^{7}$
σ_s dynes cm^{-2}	$2{\cdot}1\times10^{8}$	$2{\cdot}0\times10^{8}$	$3{\cdot}8\times10^{7}$	$5{\cdot}6\times10^{6}$

Therefore since the yield strength is thought to exceed the stress required to move a dislocation, the calculated stresses in all cases should suffice to drive the dislocation out of the whisker. When $\phi = 0$, the environment of the whisker will have no effect on the motion of the dislocation and it should slip completely out of the whisker. When $\phi > 0$ it is possible for the step formed when the dislocation intersects the surface to wind into a growth spiral (Burton *et al.* 1951), hindering the motion of the dislocation line out of the whisker and giving rise to growth perpendicular to the whisker axis. It is proposed that such perpendicular growth can give rise to growth forms which are deviants from the usual rod shape, such as blades, whisker branches, and kinks (Brenner 1956) and wheel shapes (Coleman and Cabrera 1957).

Finally, consider the situation at the tip of a growing whisker. As noted above, in addition to the elastic energy of the dislocation there will be an energy associated with the surface step which terminates at the point of intersection of the screw dislocation with the surface. This step energy is of the same order of magnitude per unit length as the energy per unit length of the dislocation. The step energy per unit length equals γa where a is the step height, equal to the screw component of the dislocation relative to the surface. If the partial pressures of components of the vapour phase with which the whisker metal can form compounds are less than the dissociation pressures of the compounds, γ is positive and the step energy will favour the decrease in length of the surface step. This condition obtains during the growth of a whisker from the vapour. If the partial pressure of a vapour phase component exceeds the dissociation pressure, γ is negative and the step energy will favour the increase of surface step length. This condition may arise during the removal of a whisker to atmospheric pressure and room temperature after growth has been terminated.

During whisker growth at a typical axial growth rate of $\sim 10^{-4}$ cm/sec, the surface step is rotating around the dislocation at a rate of about 10^4 revolutions per second. Thus during growth the step energy contributes no net force tending to drive the dislocation out of the whisker. However, when the growth rate is reduced by a decrease in supersaturation, the step energy term will contribute to the net force acting on the dislocation and the whisker tip will become a favourable site at which slip of the dislocation out of the whisker can occur. This provides another possible method of formation of growth kinks in whiskers.

Although the above calculations involve the approximations of isotropic elasticity theory and assume idealized shapes for whiskers and dislocation loops, the calculations show that it is possible for a dislocation both to persist in a metastable position in a whisker and so allow the whisker to grow, and later to slip out of the whisker and cause it to cease growing. Dislocations will slip out of whiskers of a critical radius but remain in whiskers of larger radius. Whiskers containing dislocations with an edge component greater than a critical fraction will not form. The theory predicts that dislocations with edge components with respect to the whisker axis should slip out of whiskers more easily than pure screw dislocations, and further that only dislocations with edge components will initiate the formation of growth variants when they slip out of whiskers. These latter two predictions should be relatively easy to test experimentally.

REFERENCES

BRENNER, S. S., 1956, *Acta Met.*, **4,** 62.
BRENNER, S. S., and SEARS, G. W., 1956, *Acta Met.*, **4,** 89.
BURTON, W. K., CABRERA, N., and FRANK, F. C., 1951, *Phil. Trans.*, **243,** 299.
COLEMAN, R. V., and CABRERA, N., 1957, *J. appl. Phys.*, **28,** 1360.
COMPTON, K. G., MENDIZZA, A., and ARNOLD, S. M., 1951, *Corrosion*, **7,** 327.
ESHELBY, J. D., 1953 a, *Phys. Rev.*, **91,** 755 ; 1953 b, *J. appl. Phys.*, **24,** 176.
FRANK, F. C., 1953, *Phil. Mag.*, **44,** 854.
KOEHLER, J. S., 1941, *Phys. Rev.*, **60,** 397.
NEWKIRK, J. B., and SEARS, G. W., 1955, *Acta Met.*, **3,** 110.
SEARS, G. W., 1953, *Acta Met.*, **1,** 457 ; 1955, *Ibid.*, **3,** 361, 367.
SEARS, G. W., and COLEMAN, R. V., 1957, *Acta Met.*, **5,** 131.
TREUTING, R. G., and ARNOLD, S. M., 1957, *Acta Met.*, **5,** 598.

Galvanomagnetic Properties of Cylindrical Fermi Surfaces†

By J. M. Ziman
Cavendish Laboratory, University of Cambridge

[Received June 4, 1958]

Abstract

An infinite cylinder has the same general properties, with respect to the connectivity of its plane sections, as the Fermi surface proposed by Pippard (1957) for copper. For this model, the conductivity tensor in an arbitrary magnetic field H is calculated exactly, and then averaged over all orientations of the cylinder axis relative to H. This is taken, without proof, to represent the bulk conductivity of a polycrystalline specimen. It agrees remarkably well, both at low and high fields, with the experimental results on copper, especially in making the transverse magnetoresistance proportional to H. This can be understood physically. There are always some crystallites, specially oriented to the field, where the orbits in k-space are open, or so extended that they are not traversed in the relaxation time. Since some of their conductivity components remain finite they provide leakage paths for the current but, as H increases, their number decreases as $1/H$. The observed saturation of the longitudinal magnetoresistance may also be explained by reference to the true Fermi surface and a slight sophistication of the model.

Since the experiments of Kapitza (1929) there has been difficulty in understanding the behaviour of the resistance of metals in very high magnetic fields. For many metals the magnetoresistance seems to be proportional to the field, whereas the most sophisticated modern theories suggest that it should either saturate, or, in special circumstances, increase as H^2 (e.g. Lifshitz, Azbel' and Kaganov 1956, to be denoted LAK). The mathematical problem is this: the magnetoresistance is an even function of H, and therefore tends to appear in any theory as a power series or algebraic function of H^2; how can it simulate a linear function over such a wide range? It will be shown that such behaviour can arise quite simply as a result of averaging the conductivity tensor over the mass of randomly oriented microcrystals in a polycrystalline specimen.

It will be recalled that the LAK theory depends upon the geometry of the path of the representative point of the electron state in k-space. In a magnetic field this point moves on the 'orbit' representing the intersection of a constant energy surface (in practice, the Fermi surface itself) with a plane normal to the direction of the magnetic field. It can easily be shown that the 'phase variable'

$$\phi=\omega_H \frac{c\hbar}{eH}\int\frac{dk}{v_\perp} \quad . \; . \; . \; . \; . \; . \; . \; . \; . \quad (1)$$

---

† Communicated by the Author.

(measuring dk along the orbit and $v_\perp$ the component of electron velocity normal to H) satisfies the equation of motion

$$\dot{\phi} = \omega_H. \qquad (2)$$

The parameter ω_H is a constant in time for a given orbit, but is proportional to H. If the orbit is closed, so that ϕ goes from 0 to 2π in a single circuit, it measures the fundamental frequency of rotation of the electron trajectory about the field. For free electrons

$$\omega_H = \frac{eH}{mc}. \qquad (3)$$

In terms of ϕ, one can derive a general formula for the conductivity tensor (Shockley 1950, Chambers 1952),

$$\sigma_{ij} = -e^2 \int \frac{1}{\omega_H} \frac{\partial f^0}{\partial \epsilon} \int_0^\infty v_i(\phi) \exp(-\phi'/\omega_H \tau) v_j(\phi + \phi')\, d\phi'\, \mathbf{dk}. \qquad (4)$$

The integral over $\mathbf{dk}$ sums all the electron states, labelled by the phase variable ϕ, by k_z (the coordinate parallel to H), and by the energy ϵ. The derivative of the Fermi distribution $\partial f^0/\partial \epsilon$ shows that only electrons on the Fermi surface need be counted. The scattering of electrons is represented, as usual, by a relaxation time τ, which appears here in its usual kinetic interpretation: $\exp(-t/\tau)$ is the probability of a particular state of motion surviving a time t, in which time, according to (2), the phase variable ϕ will have changed by the amount $\omega_H t$.

The discussion now hinges on the connectivity of the orbits. If, as in the free electron system, all cross sections of the Fermi surface are *closed*, then ω_H represents the frequency of a real cyclic process. LAK then show, from the terms which survive in (4) when

$$\eta = \omega_H \tau \gg 1 \qquad (5)$$

that the conductivity tensor must be of the form

$$\boldsymbol{\sigma} \sim \begin{bmatrix} \eta^{-2} A_{xx} & \eta^{-1} A_{xy} & \eta^{-1} A_{xz} \\ \eta^{-1} A_{yx} & \eta^{-2} A_{yy} & \eta^{-1} A_{yz} \\ \eta^{-1} A_{zx} & \eta^{-1} A_{zy} & A_{zz} \end{bmatrix} \qquad (6)$$

referred to axes with z parallel to H. The coefficients A_{xx}, etc. are asymptotically independent of η, and, when the resistivity tensor is calculated, it is found that all the components, except ρ_{xy} and ρ_{yz} (i.e. the Hall terms), tend to constant values. We say that the magnetoresistance *saturates* at high fields.

On the other hand, if, in certain orientations, all orbits are *open*, ω_H has no special significance, and the vanishing of the lower powers of η^{-1} in σ_{xx} or σ_{yy} is not guaranteed. There may then be special magnetoresistance components increasing quadratically as H^2 and not saturating.

To obtain any non-saturating effects there must be at least *some* open orbits in some orientations of the field. Let us think about the Fermi surfaces of real metals. In the alkali metals, where the Fermi surface is believed to be simply connected, like a distorted sphere, all orbits are closed, and (6) should hold. But, according to Pippard (1957), in copper the surface may touch the zone boundaries in the (111) directions (fig. 1). Because this structure is periodic in the reciprocal lattice, and because the motion of the representative point is continuous across the zone boundaries, in such a 'repeated zone scheme', we must repeat this figure endlessly, and look for its cross sections. Figure 2 shows the general effect. The surfaces have been schematized into four solid 'shafts' passing through the lattice along the four diagonals of the cube, with a sphere on each intersection (cube corners and centres).

Fig. 1

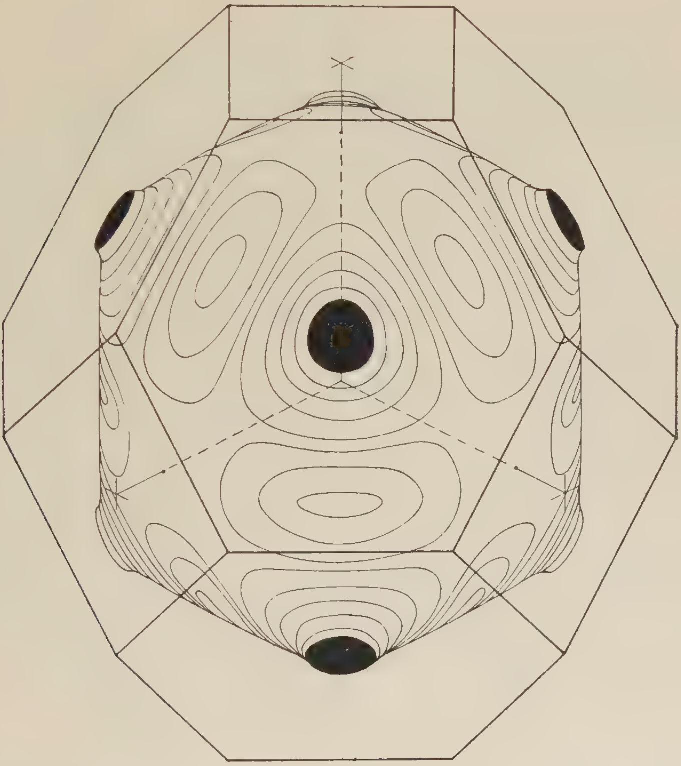

The Fermi surface of copper, according to Pippard (1957).

What is the connectivity of an arbitrary plane section of such a figure? In general we shall cut into, and across, the various 'shafts', and the orbits will run round the cut and close up. But, if the plane of section happens to be exactly parallel to the axis of one shaft, and not quite along the axis of another, the orbit will extend to infinity at either end. As the plane is rotated away from the axis, the orbit will close, then reduce in length until, at perpendicular incidence, it has its minimum perimeter.

Even the geometry of fig. 2 is too complicated for comfortable computation. A further simplification is shown in fig. 3, where the shafts have been thickened into cylinders whose intersections swallow the whole of the spherical part. From a topological point of view, this is equivalent to the true surface, but is still a little complicated analytically. Let us go the whole hog, and treat each cylinder separately, as if the Fermi surface were the sum of the four, without interference where they intersect. At least such a model preserves the character of the orbits. There are still special directions in which the orbits are open, and near these directions the orbits are closed, but very extended.

Fig. 2

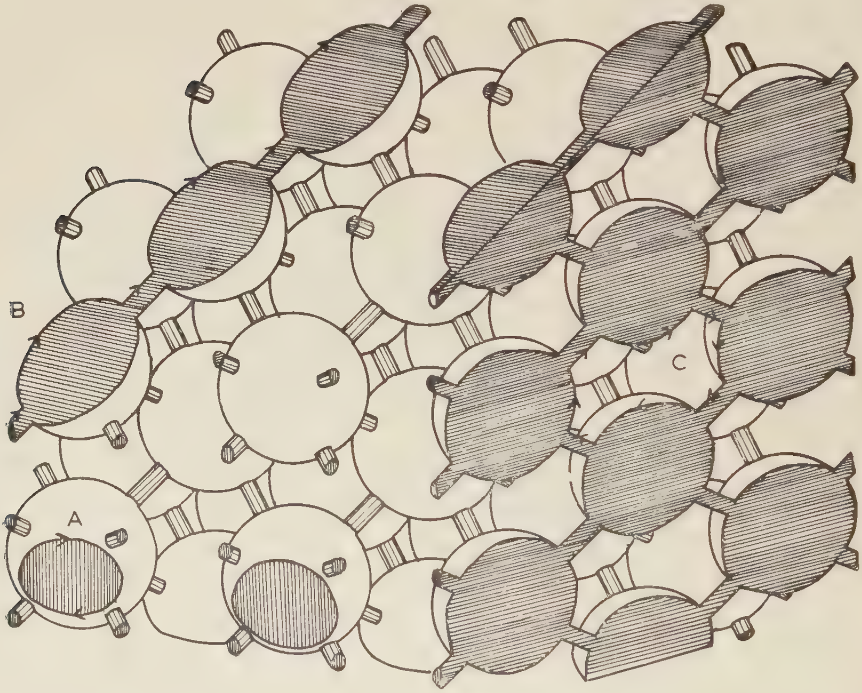

A simplified version of fig. 1, repeated in the reciprocal lattice and cut to show the various types of 'orbit'.
A, Typical closed orbit. *B*, Typical open orbit. *C*, Special closed orbit.

This simple model, with the Fermi surface merely the sum of four cylinders, can easily be analysed exactly. The electron velocity $\boldsymbol{v}$ is of constant magnitude, v_F, at all points. The sections are ellipses. The phase variable ϕ is just the azimuthal angle around the cylinder. If K is the radius of the cylinder, then the Larmor frequency for a field at an angle to the axis is

$$\omega_H = \frac{ev_F}{c\hbar K} H \cos\theta = \omega_H{}^0 \cos\theta. \quad . \quad . \quad . \quad . \quad . \quad . \quad . \quad . \quad (7)$$

This parameter $\omega_H{}^0$ is thus the maximum Larmor frequency occurring when the magnetic field is parallel to the axis of the cylinder. Putting this geometry into (4) we find

$$\sigma_{11} = \sigma_{22} = \frac{\sigma_c}{1+(\omega_H\tau)^2}\,; \quad \sigma_{12} = -\sigma_{21} = \frac{\omega_H\tau}{1+(\omega_H\tau)^2}\sigma_c, \quad . \quad . \quad . \quad (8)$$

Fig. 3

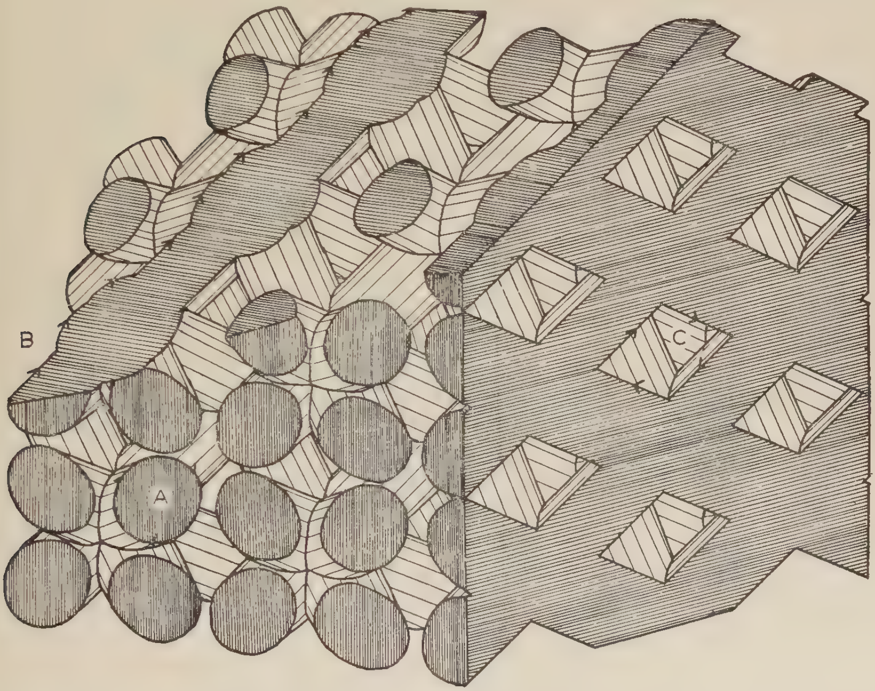

A system of intersecting cylinders having the same connectivity as fig. 2 and showing the same types of orbit.

where

$$\sigma_c = \frac{ne^2 v_F \tau}{\hbar K}. \quad . \quad . \quad . \quad . \quad . \quad . \quad . \quad . \quad . \quad (9)$$

These components of the tensor are for axes lying in the plane normal to the cylinder axis (along which, of course, σ is zero). (8) simply expresses the conductivity tensor of a 2-dimensional circular Fermi surface, subjected to the normal component $H \cos\theta$ of magnetic field; (9) is just the conductivity of such a 2-dimensional system of n electrons in zero field.

We are now to add the conductivities from four such cylinders, pointing into the (111) directions. This is not difficult to do, but leads to a great deal of complicated algebra when the tensor is inverted to obtain the resistivity. To show what can be done, fig. 5 is a plot of the extra resistance along the (100) direction as a magnetic field is rotated in the plane normal to this. Such a figure is comparable, in principle, with those drawn by Justi and Scheffers (1936) from their experiments on gold and other metals. The model is too crude to permit any serious interpretation, but at least shows a wide range of variation from minimum to maximum as is observed,.

Fig. 4

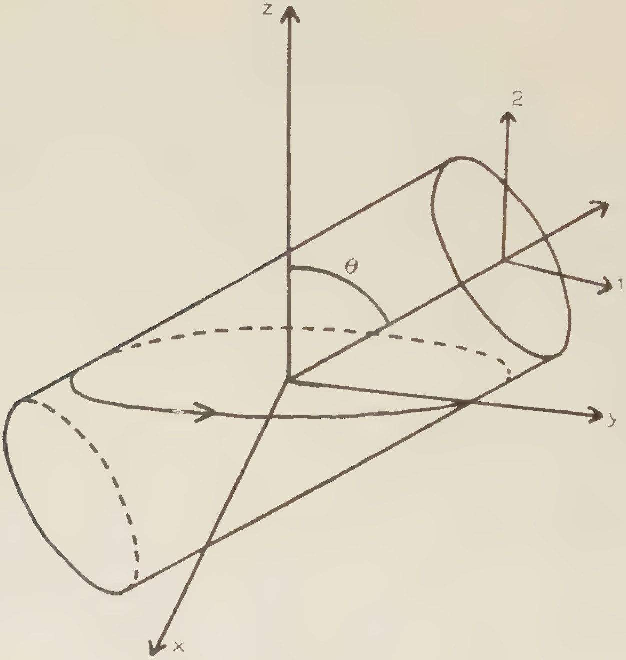

Geometry of the single-cylinder model.

But this is a calculation for a single crystal. The experiments at the highest fields have been made on polycrystalline specimens, where all crystal orientations with respect to the magnetic field may occur. How can we take account of this in the theory? The formal mathematical problem of calculating the over-all conductivity of a mixture of small domains, whose conductivity tensors are all pointing in different directions and are not even symmetric, is formidable. We are forced to make a guess. It could be plausibly argued that a reasonable approximation is simply to *take an average of the conductivity tensor itself, over all orientations* *of the crystal axes relative to the magnetic field.* This is the hypothesis upon which we now proceed. It is the crucial point in the theory, and it is unproven; it is only justified, *a posteriori*, by its remarkable consequences.

The mathematical argument is quite simple. Only one cylinder need be considered, since all four go through the same whole range of orientations. The typical term involves an integral over θ, with the weight function $\sin\theta$ for the solid angle, and the variation (7) of ω_H with θ. For example,

Fig. 5

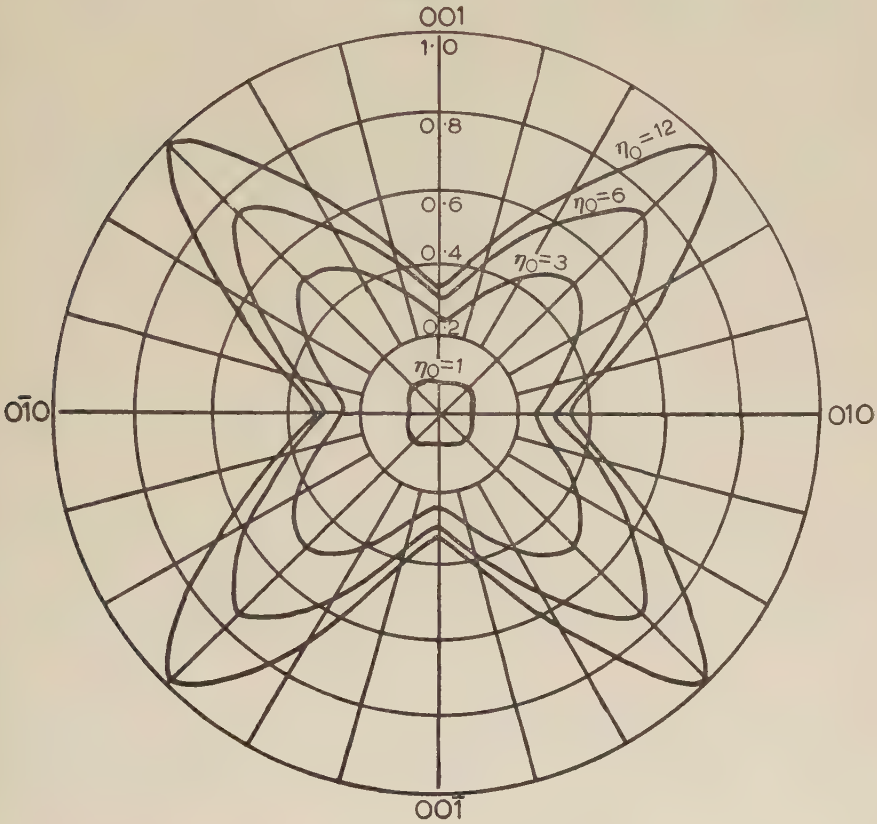

Resistance of a single crystal in the 100 direction, as a function of the orientation of a transverse magnetic field, calculated for a set of four cylinders with axes in the 111 directions.

$$\int_0^{\pi/2} \frac{\sin\theta\, d\theta}{1+(\omega_H\tau)^2} = \frac{1}{\omega_H{}^0\tau}\int_0^{\pi/2} \frac{\omega_H{}^0\tau \sin\theta\, d\theta}{1+(\omega_H{}^0\tau\cos\theta)^2}$$

$$= \frac{1}{\omega_H{}^0\tau}\tan^{-1}(\omega_H{}^0\tau). \qquad \dots\dots \quad (10)$$

In this way, we find

$$\left.\begin{aligned}\sigma_{xx}&=\frac{3}{4}\frac{\sigma_0}{\eta_0}\left\{\tan^{-1}\eta_0+\frac{1}{\eta_0}\left(1-\frac{\tan^{-1}\eta_0}{\eta_0}\right)\right\}=\sigma_{yy}\\ \sigma_{zz}&=\frac{3}{2}\frac{\sigma_0}{\eta_0}\left\{\tan^{-1}\eta_0-\frac{1}{\eta_0}\left(1-\frac{\tan^{-1}\eta_0}{\eta_0}\right)\right\}\\ \sigma_{xy}&=\frac{3}{2}\frac{\sigma_0}{\eta_0}\left\{1-\frac{\tan^{-1}\eta_0}{\eta_0}\right\}=-\sigma_{yx}\end{aligned}\right\} \quad . \quad . \quad (11)$$

in terms of $\sigma_0\ (=\frac{2}{3}\sigma_c)$, the zero field conductivity, which is just (9) smeared into three dimensions, and

$$\eta_0=\omega_H{}^0\tau=\frac{3}{2}\frac{\sigma_0}{nec}H \quad . \quad . \quad . \quad . \quad . \quad . \quad . \quad . \quad (12)$$

from (7) and (9).

Within the assumptions of the model, these formulae are exact at all field strengths; from them, the resistivity tensor may be derived by inversion. Let us look first at the low-field limit. To the lowest orders in η_0 we find

$$\left.\begin{aligned}\rho_{xx}&\sim\frac{1}{\sigma_0}(1+0\cdot15\eta_0{}^2\ldots)=\rho_{yy}\\ \rho_{zz}&\sim\frac{1}{\sigma_0}(1+0\cdot2\eta_0{}^2\ldots)\\ \rho_{xy}&\sim\frac{1}{2}\frac{\eta_0}{\sigma_0}\end{aligned}\right\} H\to 0. \quad . \quad . \quad . \quad (13)$$

These components show the correct qualitative behaviour. The magneto-resistance is proportional to $\eta_0{}^2$—that is, to H^2—and the Hall effect is linear in H. It is amusing to make a quantitative comparison with experiment. One can readily calculate that (12) gives for copper

$$\eta_0=0\cdot7\times10^{-6}\,sH \quad . \quad . \quad . \quad . \quad . \quad . \quad . \quad . \quad (14)$$

where s is the ratio of the conductivity in the experiment to the room temperature conductivity and H is measured in gauss. According to Kapitza (1929), the transverse magnetoresistance in low fields can be expressed in the form

$$\frac{\Delta\rho_\perp}{\rho_0}=0\cdot2(sH\times10^{-6})^2=0\cdot4\eta_0{}^2. \quad . \quad . \quad . \quad . \quad (15)$$

This is rather more than twice the value given by ρ_{xx} in (13). The experimental value of the longitudinal magnetoresistance is about 2/3 of the transverse effect; our model would make it 1/3 larger. As for the Hall coefficient, (12) and (13) give

$$R=0\cdot75\frac{1}{nec}. \quad . \quad . \quad . \quad . \quad . \quad . \quad . \quad . \quad . \quad . \quad (16)$$

The accepted experimental value (Chambers 1956) would seem to make the numerical coefficient about 0·67.

The point about these results is not that they prove that the cylindrical model is really a good description of the shape of the Fermi surface of copper, but that they give at least the correct order of magnitude of the quadratic part in the magnetoresistance. This gives us some confidence in going to the other limit of high fields. From (11) we easily deduce

$$\left.\begin{aligned} \rho_{xx} &\sim \frac{\pi/6}{1+(\pi/4)^2}\frac{\eta_0}{\sigma_0}=\rho_{yy} \\ \rho_{zz} &\sim \frac{4}{3\pi}\frac{\eta_0}{\sigma_0} \\ \rho_{xy} &\sim \frac{2/3}{1+(\pi/4)^2}\frac{\eta_0}{\sigma_0} \end{aligned}\right\} H\to\infty. \quad . \quad . \quad . \quad (17)$$

The most striking result is that all the components of the resistivity at high fields are proportional to H. For the transverse effect, in copper, (14) gives

$$\left(\frac{\rho_\perp}{\rho_0}\right)_{\text{theory}} \sim 0{\cdot}228\times10^{-6}\,sH. \quad . \quad . \quad . \quad . \quad . \quad . \quad (18)$$

The experimental results plotted by Chambers (1956) fit to a curve

$$\left(\frac{\rho_\perp}{\rho_0}\right)_{\text{expt}} \sim 0{\cdot}27\times10^{-6}\,sH, \quad . \quad . \quad . \quad . \quad . \quad . \quad . \quad (19)$$

whilst the data of Webber (unpublished) would make the ultimate slope of the line about $0{\cdot}2\times10^{-6}$.

The Hall coefficient at high fields should come out at

$$R_{\text{theory}}\sim0{\cdot}62\frac{1}{nec} \quad . \quad . \quad . \quad . \quad . \quad . \quad . \quad . \quad (20)$$

which is a bit less than the low field limit (16), and not in good agreement with the experimental high field value, which Chambers finds to be

$$R_{\text{expt}}\sim0{\cdot}83\frac{1}{nec}. \quad . \quad . \quad . \quad . \quad . \quad . \quad . \quad . \quad (21)$$

Another way of analysing the data is to compute the ratio of the components of the conductivity tensor. Our model gives

$$\frac{\sigma_{xy}}{\sigma_{xx}} \sim \frac{4}{\pi}=1{\cdot}27. \quad . \quad . \quad . \quad . \quad . \quad . \quad . \quad . \quad (22)$$

Chambers has plotted these two quantities (multiplied by H), from the experimental results, and finds the ratio reaching the value 1·15 at the highest fields, and still apparently increasing. In this respect, also, the model is thus quite consistent with experiment.

Only the longitudinal magnetoresistance needs some explanation. According to (17), we should find

$$\frac{\Delta\rho_{\parallel}}{\rho_0} \sim 0{\cdot}30\times10^{-6}\,sH. \quad . \quad . \quad . \quad . \quad . \quad . \quad . \quad (23)$$

In his experiments Webber has found that there is, indeed, a linear portion with slope of about $0{\cdot}07 \times 10^{-6}$, until sH reaches about 10^7 gauss. Then the curve bends over, and saturates to a value almost exactly unity. That is, the conductivity along the magnetic field cannot be made to fall below half its original value.

The reason for this discrepancy in the behaviour of the model may be as follows. The conductivity along the magnetic field is due to the component of electron velocity in that direction. In a free electron system, this component is unaltered by the magnetic field, and the longitudinal conductivity is independent of H. In the cylindrical model, however, this behaviour only occurs for certain special orientations of the cylinder, when it is exactly transverse to the magnetic field. Otherwise, the electron is carried round the orbit, and its average velocity, in any direction, tends to zero as ω_H increases. The real Fermi surface is different from the cylindrical model in this respect. It is probably more or less doubly convex in most directions, so that there are, in addition to the cylindrical sections, also many orbits running round the edges of slices from the 'cheeks' of the apple. (These might be, for example, some of the contours on fig. 1, or orbit A in fig. 2.) On these orbits, there is usually a large net component of electron velocity outwards—that is, along H.

It is not difficult to modify the model to show this behaviour. The Fermi surface in fig. 2 can be supposed, approximately, to consist of independent cylinders and spheres. That is, one adds to (8) and to (11) the conductivity tensor of a sphere. At high fields this contributes to σ_{xy} and σ_{zz}, but not to σ_{xx} and σ_{yy}. In effect, the saturation value of the longitudinal conduction would be just the conductivity of the sphere alone. One can show that this would raise the theoretical value of R in (20), without too drastically lowering the coefficient in (18)—only (22) would tend to be increased. However, since we are not supposing our model to be quantitatively correct in detail, this programme need not be pursued further.

To sum up, it may be said that we have found a mathematical procedure, with a plausible physical interpretation, that is capable of combining the two theoretical types of behaviour of the components of resistivity—quadratic in H, and saturating—into a linear function of H. This is just the integral (10). It is really a question of how one goes to the limit of high fields. In a given specimen of polycrystalline metal there are always some crystallites whose cylinder axes are so nearly perpendicular to the field direction that their orbits are not closed in the time τ. These crystallites provide leakage paths for the current. As the field increases, the number of these special domains decreases proportionately to $1/H$, but H can never be so high that all orbits are forced out of action.

However, at the heart of the argument there still remains the question of justifying the averaging procedure. This seems a problem of quite another order of magnitude of mathematical difficulty. The only excuse for offering the present calculation is that by trivial mathematical analysis it gives results which are extraordinarily close to the galvanomagnetic properties of a real metal without any need to modify the usual assumptions of the validity of the Lorentz force equation and the existence of a simple relaxation time.

ACKNOWLEDGMENTS

I am indebted to Dr. Webber for his unpublished experimental data, and to Dr. Pippard for his picture of the Fermi surface of copper, and some healthy criticism.

REFERENCES

CHAMBERS, R. G., 1952, *Proc. phys. Soc. Lond.* A, **65,** 458; 1956, *Proc. roy. Soc.* A, **238,** 344.

JUSTI, E., and SCHEFFERS, H., 1936, *Z. Phys.*, **37,** 383, 475.

KAPITZA, P., 1929, *Proc. roy. Soc.* A, **123,** 292.

LIFSHITZ, I. M., AZBEL', M. YA., and KAGANOV, M. I., 1956, *J. exp. theor. Phys.*, **31,** 63.

PIPPARD, A. B., 1957, *Phil. Trans.* A, **250,** 325.

SHOCKLEY, W., 1950, *Phys. Rev.*, **79,** 191.

The Ductile–Brittle Transition in the Fracture of α-Iron: II[†]

By J. HESLOP[‡] and N. J. PETCH
Metallurgy Department, Houldsworth School of Applied Science,
University of Leeds

[Received March 5, 1958]

ABSTRACT

The expressions obtained in a previous paper for the fracture–mode transition temperature at a notch are shown to agree well with experimental measurements of its variation with grain size and with the friction on a free dislocation. A calculation is given of the effect of the dislocation locking strength on the transition temperature and this is in reasonable agreement with the observed temperatures for steels with weakened locking due to the presence of manganese. It is suggested that strain and strain-ageing raise the transition temperature because of the increased tensile stress available at fracture for the propagation of a dislocation crack.

§ 1. INTRODUCTION

IN Part I (Petch 1958), the transition in mode of fracture from ductile to cleavage was examined. It was thought that fracture arises from cracks formed by the coalescence of dislocations and that the transition to cleavage occurs when the tensile stress at fracture becomes capable of propagating such a crack as a Griffith crack. It was concluded that the temperature-dependence of the ductile–cleavage transition at a notch probably arises more from that of the stress required to move a free dislocation than from the temperature-dependence of the locking of a dislocation source. Lowering the temperature increases this friction on a free dislocation and so increases the fracture stress and this, in turn, favours cleavage.

Two expressions were obtained for the transition temperature T_c at a notch. First, with rigidity nodulus μ and grain diameter l,

$$\beta T_c = \ln B - \ln\left(\frac{4q\mu\gamma'}{k^*} - k^*\right) - \ln l^{-1/2}. \quad . \quad . \quad . \quad . \quad (1)$$

Here, β and B are the constants in

$$\ln \sigma_0 = \ln B - \beta T,$$

which expresses the temperature dependence of σ_0, the stress required to move a free dislocation. The term γ' is a modification of the surface energy to allow for the plastic work that accompanies the opening of a crack and $q \simeq \frac{1}{3}$ is the triaxiality factor for the stresses near the notch. Finally, k^* is the slope in the expression for the uniaxial ductile fracture stress σ_f of polycrystals,

---

[†] Communicated by the Authors.
[‡] Now at the Mond Nickel Co. Ltd., Birmingham.

$$\sigma_f = \sigma_0 + k^* l^{-1/2}. \qquad \text{(2)}$$

Less accurately than in (1), σ_0 may be divided into a temperature-independent part $\sigma_0{}^*$ and a part that varies linearly with temperature, so giving

$$\sigma_0 = \sigma_0{}^* + C - \epsilon T,$$

where C and ϵ are constants. From this,

$$\epsilon T_c = \sigma_0{}^* + C - \left(\frac{4q\mu\gamma'}{k^*} - k^*\right) l^{-1/2}. \qquad \text{(3)}$$

In the present paper, the predictions from these expressions for the transition temperature are examined experimentally.

Fig. 1

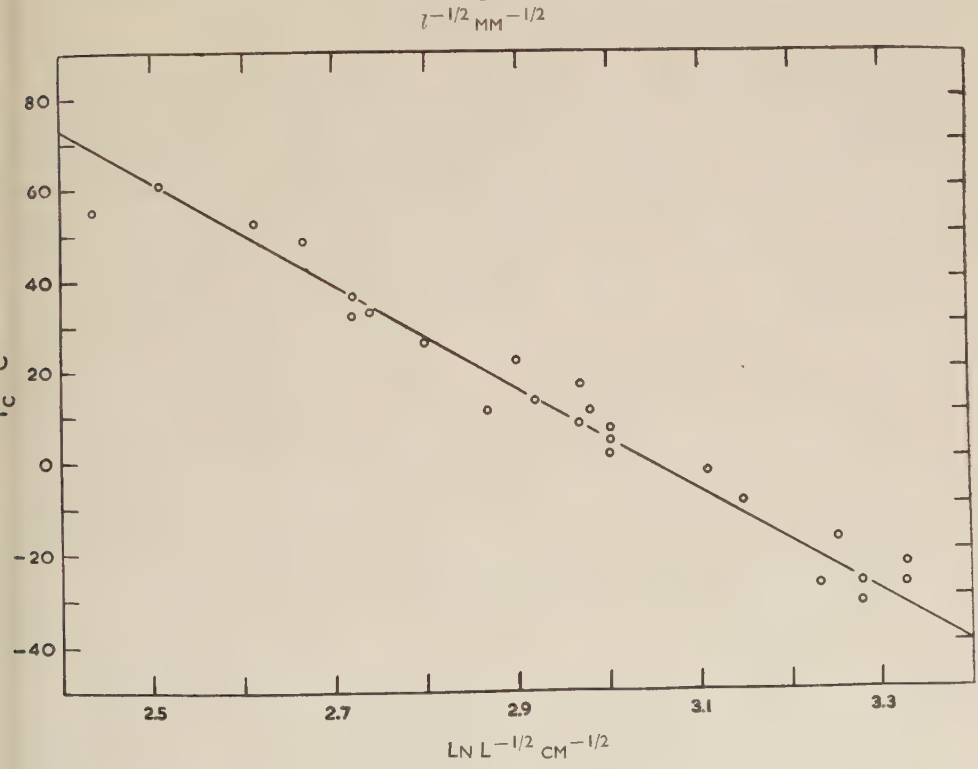

The influence of grain size on the transition temperature.

§ 2. The Effect of Grain Size

The larger the grain, the larger the dislocation crack produced. This favours cleavage. A linear dependence of T_c on $\ln l^{-1/2}$ is predicted in (1) and on $l^{-1/2}$ in (3). To check this, measurements of the transition temperature were made for a mild steel over a wide range of grain size using

5/16 in. diameter V-notched specimens in a Charpy-type impact test. The analysis of the steel (weight %) was 0·11 C, 0·51 Mn, 0·02 Si, 0·05 S, 0·03 P, 0·008 N_2.

The variation in grain size was obtained by annealing at various temperatures up to 1200°c for times up to 36 hours and the transition temperature was taken at 75% cleavage, which occurred close to an energy consumption in fracture of 10 ft. lb.

Figure 1 shows that T_c does vary linearly with $\ln l^{-1/2}$ in agreement with (1). The variation with $l^{-1/2}$ is also close to linear.

To examine the agreement with eqns. (1) and (3) further, the temperature-dependence of the friction stress σ_0 is required, so that the values of β, B etc. are known. Moreover, these are required at the strain-rate experienced ahead of an advancing ductile fracture in the notch, which is estimated as a rate of at least 10^3 sec^{-1}, probably more.

Information about σ_0 at the lower yield point $\sigma_{\text{l.y.p.}}$ is given by

$$\sigma_{\text{l.y.p.}} = \sigma_0 + kl^{-1/2}, \qquad . \quad . \quad . \quad . \quad . \quad . \quad . \quad . \qquad (4)$$

where k is a constant.

The lower yield points at −79°c in fig. 2 show the variation of σ_0 (the intercept at $l^{-1/2} = 0$) within the strain-rate range available with a geared testing machine. Considerable dependence of σ_0 on strain rate is evident†. Use of the rather special techniques that would be necessary to obtain values at higher rates has not been attempted in the present work and instead Baron's (1956) measurements have been used. From these, the following in c.g.s. units have been deduced for the temperature range of about 0 ± 50°c.

$$\beta = 0{\cdot}62 \times 10^{-2} \qquad \ln B = 23{\cdot}4$$

$$\epsilon = 2{\cdot}0 \times 10^{7} \qquad C = 79 \times 10^{8}.$$

These values are obtained from the lower yield point and in applying them here the effect of the plastic strain prior to fracture in a notch at the transition temperature is neglected. The strain rate in Baron's measurements was 10^2 sec^{-1}, which still is slower than that ahead of an advancing ductile fracture. This will not have much effect on β or $\ln B$, but the values taken for ϵ and C may be somewhat low.

A quantitative check on the grain size dependence of T_c can now be made. In (1), the reciprocal of the slope of the transition temperature-grain size relationship is simply $-\beta$, so the calculated value from above is $-0{\cdot}62 \times 10^{-2}$ c.g.s. units, which compares quite well with the observed value from fig. 1 of $-0{\cdot}88 \times 10^{-2}$. What difference there is may in part reflect some temperature variation of the dislocation locking strength, which was taken as invarient over the temperature range of interest in deducing (1). Strengthening of the locking at the lower temperatures will raise T_c.

---

† Previous work on the influence of strain-rate on the yield of α-iron has considered only the effect on the unlocking of a dislocation source, which controls the value of k. The most strain-rate dependent term is however σ_0 and this has two parts (Heslop and Petch 1956), one of which should be independent of strain-rate.

From the intercept at $\ln l^{1/2}=0$ in fig. 1 and taking $\ln B=23\cdot4$, $\ln[(4q\mu\gamma'/k^*)-k^*]=18\cdot0$ in eqn. (1). With $k^*=2\cdot0\times10^8$ c.g.s. units (Petch 1956) and $q=\frac{1}{3}$, the effective surface energy γ' is obtained as 50 000 ergs cm^{-2}.

Fig. 2

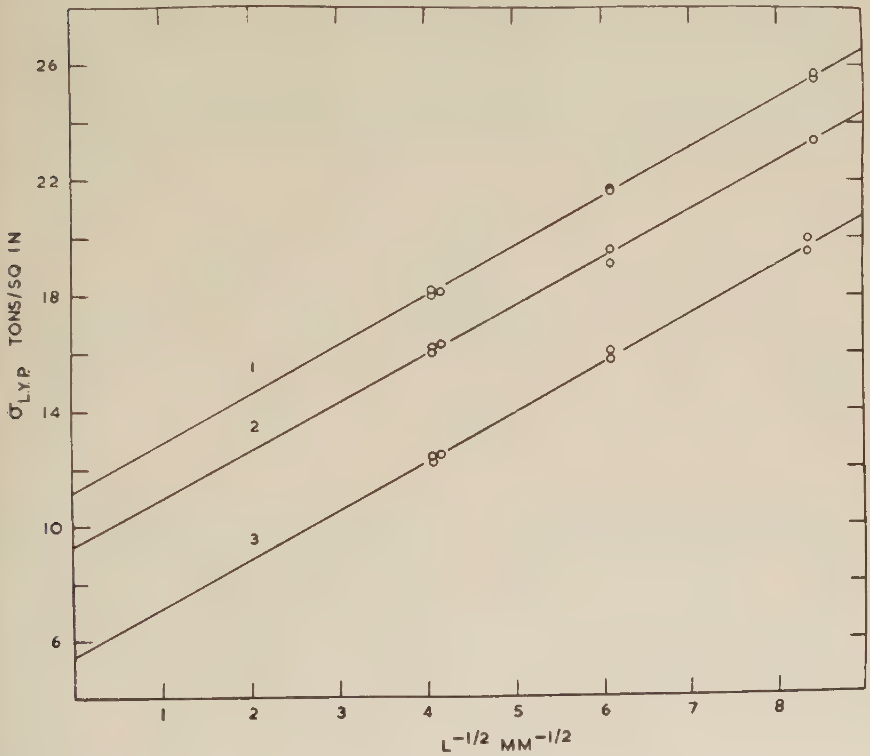

The influence of strain rate on the lower yield point at −79°c. The rates are (1) 2×10^{-3}, (2) 2×10^{-4}, (3) 1×10^{-6} sec^{-1}.

§ 3. The Effect of the Temperature-Independent σ_0*

The temperature-independent part of σ_0 is due to the resistance to the motion of a free dislocation arising from interaction with carbon, nitrogen or other alloy atoms, with precipitates or with lattice defects (Cracknell and Petch 1955). Thus, σ_0* varies, for example, with alloying, with sub-critical quenching (which increases the amount of carbon in solution in the ferrite), with quench-ageing and with variation in the phosphorus and nitrogen contents.

An alteration of σ_0* in one of these ways produces a direct alteration in the lower yield point, eqn. (4). The effect on the ductile fracture stress, eqn. (2), is less certain, because the change made to alter $\sigma_0{}^*$ may also alter the strain at fracture, and the strain-hardening itself contributes to the value of $\sigma_0{}^*$ at fracture.

This is examined in table 1, which shows the effect of raising $\sigma_0{}^*$ by quench-ageing. These measurements are at constant grain size on the same steel as in § 1. The increase in the ductile fracture stress is only slightly less than the increase in the lower yield point and the difference between the two increases is close to what would be expected from the known strain-hardening rate and the reduction in the fracture strain by the quench-ageing. In fracture at a notch, the influence of fracture strain is probably less, so treatments that increase $\sigma_0{}^*$ at the lower yield point should increase $\sigma_0{}^*$ at fracture by very closely the same amount. This will increase the stress available at fracture for Griffith propagation of dislocation cracks and so favour cleavage.

Table 1. The Effect of Quench-Ageing on the Ductile Fracture Stress at 18°c

Treatment	Lower yield point (tons in $^{-2}$)	Fracture stress (tons in $^{-2}$)	Redtn. in area (%)
Anneal	13·0	51·0	68
Quench from 700°c ; age 20 hr 50°c	28·0	64·8	56

From (3), the increase in the transition temperature from an increase in $\sigma_0{}^*$ at fracture is simply $\Delta\sigma_0{}^*/\epsilon$. Using the value of ϵ for a strain-rate of $10^2\,\text{sec}^{-1}$, the calculated increase in T_c due to an increase of 1 ton in^{-2} in $\sigma_0{}^*$ is 7·5°c. This is probably an over-estimate, since, as already mentioned, the strain rate ahead of an advancing ductile fracture is probably greater than $10^2\,\text{sec}^{-1}$, so the value used for ϵ is probably too low.

To check this calculation, the effects on T_c of alteration in $\sigma_0{}^*$ by sub-critical quenching, quench-ageing, over-ageing and nitriding were determined (table 2). The same steel was used as in § 1 and the $\sigma_0{}^*$ increase was obtained from the lower yield point.

Table 2. The Effect of $\sigma_0{}^*$ on T_c

Treatment	T_c Increase (°c)	$\sigma_0{}^*$ increase (tons in^{-2})	$\dfrac{\Delta T_c}{\Delta\sigma_0{}^*}$
Quench from 650°c	15	3·0	5·0
Quench from 690°c	22	4·7	4·7
Quench from 700°c ; age 20 hr, 50°c	61	15·0	4·1
Quench from 690°c ; over-age 150°c	7	1·5	4·7
Nitride 580°c ; quench	18	3·6	5·0

From table 2, it will be seen that an increase in $\sigma_0{}^*$ does raise the transition temperature in the way expected and that a 1 ton in^{-2} increase produces a rise of 4·7°C.

It seems probable that this effect of $\sigma_0{}^*$ on T_c must be an important factor in the variation of transition temperature observed amongst industrial steels. For example, the difference between Bessemer and Open Hearth steels must lie partly in the $\sigma_0{}^*$ difference due to different nitrogen contents. An increase of 0·01% nitrogen in solution increases $\sigma_0{}^*$ by 2·9 tons in^{-2} (Cracknell and Petch 1955) and this should raise the transition temperature by 14°C at constant grain size.

Churchman *et al.* (1957) have recently shown that irradiation increases $\sigma_0{}^*$. In their experiments an increase of $\sigma_0{}^*$ by 25 000 lb in^{-2} corresponded to a rise in the transition temperature of about 60°C. On the basis of the present measurements, a rise of 52°C would be predicted.

§ 4. THE EFFECT OF DISLOCATION LOCKING

The easier the operation of a dislocation source, the greater is the amount of plastic work that accompanies the opening of a crack, so the larger is the effective surface energy γ' and the lower is the transition temperature, eqn. (1).

An estimate of the effect on T_c of alteration in the dislocation locking strength can readily be made.

Taking the shear stress to operate a dislocation source as $\sim 1\times 10^{10}$ dynes cm^{-2} and the number of dislocations in a dislocation crack as ~ 500, from Stroh's (1954) analysis, the stress around the dislocation crack is sufficient to operate sources up to a distance of $\sim 1\times 10^{-4}$ cm from the crack tip. The length c of the dislocation crack that just does not break out across the crystal is $\sim 1\times 10^{-4}$ cm (Petch 1958). Thus, if r is distance from the crack tip and $r_{\max}$ is the maximum value for the operated sources, $r_{\max}\sim c$.

At this distance from the crack, the concentration of the applied stress is negligible and the stress produced is principally due to the wedging by the dislocations in the crack. Thus, with a crack length c, in the vicinity of $r_{\max}$ the dependence of the shear stress on r will be between $r^{-1/2}$ (for $r \ll c$) and r^{-1} (for $r \gg c$). Then, if τ is the shear stress required to operate a source,

$$r_{\max}=\text{const.}\,\tau^{-\alpha},$$

where $\alpha=1$–2, and, taking the effective surface energy γ' as proportional to $r_{\max}$,

$$\gamma'=\text{const.}\,\tau^{-\alpha}.$$

Information about τ is given by the slope k in

$$\sigma_{\text{l.y.p.}}=\sigma_0+kl^{-1/2},$$

since k indicates the shear stress that must be generated ahead of a dislocation pile-up to propagate yield from one grain to the next. It seems probable that $\tau = \text{const.}\, k$. Thus

$$\gamma' = \text{const.}\, k^{-\alpha} \quad . \quad . \quad . \quad . \quad . \quad . \quad . \quad . \quad . \quad (5)$$

at the critical stage in the break-out of the crack.

This permits an estimate of the effect on T_c of alteration in the locking strength. Such an alteration can arise from composition changes. For instance, the presence of manganese weakens the locking (Heslop and Petch 1957), locking by nitrogen appears to be stronger than by carbon and by boron is stronger still (Codd and Petch, unpublished). Along with these changes in the locking strength, there are changes in T_c.

With a 1·9% Mn steel, k is reduced at room temperature to 0·83 of its value for low manganese steels such as the one used for the present paper (Heslop and Petch 1957). Using (5) and the data for γ' and β from fig. 1, γ' is increased by the manganese from 50 000 ergs cm^{-2} to 60 000–72 000 ergs cm^{-2}, corresponding to $\alpha = 1$–2. From (1), this causes a decrease of T_c by 66–110°C. On the other hand, the presence of the manganese increases $\sigma_0{}^*$ at the lower yield point by 4·5 tons in^{-2}, which will raise T_c by 21°C, so that a nett decrease of 45–90°C is predicted. The observed decrease at constant grain size is 43°C†.

In this calculation, the opposition to the T_c lowering by $\sigma_0{}^*$ increase is possibly somewhat under-estimated. The lowering of the yield point due to the weaker dislocation locking may increase the strain at fracture and so lead to some further increase in $\sigma_0{}^*$ at fracture from the additional strain-hardening.

§ 5. THE EFFECT OF STRAIN AND STRAIN-AGEING

Strain hardening increases the friction stress $\sigma_0{}^*$ and on ageing there is a further increase probably due to precipitation. Such an increase produced by pre-straining at room temperature also increases the fracture stress on subsequently testing in liquid nitrogen, provided the residual ductility at the low temperature is small (Patwardhan 1953). Straining and ageing produces the same result. The increase in the fracture stress appears to be somewhat less than the $\sigma_0{}^*$ increase in the pre-treatment. These effects are more complicated if the residual ductility in liquid nitrogen is high; then, at high pre-strains, there may even be a decrease in the total strain to fracture and in the fracture stress.

If strain or strain-ageing is followed by a notched impact test instead of a low temperature tensile test, it seems probable that again the fracture stress must be raised, for cleavage is favoured and the transition temperature is raised.

---

† The 75% cleavage criterion gives transition temperatures that are a little above those in Heslop and Petch (1957).

Table 3 shows some measurements on the influence of strain and strain-ageing on the transition temperature. In this, $\Delta\sigma_0^*$ in the pre-treatment is taken equal to the work-hardening or, for the aged specimens, to the difference between the initial and final lower yield points.

Table 3. The Effect and Strain-Ageing on T_c

Material	Grains mm^2	Treatment	Increase in T_c (°c)	Pre-treatment increase in σ_0^* (tons in^{-2})	$\frac{\Delta T_c}{\Delta\sigma_0^*}$
Swedish Iron	220	Strain 2%	9	2·1	4·3
	540		9	1·9	4·7
Mild Steel	1350		13	2·3	5·7
	3000		14	2·2	6·4
Swedish Iron	220	Strain 2%; Age	25	5·5	4·5
	540		26	5·3	4·9
Mild Steel	1350		28	5·0	5·6
	3000		27	4·6	5·8
Swedish Iron	220	Strain 10%	24	9·7	2·5
	540		25	9·8	2·6
Mild Steel	1350		28	10·0	2·8
	3000		22	9·9	2·2
Swedish Iron	220	Strain 10%; Age	47	15·2	3·1
	540		49	15·0	3·3
Mild Steel	1350		47	14·9	3·1
	3000		45	14·1	3·2

At 2% strain, with or without ageing, ΔT_c/pre-treatment $\Delta\sigma_0^*$ is ~5°c/ton in^{-2}, which is close to the $\Delta T_c/\Delta\sigma_0^*$ value previously observed in table 2, so this suggests that the strain increases σ_0^* at fracture in the notch by an amount close to the σ_0^* increase in the pre-treatment.

At 10% strain, ΔT_c/pre-treatment $\Delta\sigma_0^*$ is down to 2·5°c/ton in^{-2}, so it seems that the increase in σ_0^* at fracture is now less than the σ_0^* increase in the pre-treatment. The change in T_c on subsequent ageing corresponds to a $\Delta T_c/\Delta\sigma_0^*$ of 4·4°c/ton in^{-2}, which suggests that most of this increase in σ_0^* is carried through to the fracture stress.

§ 6. THE TRIAXIALITY FACTOR

A change from notched to un-notched specimens changes the factor q, introduced by the triaxiality of the tension at a notch, from $\frac{1}{3}$ to unity. This reduces the tensile stress available at fracture for Griffith propagation of a dislocation crack and so favours ductile fracture. From (1), using the values of β and γ' given by fig. 1, such a change in q will lower T_c by 248°c. With a medium grain size, this is to about −250°c.

In practice, the un-notched specimens should become brittle above -250°c. Measurements of the slope k in the lower yield point eqn. (4) indicate that the dislocation locking strengthens rapidly below about -150°c, and this will ensure that the steel becomes brittle in the -150°c to -250°c range as the temperature is lowered in response to the change in q. This agrees with the known behaviour of un-notched specimens.

REFERENCES

BARON, H. G., 1956, *J. Iron St. Inst.*, **182,** 45.
CHURCHMAN, A. T., MOGFORD, I., and COTTRELL, A. H., 1957, *Phil. Mag.*, **2,** 1271.
CRACKNELL, A., and PETCH, N. J., 1955, *Acta Met.*, **3,** 186.
HESLOP, J., and PETCH, N. J., 1956, *Phil. Mag.*, **1,** 866 ; 1957, *Ibid.*, **2,** 649.
PATWARDHAN, M. K., 1953, *Ph.D. Thesis*, Leeds University.
PETCH, N. J., 1956, *Phil. Mag.*, **1,** 186 ; 1958, *Ibid.*, **3,** 1089.
STROH, A. N., 1954, *Proc. roy. Soc.* A, **223,** 404.

The Intensity Profiles of Electron Diffraction Lines†

By T. B. RYMER and F. J. FAYERS‡
The University, Reading

[Received in revised form May 22, 1958]

ABSTRACT

The paper discusses the intensity profiles of electron-diffraction rings from a polycrystalline specimen with random orientation. Theoretical expressions are given for the profiles due to (*a*) the finite size of the crystals, (*b*) random stresses in the specimen, (*c*) dynamical refraction. The profiles of diffraction rings formed by specimens of vacuum-evaporated lithium fluoride and gold have been studied using an electron-diffraction camera and microphotometer capable of a resolution better than 10 μ. It is found that the profiles of lithium fluoride diffraction rings are consistent with the assumption that the crystals are cylinders of diameter ~ 140 Å having their axes normal to the specimen plane and subject to random stresses in the plane of the specimen having a standard deviation $\sim 4 \times 10^9$ dyn/cm^2. The profiles of gold diffraction rings are consistent with the assumption that the width of the rings is due to dynamical refraction by crystals bounded by parallel (100) faces and subject to random stresses in the plane of the specimen having a standard deviation $\sim 10^{10}$ dyn/cm^2.

§ 1. INTRODUCTION

ELECTRON diffraction rings from a polycrystalline specimen have a width which may be due to any or all of the following: (*a*) instrumental effects, (*b*) the finite size of the crystals, (*c*) refraction at crystal facets due to the inner potential of the crystals and dynamical refraction effects, and (*d*) variations of lattice constant from one crystal to another due, for example, to random stresses in the specimen. Inhomogeneous stresses in a crystal due to imperfections produce an effect similar to (*d*). Examples of most of these effects occur in the literature, but few attempts have been made to see whether the intensity profile of a continuous diffraction ring can be assigned to a particular type of broadening. Most authors have assigned the widths of diffraction rings to a combination of instrumental effects and finite crystal size, with a cautionary note that the crystal sizes they derive may be grossly in error.

In the present paper we describe an attempt to determine the profiles of diffraction rings and to give a theoretical interpretation of them. The study has been confined to specimens of vacuum evaporated lithium fluoride and gold. These substances were chosen partly because they give continuous ring patterns, but mainly because these patterns have already been the subject of extensive study (Halliday *et al.* 1954, Rymer 1956).

---

† Communicated by the Authors.
‡ Now at California Research Corporation, La Habra, California, U.S.A.

Instrumental effects (*a*) were rendered negligible by the use of a high-resolution diffraction camera and microphotometer, leaving (*b*), (*c*) and (*d*) as potential sources of broadening. We shall show that the widths of lithium fluoride rings are due to the finite size of the crystals (*b*) and strains in the specimen (*d*); the widths of gold rings on the other hand are due to dynamical refraction effects (*c*) and strains (*d*).

§ 2. Experimental Technique

The diffraction rings studied were those of transmission specimens of lithium fluoride and gold prepared by vacuum evaporation. Using the usual 50 cm specimen-to-plate distance, the widths of the diffraction rings from such specimens is $\sim 200\,\mu$. If instrumental effects are to be negligible, the size of the focused electron beam at the plate should not exceed about $10\,\mu$. A similar limitation applies to the width of the slit of the microphotometer used to measure the plate.

The only practicable method of obtaining a sufficiently small focused electron beam is by the use of a high-resolution camera using two magnetic lenses (Cowley and Rees 1953, Ehlers 1956). The best arrangement is to have one lens situated just above the specimen and the other, a short-focus condenser lens, half way between the specimen and the electron source. The camera used had a specimen-to-plate distance 50 cm and a source-to-specimen distance 90 cm. The condenser lens had a focal length of 2 cm. The electron gun was of the type studied by Haine and Einstein (1952) and operated with a fixed bias voltage just above cut-off. Assuming the diameter of the source in such a gun to be $25\,\mu$, the calculated value of the focused spot on the photographic plate is $1{\cdot}3\,\mu$. If the spot is not to oscillate to and fro on the plate, it is necessary that alternating magnetic fields from other apparatus in the laboratory shall not exceed about 10^{-5} gauss amplitude at the camera, and that the high-tension and lens current supplies shall be stabilized to 1 or 2 parts in 10^4 during the 3–5 minutes of an exposure. The stray magnetic fields were eliminated partly by enclosing the whole camera in a large cylindrical mumetal shield and partly by removing the most powerful sources to an adequate distance from the camera.

The adequacy of the precautions mentioned was checked by making exposures in the absence of a specimen when a 1000 c/s alternating potential of a few hundred volts was applied to a pair of deflecting electrodes mounted immediately below the position normally occupied by the specimen. The resulting line trace was examined with a microscope or microphotometer and found to be $5\text{-}10\,\mu$ wide. This represents the combined effect of the width of the focused spot and of any movement of the beam. Successive traces made on the same plate at intervals of 5 minutes were usually coincident, showing that the beam was generally steady over the period of a normal exposure. Occasionally, however, two such traces were about $40\text{–}50\,\mu$ apart. The cause of such movements of the beam could not be determined with certainty, but it was probably due to a slight charge on a carbonaceous deposit on one of the diaphragms. In order to be sure that such a beam movement did not occur while photographing a diffraction pattern, a voltage was applied to the deflector plates for a fraction of a second before and after the main exposure in such a way that the undiffracted beam produced a uniform linear trace superposed on the main pattern. The duration of the voltage pulses was such that the trace formed by the movement of the central spot was suitable for microphotometry; the diffraction rings, which of course are deflected along with the central spot, produce no appreciable photographic effect during this period. Photographs were rejected if the linear trace appeared broad or doubled. For convenience in producing the linear trace the undiffracted beam was allowed to fall on the photographic plate throughout the exposure. This will produce an electrostatic charge on the plate resulting in a distortion of the diffraction pattern. It can however be deduced from the data of Rymer and Butler (1945), who first studied this effect, that although the radii of the diffraction rings are slightly increased, the effect on the intensity profile is entirely negligible.

It is necessary that the substrate on which the specimen is mounted should not cause appreciable scattering. Tests with the thinnest cellulose films showed that the beam width at the plate after passing through the material was $\sim 40\,\mu$, showing that this is an unsuitable substrate material. Carbon films prepared by Bradley's (1954) technique generally gave less scattering than cellulose films: with the thinnest possible carbon films there was only some general background scattering without perceptible line broadening. Such films were therefore used as a substrate for lithium fluoride specimens. Gold specimens required no substrate: the metal was evaporated on to a glass slide coated with Bedacryl 122X, the resulting film was stripped from the glass and the Bedacryl dissolved off.

The photographic plates were measured with a Vickers projection microscope converted (Tomlin and Fayers 1955) into a non-recording microphotometer. Ilford Thin Film Half Tone plates were used; these had been found by Butler (1945) to have a linear relation between exposure and density up to densities of at least 1. By using the microphotometer to examine the shadow of a knife-edge cast by the electron beam on the photographic plate, it was verified that the combined effect of the finite size of the microphotometer slit and of scattering of electrons within the emulsion amounted to an overall width of less than $10\,\mu$.

The microphotometer records were corrected to intensity profiles as follows. If i is the photocell reading when set at any part of the line, and i_B is the reading corresponding to the diffuse background, the intensity of that part of the line is proportional to $\log i_B - \log i$. Log i_B is determined by linear interpolation between readings taken at the two extreme edges of the line. This is equivalent to assuming that the background varies linearly across the line. The intensity profile so obtained has a symmetrical central region, but in general the two wings are slightly different. This is because of small errors in the determination of the background gradient due to the presence of the wings of the line being studied, and occasionally the wing of an adjacent line. A symmetrical line is obtained by adjusting the values of the log i_B to correspond with a slightly different background gradient. Provided there is no great error in the first estimate of the background gradient, it is sufficiently accurate to use the line profile derived from this by taking half the width of the curve at a given intensity as the abcissa corresponding with that intensity. The corrected curve $I(x)$ is normalized by adjusting the intensity scale so that the maximum intensity is unity.

The theoretical profile of any line will be a function $I(\Delta)$ of a variable $\Delta = Qx$, where Q is a constant containing a number of parameters such as electron wavelength, size of crystals, magnitude of random stresses, etc. Different types of line broadening will be expressed by different functions $I(\Delta)$ and by different expressions for Q in terms of the parameters. In order to test whether an experimental line profile $I(x)$ is identical with a theoretical profile $I(\Delta)$, values of x and Δ corresponding to the same intensity are read from the experimental and theoretical curves, and a graph is drawn of $Q = \Delta/x$ against I. If this is a horizontal straight line, the experimental profile is the same as the theoretical one.

§ 3. THEORY OF LINE PROFILES

Before discussing the experimental measurements of line profiles, it is convenient to derive the theoretical profiles $I(\Delta)$ for different types of broadening.

3.1. *Particle Size Broadening*

The line profile of a powder pattern due to particle size broadening can be shown (Bertaut 1950) to depend on a function $p(n)/N$ where N is the total number of atoms in all the crystals of the specimen irradiated by the beam and $p(n)$ is the total number of rows of atoms of length na, measured perpendicular to the reflecting planes, in all crystals of the specimen; a is the spacing of these planes. The line profile thus depends on an *average* shape and size defined by p/N as a function of n. In this average shape, irregularities of individual crystals will be smoothed out. Unless all the crystals have nearly the same shape, the average shape will be a highly symmetrical geometrical solid. The most probable profiles for diffraction rings produced by an assembly of irregular crystals will therefore be either (a) a profile formed by diffraction by spherical crystals or (b) a profile formed by diffraction by cylindrical crystals with axes perpendicular to the plane of the specimen.

Profiles of type (a) will occur if the thickness of the crystals is roughly the same in all directions. Profiles of type (b) will occur if the crystals have very different dimensions in and perpendicular to the plane of the specimen. Halliday *et al.* (1954) for example, have suggested that specimens of vacuum evaporated lithium fluoride consist of cylindrical crystals, the axes of which are perpendicular to the plane of the specimen; the length of the cylinders is large compared with their diameter.

An expression for the profiles in case (*a*) has been given by Patterson (1939 b). In the notation of the present paper this can be written

$$I_p' = \Delta^{-4}[\sin^2\Delta - 2\Delta\sin\Delta\cos\Delta + \Delta^2] \quad . \quad . \quad . \quad . \quad (1)$$

where

$$\Delta = 2\pi\left(\frac{R_0}{a}\right)\left(\frac{x}{t}\right)$$

or

$$Q_p = \frac{\Delta}{x} = 2\pi R_0/\lambda L. \quad . \quad . \quad . \quad . \quad . \quad . \quad . \quad . \quad . \quad . \quad (2)$$

R_0 is the radius of the crystals, λ the electron wavelength, L the specimen-to-plate distance, x distance measured on the photographic plate and t the distance between successive orders of diffraction from the same crystal planes.

The profiles of diffraction lines of type (*b*) when the axes of the cylinders are parallel to the incident electron beam, can be calculated in the usual way by making use of the function given by Patterson (1939 a) for the distribution of intensity round reciprocal lattice points in the case of cylindrical crystals. The expression so obtained for the line profile is

$$I_p = \frac{3\pi}{2}\frac{S_1(2\Delta)}{(2\Delta)^2} \quad . \quad . \quad . \quad . \quad . \quad . \quad . \quad (3)$$

where S_1 is the first-order Struve function tabulated by Jahnke and Emde (1954) and Δ/x is given by (2).

A distinguishing feature of particle-size broadening is that the breadth of the line is independent of the order of the diffraction. This does not mean that all the rings of the diffraction pattern will have exactly the same width, for crystals oriented to reflect into different diffraction rings may be of different sizes. It does mean, however, that there will be no general tendency for the breadth to vary with the radius of the diffraction rings.

3.2. *Strain Broadening*

If the crystals in a specimen exert forces on one another, they will be elastically deformed and will therefore have different lattice constants, resulting in a broadening of the diffraction rings. If δ is the fractional change of the spacing of the reflecting plane, the displacement of the diffraction ring is given by

$$x = t\delta. \quad . \quad . \quad . \quad . \quad . \quad . \quad . \quad . \quad . \quad (4)$$

In this equation, t is the radius of the diffraction ring. δ will be proportional to the stress acting on the crystal, and will also depend on the directions of the axes of the stress tensor. It has not been possible to calculate the distribution of δ, and therefore the profile of the diffraction line, for stresses which are random in direction and have a Gaussian distribution of magnitude. It would be expected that the resulting line profile would not be Gaussian. In fact, experimental line profiles are often quite closely Gaussian; in interpreting the particular profiles studied in the present paper, it has been found unnecessary to assume anything but a Gaussian profile for strain-broadened lines. We therefore, following Stokes and Wilson (1944), assume the distribution of δ to be Gaussian.

$$\text{Probability of strain } \delta - \delta + d\delta \propto \exp\left(\frac{\delta^2}{2\overline{\delta^2}}\right) d\delta. \qquad (5)$$

The variance $\overline{\delta^2}$ of δ can be calculated for any assumed system of stresses. Let the stress tensor acting on any crystal of the specimen have components $\sigma_1\ \sigma_2\ \sigma_3$ when referred to its principal axes. Since the stresses have a random distribution, we may write

$$\overline{\sigma_1{}^2} = \overline{\sigma_2{}^2} = \overline{\sigma_3{}^2} = A,$$

$$\overline{\sigma_1\sigma_2} = \overline{\sigma_2\sigma_3} = \overline{\sigma_3\sigma_1} = B.$$

Stokes and Wilson have given an expression for $\overline{\delta^2}$ when the axes of the stress tensor are oriented at random. In the notation of the present paper, this may be written

$$\overline{\delta^2} = \frac{A}{5}\,[3s_{11}{}^2 + 4s_{11}s_{12} + 8s_{12}{}^2 - 4\{(s_{11}-s_{12})^2 - 4s_{44}{}^2\}\alpha]$$
$$+ \frac{B}{5}\,[2s_{11}{}^2 + 16s_{11}s_{12} + 12s_{12}{}^2 + 4\{(s_{11}-s_{12})^2 - 4s_{44}{}^2\}\alpha]. \qquad (6)$$

$s_{11}\, s_{12}\, s_{44}$ are the elastic moduli and $x = \sum h^2k^2$ where hkl are the direction cosines of the normal to the reflecting planes. The variation of $\overline{\delta^2}$ with $[hkl]$ is determined by the ratio B/A. If there is no correlation between the components $\sigma_1\ \sigma_1\ \sigma_3$ of the stress tensor, $B=0$. We refer to this as Model I. The other extreme (Model II) is where there is complete correlation and $B=A$. The expression for $\overline{\delta^2}$ then takes the simple form $A(s_{11}+2s_{12})^2$ and is independent of hkl.

The specimens used in electron diffraction studies are in the form of thin films perpendicular to the electron beam. It is then reasonable to assume that the stress tensor acting on any crystallite has two axes (components $\sigma_1\ \sigma_2$) lying in the plane of the film, which also contains the direction $[hkl]$, and $\sigma_3=0$. This assumption leads to the expression

$$\overline{\delta^2} = A[\tfrac{1}{4}(3s_{11}{}^2 + 2s_{11}s_{12} + 3s_{12}{}^2) - (s_{11}-s_{12}-2s_{44})(2s_{11}+s_{44})\alpha$$
$$+ \tfrac{3}{8}(s_{11}-s_{12}-2s_{44})^2(3\alpha^2+\beta)]$$
$$+ B[\tfrac{1}{4}(s_{11}{}^2 + 6s_{11}s_{12} + s_{12}{}^2) - (s_{11}-s_{12}-2s_{44})(2s_{12}-s_{44})\alpha$$
$$+ \tfrac{3}{8}(s_{11}-s_{12}-2s_{44})^2(\alpha^2-5\beta)] \qquad (7)$$

where $\beta = h^2k^2l^2$; $A = \overline{\sigma_1{}^2} = \overline{\sigma_2{}^2}$; $B = \overline{\sigma_1\sigma_2}$. As with eqn. (6), we may consider the extreme cases of $B=0$ (Model III) and $B=A$ (Model IV).

Stokes and Wilson have proposed another model (Model V) according to which $\overline{\delta^2}$ is inversely proportional to the square of Young's modulus in the direction $[hkl]$. This may be written

$$\overline{\delta^2} \propto [s_{11} - 2(s_{11}-s_{12}-2s_{44})\alpha]^2. \qquad (8)$$

For an elastically isotropic material, $s_{11}-s_{12}=2s_{44}$ and for every model $\overline{\delta^2}$ becomes constant and independent of *hkl*. The ratios of the breadths of the different lines are then independent of the model and only their absolute value is in doubt. Substitution of the elastic moduli of LiF or Au in equs. (6)–(8) shows that the same is substantially true for these substances. For LiF the *maximum* difference between the relative $\overline{\delta^2}$ values† calculated for any model and the mean of the values for all 5 models is: 16% (ring 111); 16% (ring 200); 5% (ring 220); 4% (ring 311). Now it is shown in §4 that for the 111 ring the contribution of strain broadening to the total width is negligible. The contribution in the case of the 200 ring is perceptible, but not enough to detect a 16% variation. The widths of the outer rings have a large strain contribution, but for these the differences between the models become small. Gold is less nearly isotropic than LiF, and the maximum difference between the relative $\overline{\delta^2}$ values for any model and the mean of all models is: 48% (111); 32% (200); 7% (220); 12% (311).

We conclude that the goodness of fit of the theoretical and experimental line profiles is substantially independent of the model chosen. In the present paper, we have interpreted our results in terms of Model IV. The values obtained for the r.m.s. stress may be too high by a factor of not more than 1·4 in the case of LiF or not more than 4·2 in the case of Au. For this model, the line profile is

$$I_s=\exp(-\Delta^2)=\exp[-(Qx)^2] \qquad \ldots\ldots \quad (9)$$

where

$$(1/Q_s)^2=2At^2[(s_{11}+s_{12})^2-2(s_{11}-s_{12}-2s_{44})(s_{11}+s_{12})\alpha \\ +\tfrac{3}{2}(s_{11}-s_{12}-2s_{44})^2(\alpha^2-\beta)]. \qquad \ldots\ldots \quad (10)$$

3.3. *Refraction Broadening*

The effects of refraction due to the inner potential of the crystals and of dynamical interference may conveniently be considered together. Let V be the potential used to accelerate the electrons and let the electrostatic potential ϕ in the crystal be expressed as a Fourier series

$$\phi=\phi_0+\sum\phi_{hkl}\cos 2\pi\left\{\frac{lx+my+nz}{a_{hkl}}+\chi_{hkl}\right\} \qquad \ldots \quad (11)$$

where xyz are the coordinates of a point in the crystal, lmn are the direction cosines of the normal to the atom planes of indices hkl and spacing a_{hkl} and χ_{hkl} is a phase factor. Then the diffracted spot on the photographic plate is displaced in a direction perpendicular to the refracting edge of the crystal by amounts

$$\pm L[(\phi_0/2V)(\tan\beta-\tan\beta')+\mu\sin\theta(\tan\beta+\tan\beta') \\ \pm\{\mu^2\sin^2\theta+(\phi_{hkl}/2V)^2\}^{1/2}(\tan\beta-\tan\beta')] \qquad \ldots\ldots \quad (12)$$

---

† By the relative value of $\overline{\delta^2}$ is meant its value for the ring in question ÷ by the geometric mean for all rings.

(Rymer 1953). The first term is due to ordinary refraction due to the inner potential ϕ_0. β and β' are the angles made by the rays with the normals to the faces where the rays enter and leave the crystal. θ is the Bragg angle and μ the angle by which the incident ray deviates from the direction satisfying the Bragg relation. V is the potential used to accelerate the electrons. The effect of dynamical interference is represented by the last two terms: it results in each of the two spots which could arise on the kinematical theory being split into two components. The intensities of these components are equal and proportional to

$$\frac{1}{1+(2\mu V\sin\theta/\phi_{hkl})^2} . \qquad \qquad (13)$$

By applying (12) and (13) to a specimen consisting of crystals with faces in all orientations, it is, in principle, possible to calculate the profile of the diffraction line. In practice, the mathematical expressions become very complicated even for the apparently simple model of a specimen consisting of spherical crystals. It is, however, evident that the breadth of a line will be a monotonically increasing function of both ϕ_0/V and ϕ_{hkl}/V. It is therefore possible to make the following general statements.

(i) ϕ_{hkl} is a monotonically decreasing function of interplanar spacing. The effect of dynamical interference is therefore most marked for the innermost rings and rapidly diminishes for the outer rings.

(ii) 'Kinematical' refraction, represented by the first term of (12) broadens the central undiffracted spot of the pattern as well as the rings. Other sources of broadening have negligible or no effect on the central spot.

(iii) Specimens of low atomic weight, and therefore small ϕ_0, ϕ_{hkl}, will show only small broadening.

In some examples studied in the present paper, there is reason to believe that refraction is a major cause of line broadening: nevertheless, the central spot shows no broadening. It is concluded that the first term of (12) is zero, i.e. $\tan\beta=\tan\beta'$. This means that we are dealing with refraction by parallel-sided slabs, which we may assume to be bounded by planes (HKL). It is not necessary that these slabs should be separate crystals: defects could split up a large crystal into parallel-sided domains each of which scatter electrons coherently but out of phase with other domains. For a crystal oriented so that the angle of incidence is β, eqns. (12) and (13) give for the deviation of the spot on the photographic plate

$$s=2LM\tan\beta \qquad \qquad (14)$$

and for the intensity

$$J=\frac{1}{1+M/\Phi^2} \qquad \qquad (15)$$

where

$$M=\mu\sin\theta \quad \text{and} \quad \Phi=\phi_{hkl}/2V. \qquad \qquad (16)$$

Let Ox (fig. 1) be the normal to the reflecting plane and zO the incident electron beam. Ox is parallel to the radius of the diffraction pattern through the diffracted spot if refraction be ignored. Let the normal OP to the slab be inclined at an angle ρ to Ox and in azimuth σ about it. Then

$$\cos\beta=\sin\rho\cos\sigma \quad . \quad . \quad . \quad . \quad . \quad . \quad . \quad (17)$$

and the plane of incidence intersects the xOy plane at an angle ω to Ox such that

$$\tan\omega=\tan\rho\sin\sigma. \quad . \quad . \quad . \quad . \quad . \quad . \quad . \quad (18)$$

If x be the radial component of the displacement s of the spot on the photographic plate

$$x=s\cos\omega. \quad . \quad . \quad . \quad . \quad . \quad . \quad . \quad . \quad (19)$$

Eliminating M, s, β, from eqns. (14), (15), (17), (18), (19)

$$J=1/[1+(x^2/4L^2\Phi^2)\tan^2\rho\cos^2\sigma]. \quad . \quad . \quad . \quad . \quad (20)$$

Fig. 1

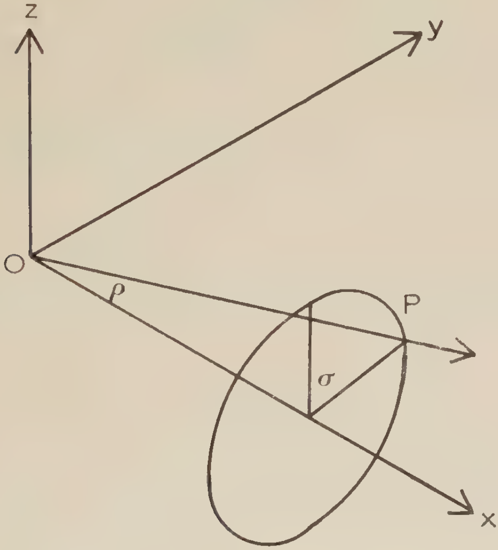

The intensity diffracted into this spot will be proportional to the area of the incident beam intercepted by the slab. This area is proportional to $\cos\beta$. We therefore take as the intensity of the spot formed by a crystal slab with azimuth σ to $\sigma+d\sigma$

$$J'=\frac{\sin\rho\cos\sigma\,d\sigma}{1+(x^2/4L^2\Phi^2)\tan^2\rho\cos^2\sigma}. \quad . \quad . \quad . \quad . \quad (21)$$

The total intensity at a point distance x from the centre of the line is obtained by integrating this expression over all values of the azimuth angle σ. This leads to the expression

$$I_r=\frac{\sinh^{-1}\Delta}{\Delta\sqrt{(1+\Delta^2)}} \quad . \quad . \quad . \quad . \quad . \quad . \quad . \quad (22)$$

for the line profile, where

$$\frac{\Delta}{x}=Q=\tan\rho/2L\Phi=V\tan\rho/L\phi_{hkl} \quad . \quad . \quad . \quad . \quad (23)$$

and the expression has been normalized so that $I(0)=1$. ρ is the angle between the planes HKL bounding the crystal slab and the reflecting planes *hkl*. Thus

$$\cos\rho=(Hh+Kk+Ll)/(\sum h^2\sum H^2)^{1/2}. \quad . \quad . \quad . \quad (24)$$

The width of the line is proportional to

$$\frac{\phi_{hkl}L}{V\tan\rho}. \quad . \quad . \quad . \quad . \quad . \quad . \quad . \quad . \quad . \quad (25)$$

3.4. *Combined Broadening*

It will often happen that the breadth of a line is due partly to particle size and partly to strain broadening. In this case, the resultant profile is the fold of the particle-size function

$$I_p(\Delta)=I_p(Q_px)$$

with the strain function

$$\exp(-\Delta^2)=\exp[-(Q_sx)^2]$$

Q_p and Q_s are the values of Q given by eqns. (2) and (10) respectively. Thus

$$I\propto\int_{-\infty}^{+\infty}I_p(\Delta-\zeta)\exp\left[-\left(\frac{\zeta Q_s}{Q_p}\right)^2\right]d\zeta. \quad . \quad . \quad . \quad . \quad (26)$$

Analogous expressions can be derived for other combinations of broadening. The integral of (26) must be evaluated numerically for any given value of Q_p/Q_s.

§ 4. EXPERIMENTAL RESULTS : LITHIUM FLUORIDE

Because of the low atomic numbers of both lithium and fluorine, the potential coefficients of lithium fluoride are expected to be low (probably less than 5 v). Refraction and dynamic refraction should therefore be negligible and we can confine our attention to particle size and stress broadening.

Figures 2 (*a*, *b*) shows the result of fitting the particle-size broadening functions I_p' and I_p of eqns. (1) and (3) to the 111 diffraction ring profile of lithium fluoride. It is clear that the function representing broadening by cylindrical particles is a better fit than that representing broadening by spherical particles. For comparison, fig. 2 (*c*) shows a Gaussian function I_s (strain broadening) fitted to the same data. It is clear that I_p and I_s are almost indistinguishable. For a reason which will become apparent later, we conclude that the width of the 111 ring is mainly due to particle-size broadening by cylindrical crystals. From fig. 2 (*b*)

$$Q=\frac{2\pi R_0}{\lambda L}=205\ \mathrm{cm}^{-1}.$$

Fig. 2

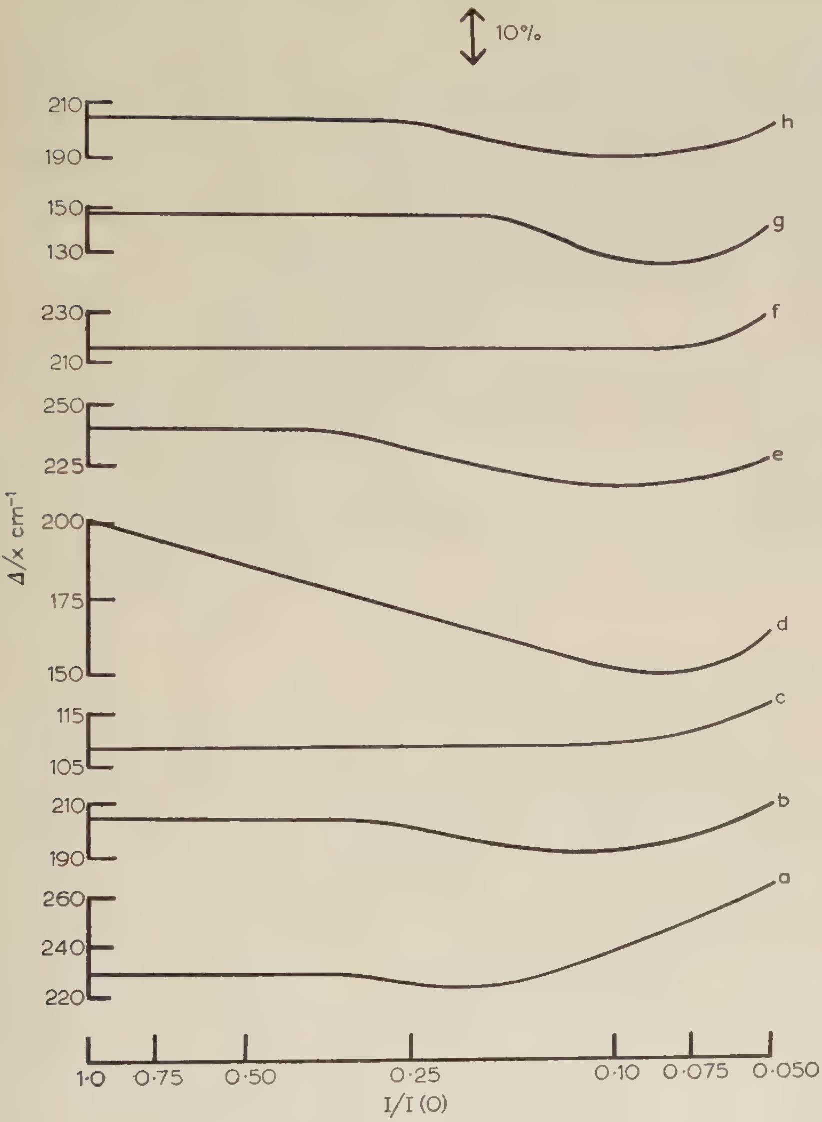

Lithium Fluoride. Comparison of experimental line profiles $I(x)$ with theoretical profiles $I(\Delta)$. The ratio Δ/x for a given I is plotted against I. The ordinate scales are chosen so that for each curve a given percentage change of Δ/x corresponds to the same vertical distance.

(*a*) I'_p—111 ring	(*e*) I_4—311 ring
(*b*) I_p —111 ring	(*f*) I_1—111 ring
(*c*) I_s —111 ring	(*g*) I_2—200 ring
(*d*) I_p —311 ring	(*h*) I_3—220 ring

For this plate, $\lambda L = 2{\cdot}08 \times 10^{-8}\,\text{cm}^2$, and therefore the radius of the cylindrical crystals is

$$R_0 = 68\ \text{Å}.$$

Figure 2 (*d*) shows the result of fitting I_p to the profile of the 311 diffraction ring on the same plate. There is a great difference between the experimental profile and the theoretical curve I_p. Since I_p and I_s are almost indistinguishable, there will be a similar difference between the experimental profile and I_s. On the other hand, fig. 2 (*e*) shows that there is excellent agreement between the experimental profile and a function

$$I_4 = C\int_{-\infty}^{+\infty} I_p(\Delta - \zeta)\exp\left(-\zeta^2/2{\cdot}5\right)d\zeta$$

which is the fold of I_p with a Gaussian function $I_s = \exp\left(-\Delta^2/2{\cdot}5\right)$. C is a normalizing factor to make the maximum of the integral unity. The fact that the width of the innermost ring arises from particle-size broadening alone and that of the outermost ring from a combination of particle-size and strain broadening is to be expected, since particle-size breadths are roughly independent of the diffraction ring radius but breadths due to strain are roughly proportional to the ring radius.

From fig. 2 (*e*),

$$\frac{\Delta}{x} = Q_p = 240\ \text{cm}^{-1}. \qquad \ldots\ldots\ldots \qquad (27)$$

Hence from (2) and the value of λL quoted above,

$$R_0 = 79\ \text{Å}.$$

Now $(Q_p/Q_s)^2 = 2{\cdot}5$. Hence substituting the values (Rao 1949) $s_{11} = 1{\cdot}17 \times 10^{-12}$, $s_{12} = -0{\cdot}364 \times 10^{-12}$, $s_{44} = 0{\cdot}468 \times 10^{-12}$ of the elastic constants and the radius $l = 1{\cdot}715$ cm of the 311 diffraction ring into (10) and making use of (27) we obtain for the r.m.s. stress $A^{1/2}$

$$A^{1/2} = 3{\cdot}8 \times 10^9\ \text{dyn/cm}^2.$$

The values of Q_p/Q_s for other rings of the diffraction pattern can be calculated from (2) and (10) using the above values of R_0 and $A^{1/2}$. It will be found that the profiles I_1, I_2, I_3 of the 111, 200 and 220 rings are the folds of $I_p(\Delta)$ with $\exp\left(-\Delta^2/0{\cdot}50\right)$, $\exp\left(-\Delta^2/1{\cdot}17\right)$ and $\exp\left(-\Delta^2/1{\cdot}59\right)$ respectively. Figures 2 (*f*, *g*, *h*) shows that there is fair to good agreement in all cases between the theoretical and experimental profiles of the different rings on the same plate. From figs. 2 (*f*, *g*, *h*) the values of R_0 and $A^{1/2}$ given in table 1 have been derived. Except for the 200 ring, there is good agreement between measurements on the different diffraction rings. The low value of R_0 and the high value of $A^{1/2}$ derived from the 200 ring suggest that there is some other, unexplained, source of broadening which affects this ring and not the others.

We conclude that our results are consistent with the assumption that the 'average shape' of the crystals is a cylinder of diameter $2R_0 = 144$ Å with axis perpendicular to the plane of the specimen and with random stresses, having a r.m.s. value $A^{1/2} = 4{\cdot}1 \times 10^9$ dyn/cm², acting in the plane of the specimen. In addition, there is an unexplained source of broadening which affects the 200 ring only.

Table 1. Radius R_0 of Cylindrical Crystals and r.m.s. Stress $A^{1/2}$ in the Plane of the Specimen, derived from Measurement of the Profile of Different Diffraction Rings

Ring indices	R (Å)	$10^{-9} A^{1/2}$ (dyn/cm²)
111	71	4·2
200	49	6·2
220	67	4·4
311	79	3·8

§ 5. Experimental Results : Gold

The potential coefficients of gold are relatively large owing to the high atomic number. Dynamical refraction may therefore make an appreciable contribution to the width of the diffraction rings. The potential coefficient ϕ_{hkl} is given by

$$\phi_{hkl} = \frac{a_{hkl}^2}{\pi} eN(Z-f) \exp(-B/4a^2_{hkl}) \quad . \quad . \quad . \quad . \quad (28)$$

where a_{hkl} is the spacing of the *hkl* planes, N the number of atoms per unit volume of atomic number Z and X-ray scattering factor f and e is the electronic charge. The last factor is the Debye–Waller temperature factor; for gold, with a Debye temperature of 180°K, the constant B has the value of 3·6 Å². Taking the lattice constant of gold to be 4·07 Å, and using the f values given in the *Internationale Tabellen zur Bestimmung von Kristallstrukturen* we obtain the following values for some important potential coefficients

$$\phi_{111} = 19{\cdot}2, \quad \phi_{220} = 9{\cdot}2, \quad \phi_{311} = 6{\cdot}8 \text{ v}.$$

From 25, the breadth of a diffraction ring due to dynamical refraction is $\sim \phi_{hkl} L/V$. Writing $L = 50$ cm and $V = 78$ kv, we find that the width of the 111 ring due to dynamical refraction should be $\sim 120\,\mu$. In fact, the width of this ring, measured where the intensity is 50% of the maximum, was found to be $280\,\mu$.

It is clear from these calculations that refraction will play a dominant rôle in determining the profiles of, at any rate, the innermost diffraction rings of gold. Nevertheless, the central undiffracted spot shows negligible broadening. According to the theory of § 3, it therefore appears that we have to deal with dynamical refraction by parallel-sided slabs of crystal, and that the intensity profile is given by eqn. (22). Figure 3 (*a*) shows this equation tested against the experimental profile of the 111

Fig. 3

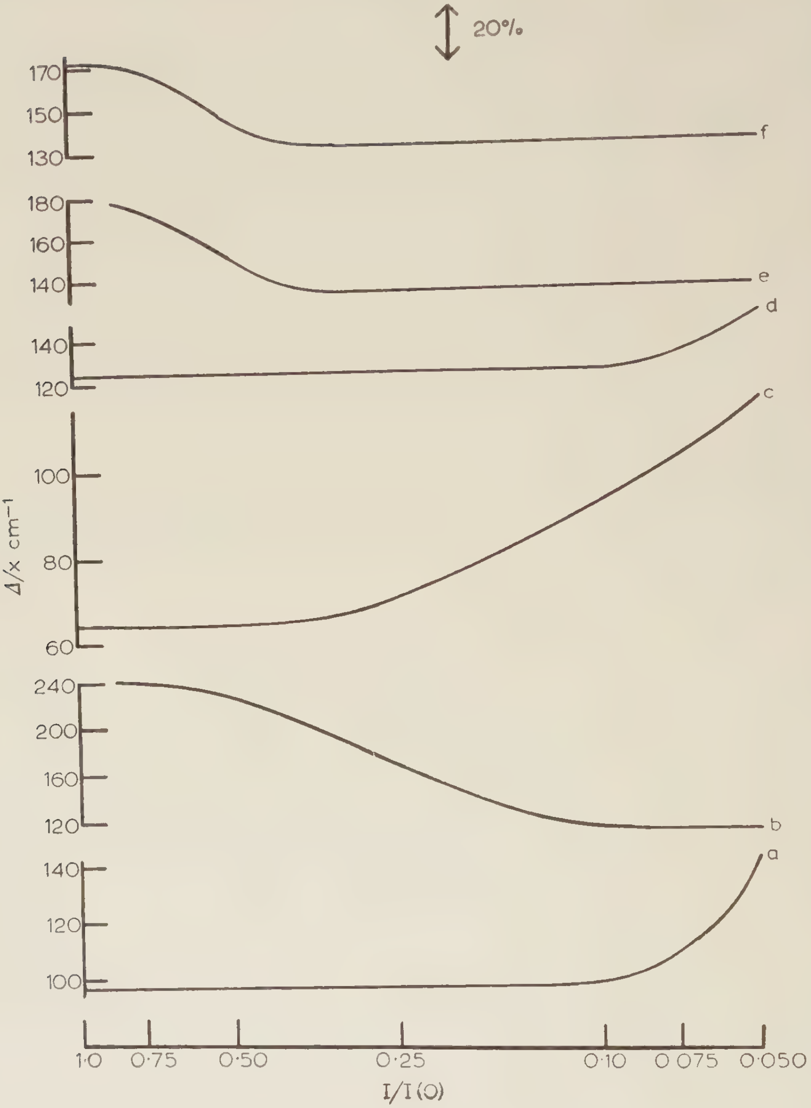

Gold. Comparison of experimental line profiles $I(x)$ with theoretical profiles $I(\Delta)$. The ratio Δ/x for a given I is plotted against I. The ordinate scales are chosen so that for each curve a given percentage change of Δ/x corresponds to the same vertical distance.

(*a*) I_r—111 ring
(*b*) I_p—111 ring
(*c*) I_r—220 ring
(*d*) I_1—111 ring
(*e*) I_2—220 ring
(*f*) I_3—311 ring

ring of gold. For comparison, fig. 3 (*b*) shows the same experimental data tested against the particle-size function I_p. It is clear that the function I_r fits the data much better than I_p or I_s (it will be remembered that I_p and I_s are almost indistinguishable).

From fig. 3 (*a*)

$$\Delta/x = 98\ \mathrm{cm}^{-1}$$

and therefore from (23), using the values of ϕ_{111}, L and V quoted in the last paragraph $\rho = 50°$. Now the angle between the [111] and [100] directions is 54°. This suggests that dynamical refraction is occurring at parallel-sided crystal slabs bounded by 100 planes.

Figure 3 (*c*) shows that the profile of the 220 diffraction ring of the same material does not fit the dynamical refraction function. This might indicate that the breadth of the rings is due partly to dynamical refraction and partly to strains. Since dynamical refraction broadening diminishes, and strain broadening increases, with ring radius, we should expect the innermost ring to have a contour determined mainly by refraction and the outer rings to show evidence of strain broadening. We will examine this hypothesis in more detail.

If it be assumed that dynamical refraction is occurring at parallel-sided slabs of crystal bounded by (100) faces, then from 25 and the values of the potential coefficients quoted above, the relative widths of the various rings due to this cause are as given in the second row of table 2. The contribution to the widths due to strain can be found by substituting in eqn. (10) the values (Boas and Mackenzie 1950) of the elastic constants of gold

$$s_{11} = 2{\cdot}37 \times 10^{-12}, \quad s_{12} = -1{\cdot}083 \times 10^{-12}, \quad s_{44} = 0{\cdot}595 \times 10^{-12}.$$

Table 2

hkl	111	202 220	022	311	113 131
Width $\phi_{hkl} \cot \rho$ due to refraction	13·6	9·2	0	14·4	2·2
Relative widths due to strains	4·8	12·2	12·2	16·3	16·3
Relative weights of equivalent reflections	1	$\sqrt{2}$	1	1	$\sqrt{20}$

These widths are listed in the third row of table 2. The intensity of a ring is proportional to the multiplicity of the reflecting plane and also to the area of the incident electron beam which is intercepted; the latter quantity is proportional to $\sin \rho$. The relative weights of the different reflections are therefore as given in the fourth row of table 2.

Suppose now that the magnitude of the strains is such that the contours of the 220 and 202 rings can be represented by the fold of I_r with $\exp(-\Delta^2/p)$.

The contour of the 022 ring is due entirely to strain and is therefore $\exp(-\Delta^2/p)$. The contour of the multiplet 220, 202, 022 is therefore

$$I_2^* = \frac{1}{1+\sqrt{2}}\left[\sqrt{2}\int_{-\infty}^{+\infty} CI_r(\Delta-\zeta)\exp(-\zeta^2/p)\,d\zeta + \exp(-\Delta^2/p)\right] \quad . \quad . \quad . \quad (29)$$

where C is a normalizing factor to make the maximum of the integral unity. From the ratios of ring widths given in table 2 it then follows that the contour of the 111 ring is the fold of I_r with $\exp(-\Delta^2/0{\cdot}1p)$:

$$I_1^* = \int_{-\infty}^{+\infty} CI_r(\Delta-\zeta)\exp(-\zeta^2/0{\cdot}1p)\,d\zeta. \quad . \quad . \quad . \quad (30)$$

The contour of the 311 ring will then be the fold of I_r with $\exp(-\Delta^2/0{\cdot}7p)$. The 113 and 131 rings will show negligible refraction broadening and will therefore have a contour $\exp(-\Delta^2/0{\cdot}7p)$. The resultant contour of the 311, 131, 113, multiplet is therefore

$$I_3^* = \frac{1}{1+\sqrt{20}} \times \left[\int_{-\infty}^{+\infty} CI_r(\Delta-\zeta)\exp(-\zeta^2/0{\cdot}7p)\,d\zeta + \sqrt{20}\exp(-\Delta^2/0{\cdot}7p)\right]. \quad (31)$$

Figures 3 (*d*, *e*, *f*) show that there is good agreement between the experimental contours of the 111, 220 and 311 multiplets and the functions I_1^*, I_2^*, and I_3^* respectively if we choose $p=10$. From the values of Δ/x in these figures, the potential coefficients are found to be

$$\phi_{111}=17{\cdot}8, \quad \phi_{220}=11{\cdot}0, \quad \phi_{311}=5{\cdot}6\text{ v}.$$

These may be compared with the calculated values quoted previously:

$$\phi_{111}=19{\cdot}2, \quad \phi_{220}=9{\cdot}2, \quad \phi_{311}=6{\cdot}8\text{ V}.$$

Figures 2 (*d*, *e*, *f*) also enable $A^{1/2}$, the r.m.s. stress in the plane of the specimen, to be calculated. The values obtained from the three diffraction rings measured are

(111) $1{\cdot}00\times10^{10}$; (220) $1{\cdot}28\times10^{10}$; (311) $0{\cdot}87\times10^{10}$ dyn/cm^2.

The agreement of the potential coefficients with the calculated values, and the agreement between the values of the stress derived from different diffraction rings, can both be regarded as satisfactory when it is borne in mind that there is only one disposable constant (p) in the expressions for I_1^*, I_2^* and I_3^*.

The contour of the 200 ring is broad and irregular; it cannot be fitted to the functions studied. This tends to confirm that refraction is occurring at (100) faces. The beam reflected off a 200 plane would meet a (100) face at grazing incidence and would suffer a large radial deviation; but no radial deviation would occur by refraction at (010) or (001) faces. The contour will therefore consist of a narrow central portion with extensive 'wings', the whole being subject to strain broadening. The precise form of the contour is rather sensitive to the exact details of the model used, and it does not appear profitable to examine it further.

§ 6. CONCLUSIONS

The interest of the present study lies not so much in the actual results, which apply only to the particular specimens studied, but in the demonstration of the procedure to be followed in distinguishing between different types of line broadening. It appears that line breadths can be correctly interpreted only by a detailed study of the profiles of several diffraction rings of the same pattern. The mere comparison of the widths of the rings can be completely misleading. Thus Rymer (1956) has shown that the *widths* of the rings of a gold specimen similar to that used in the present study were consistent with a particle size interpretation. It appears that stresses usually exist in a specimen as well as other sources of broadening. The present results suggest that the profile of the innermost ring will often give a fairly reliable indication of the nature of broadening other than stress broadening, because this ring is affected least by stress broadening and most by other types of broadening. The stress may then be estimated from the profile of the outermost rings where the reverse applies.

ACKNOWLEDGMENTS

The authors' thanks are due to Professor R. W. Ditchburn for the provision of facilities and his interest in the work. One author (F.J.F.) is indebted to the Research Board of the University of Reading for a Research Scholarship.

REFERENCES

BERTAUT, E. F., 1950, *Acta cryst.*, **3**, 14.
BOAS, W., and MACKENZIE, J. K., 1950, *Progr. Metal Phys.*, **2**, 90.
BRADLEY, D. E., 1954, *Brit. J. appl. Phys.*, **5**, 65.
BUTLER, C. C., 1945, *Ph.D. Thesis*, Reading University.
COWLEY, J. M., and REES, A. L. G., 1953, *J. Sci. Instrum.*, **30**, 33,
EHLERS, H., 1956, *Z. Naturf.*, **11a**, 359.
HAINE, M. E., and EINSTEIN, P. A., 1952, *Brit. J. appl. Phys.*, **3**, 40.
HALLIDAY, J. S., RYMER, T. B., and WRIGHT, K. H. R., 1954, *Proc. roy. Soc.* A, **225**, 548.
JAHNKE, E., and EMDE, F., 1954, *Tables of Functions* (New York: Dover Publications).
PATTERSON, A. L., 1939 a, *Phys. Rev.*, **56**, 972; 1939 b, *Ibid.*, **56**, 978.
RAO, T. S., 1949, *Curr. Sci.*, **18**, 436.
RYMER, T. B., 1953, *Brit. J. appl. Phys.*, **4**, 297; 1956, *Proc. roy. Soc.* A, **235**, 274.
RYMER, T. B., and BUTLER, C. C., 1945, *Phil. Mag.*, **36**, 821.
STOKES, A. R., and WILSON, A. J. C., 1944, *Proc. phys. Soc. Lond.*, **56**, 174.
TOMLIN, D. H., and FAYERS, F. J., 1955, *J. Sci. Instrum.*, 32, 404.

The Effect of Atmospheric Corrosion on Metal Fatigue†

By N. J. Wadsworth and J. Hutchings
Royal Aircraft Establishment, Farnborough, Hants.

[Received June 26, 1958]

Abstract

Polycrystalline specimens of copper, aluminium and gold were fatigued in reversed bend in various pressures of air and in water vapour and inert gases. The ratio of life in atmosphere of air to that in vacuum ($\sim 10^{-5}$ mm Hg) at lives of about 10^6 cycles was 1 : 20 for copper, 1 : 5 for aluminium and about 1 : 1 for gold.

Some specimens were examined at intervals during the test. Small cracks a few microns deep formed in the first few hundredths of the life in air and after the same number of cycles in vacuum. The effect of air was to speed the propagation of cracks in copper and aluminium but not gold.

Electron micrographs showed that extrusions and intrusions can occur close to each other in the same slip band.

§ 1. Introduction

Previous work (Gough and Sopwith 1932, 1935, 1946) has shown that the fatigue life of various metals can be increased by removing the air surrounding the specimen but gave no indication of the mechanism involved or of which part of the fatigue process is affected. Thompson *et al.* (1956) tested polycrystalline copper in air and in 'oxygen free' nitrogen and examined the surface of the specimens at intervals during the tests. They found that if specimens tested in air were electropolished after about 5% of their life some of the slip bands remained clearly visible. These were called 'persistent slip bands' and it was from one of these that the final crack grew. In nitrogen the persistent slip bands occurred after about the same number of cycles as in air but took much longer to spread and to become undoubted cracks. The nature of 'persistent slip bands' was not known, nor was the relative effect of different amounts of oxygen or other gases. This paper describes the results of experiments in which copper, aluminium and gold specimens were fatigued in various pressures of air and of other gases, their lives determined and growth of cracks followed.

§ 2. Apparatus

The apparatus used in these tests was built to enable specimens to be fatigued at a constant, predetermined, strain in vacuum or in any controlled atmosphere at room temperature. In the previous work of Gough and Sopwith (1932, 1935, 1946) and of Thompson *et al.* (1956) the fatigue specimens were exposed to the air after they had been prepared and annealed before testing in an inert atmosphere or vacuum. It was considered desirable to avoid this in an investigation of the effect of various atmospheres so the apparatus was designed to allow the specimen to be annealed in vacuum and then fatigued without intermediate exposure to air. Thompson *et al.* (1956) showed that fatigue cracks always started on the surface even when the stress was macroscopically uniform over the whole volume of the specimen so a uniform stress was not considered essential. Reversed bending was chosen as the stress system which was most easily applied in vacuum without the apparatus constraining the specimen in any way during annealing.

---

† Communicated by the Authors.

Figure 1 shows the fatigue apparatus used. The top end of the specimen, A, was clamped to the lower end of a stainless steel tube, B, which passed through the top of a brass cylinder, C. A piece of iron and a metal vane were attached to the lower end which was otherwise free. The specimen was surrounded by a silica tube, D. The whole system could be evacuated by an oil diffusion pump connected to the apparatus by large diameter glass tubes. A liquid nitrogen trap increased the pumping speed for condensable vapours. 'O'-ring seals were used throughout. Gases could be admitted when required through a tube, E, which released them close to the specimen.

In use the prepared specimen was fixed in position and the apparatus pumped out. A furnace was placed round the silica tube and the specimen was annealed. The furnace was then removed. After about an hour, when the apparatus had cooled, an electromagnet was placed on each side of the flat end of the silica tube. These magnets were fed with alternating current from different phases of the 50 c/s mains. This produced a force on the iron on the bottom of the specimen which varied sinusoidally (for small movements) at 100 c/s. The specimen thickness and the mass on the free end were chosen to make it approximately resonant at the operating frequency. The specimen was shaped to give a constant surface strain over the centre portion on which observations were made. There was inevitably a slight stress concentration at the curves at the ends of the straight sided region but failure occurred in the straight sided part more often than at either end.

The strain in the specimen was determined by observing the movement of the triangular vane attached to the bottom of the specimen. The point at which the amplitude of movement was exactly equal to the width of the vane was easily seen and was independent of any irregularities in the silica which would invalidate direct measurement of the amplitude from outside. The system was calibrated in terms of surface strain on the straight sided part of the specimen by using electrical resistance strain gauges on a dummy specimen under operating conditions. The extremes of the swing of the vane were monitored by two light beams falling on photocells which adjusted the currents through the magnets to keep the amplitude constant and the specimen central. An automatic cut-out stopped the test at a time when the main crack was just becoming visible to the naked eye. At this stage the rate of propagation of the crack was comparatively large and the total length of the test was little affected by the sensitivity setting of the cut out.

Fig. 1

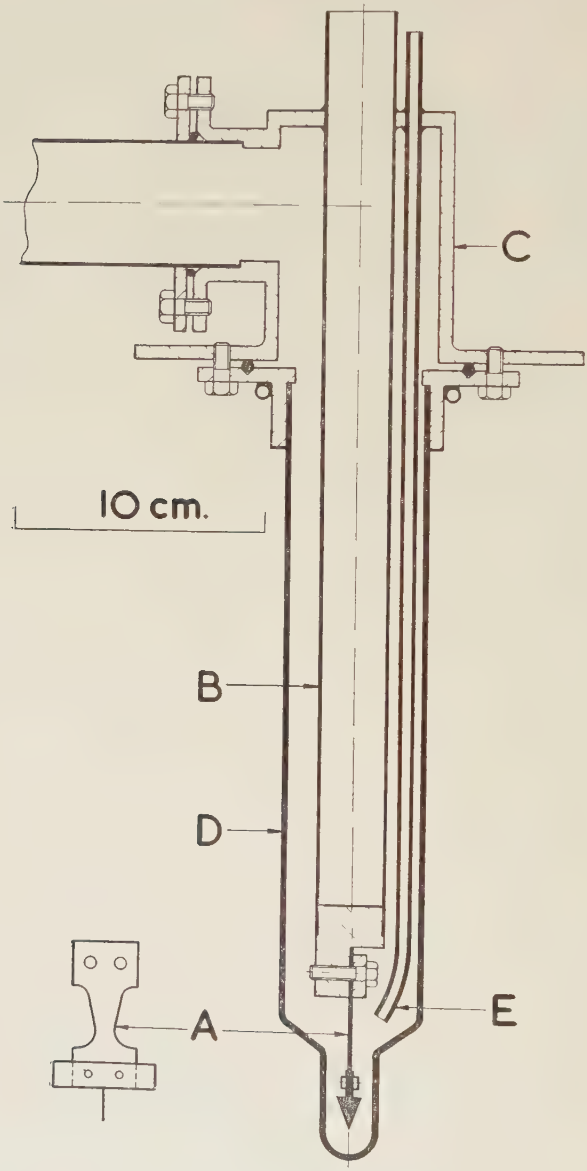

The fatigue apparatus.

If the specimens were soft before the start of the test, as the annealed pure metals were, then it was necessary to increase the fatigue strain gradually. With copper and gold it took about 10^4 cycles to reach full strain while the softer aluminium took about six times as long.

§ 3. MATERIAL

Observations were made on polycrystalline copper, aluminium and gold. The copper used was commercial 'oxygen free high conductivity' copper (99·95%). It was annealed for one hour at 800°C after which the grain size was about 0·5 mm. The aluminium was 'superpure' (99·995%). It was annealed for one hour at 550°C giving a grain size of about 1·5 mm. The gold was 'fine' (99·96%) and was annealed for one hour at 800°C giving a grain size of about 1·25 mm. The copper specimens were 0·85 mm thick while the aluminium and gold were 1·10 mm and 1·06 mm respectively.

The specimens were cut out of sheet of the appropriate thickness, mechanically polished and then electrolytically or chemically polished to give a smooth surface suitable for metallographic examination.

§ 4. RESULTS

4.1. *Effect of Atmosphere on Fatigue Life*

4.1.1. *Copper*

A number of copper specimens, all tested at the same strain, were run to failure in air pressures between one atmosphere and the lowest obtainable—about 7×10^{-6} mm Hg. Intermediate pressures were obtained either by letting air in to the apparatus to the required pressure and then sealing off, or by leaving the pumps on and arranging a deliberate leak. It appeared to make no difference whether the air was stationary or continually changed.

Figure 2 shows the results. The relation between log life and log air pressure is linear over the range investigated and shows no sign of flattening off at either end. In these tests the specimens were fatigued as soon as they had cooled after being annealed and were not exposed to air between annealing and fatiguing. A few other specimens fatigued *in vacuo* were removed from the machine and exposed to air at intervals during the test to enable photographs to be taken of their surface. Their lives were similar to those obtained without exposure to air. A further specimen was deliberately oxidized by admitting air to the vacuum system while the specimen was still hot after being annealed. This produced a visible coat of oxide. The specimen was then fatigued in vacuum and gave a life similar to that of normal specimens fatigued in vacuum. Thus it appears that, as in most corrosion fatigue experiments, it is necessary to have the corrosive medium (air in this case) present at the same time as the fatigue stress to obtain an appreciable reduction in life. The alternate application of corrosion and fatigue does not reduce the life.

Gough and Sopwith (1946) investigated the effect of the various constituents of the atmosphere and concluded that the main reduction in the endurance limit of copper (at 3×10^7 cycles) was produced by the simultaneous presence of oxygen and water vapour. Oxygen alone, or water vapour with nitrogen to make up the pressure, produced little reduction in the endurance limit. Tests were made to find if this was true for the copper used in these experiments. Three specimens were fatigued in dry air at a pressure of about 500 mm Hg. This was obtained by admitting air to the apparatus slowly through a spiral tube filled with glass wool and immersed in liquid nitrogen, the pressure being limited to that at which oxygen started to condense. The lives obtained were significantly greater than those in air but much shorter than those in vacuum and are shown in fig. 3. Two specimens were fatigued in water vapour. The pressure of non-condensable gas (presumably air) present was measured by condensing the water vapour in the liquid nitrogen trap. It was approximately 6×10^{-3} mm Hg for the specimen with a life of

Fig. 2

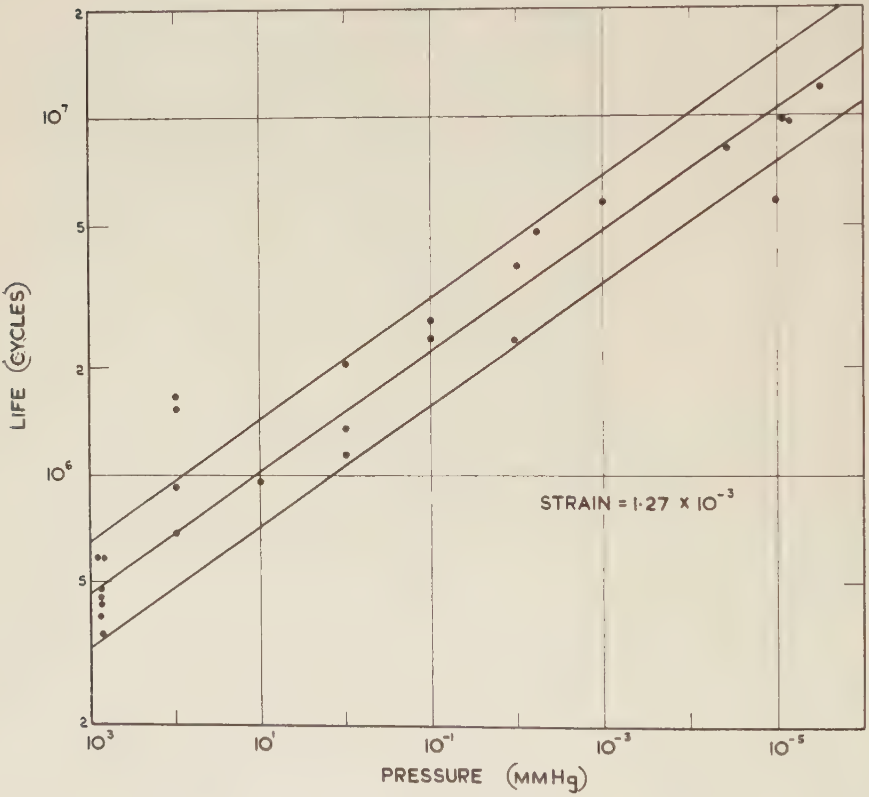

Copper. Variation of fatigue life with air pressure.

$4{\cdot}1 \times 10^6$ cycles and 4×10^{-4} mm Hg for the other. The lives are similar to those which would have been obtained if the water had not been present. Specimens were also fatigued in wet oxygen at one atmosphere pressure and gave lives rather shorter than those of specimens fatigued in air. Specimens fatigued in atmospheres of argon, nitrogen or carbon dioxide had lives compatible with the probable oxygen pressure in these gases. (The nitrogen and argon were stated to contain less than 1 part in 10^5 of oxygen while the carbon dioxide contained "less than 1% oxygen".)

Fig. 3

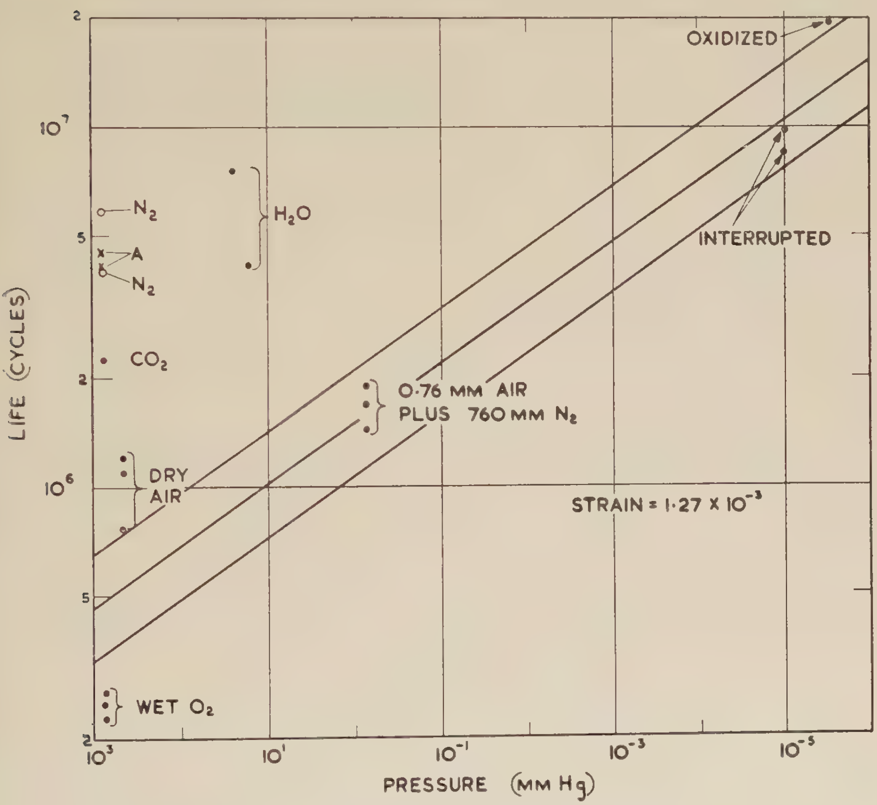

Copper. Fatigue life in various atmospheres.

A check was made on the hypothesis that a certain pressure of oxygen always gave the same life irrespective of the presence of an inert gas. 0·1% of air was added to a cylinder of 'oxygen free' nitrogen and some specimens were fatigued in one atmosphere pressure of the mixture. They had lives similar to those fatigued at a pressure of 10^{-3} atmospheres of air. The points resulting from these various experiments are all shown in fig. 3.

It appears that the fatigue life of this copper at room temperature is affected chiefly by the partial pressure of oxygen, water vapour increasing the effect of the oxygen slightly but having no effect on its own.

Some specimens were fatigued at other strains in air or in vacuum to check that a similar effect occurred at other strains. The results are shown in fig. 4. Over the range studied the ratio of life in vacuum to that in air increases as the stress is reduced, as it does in normal corrosion fatigue tests.

Fig. 4

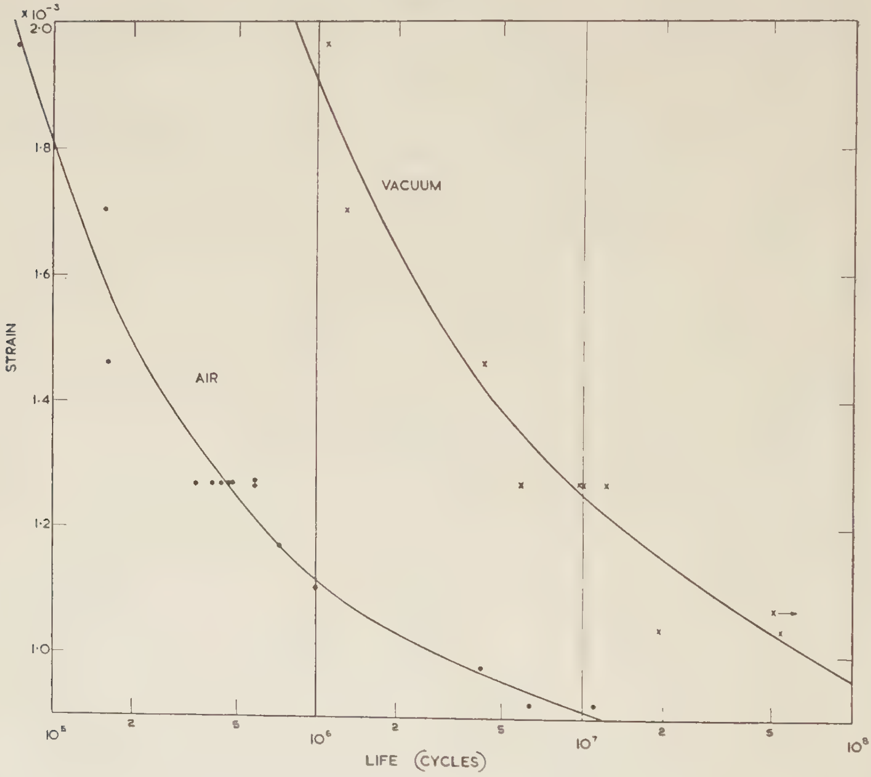

Copper. Endurance curves in air and vacuum.

4.1.2. *Aluminium*

Aluminium was chosen as a metal which is considerably more reactive chemically than copper. It was fatigued at one strain in various pressures of air with the results shown in fig. 5. The scatter of the results is worse than with the copper but it is clear that the life decreases as the pressure is increased. The total decrease is however rather less than that for the copper used. Two specimens fatigued in dry air had lives slightly longer than those fatigued in damp air. This is similar to the behaviour of copper.

However when aluminium specimens were fatigued in water vapour alone (air pressure about 10^{-3} mm Hg) they had lives similar to, or slightly shorter than, those of specimens fatigued in air.

Thus for aluminium water vapour alone is as detrimental as water vapour and air while air alone has slightly less effect.

Fig. 5

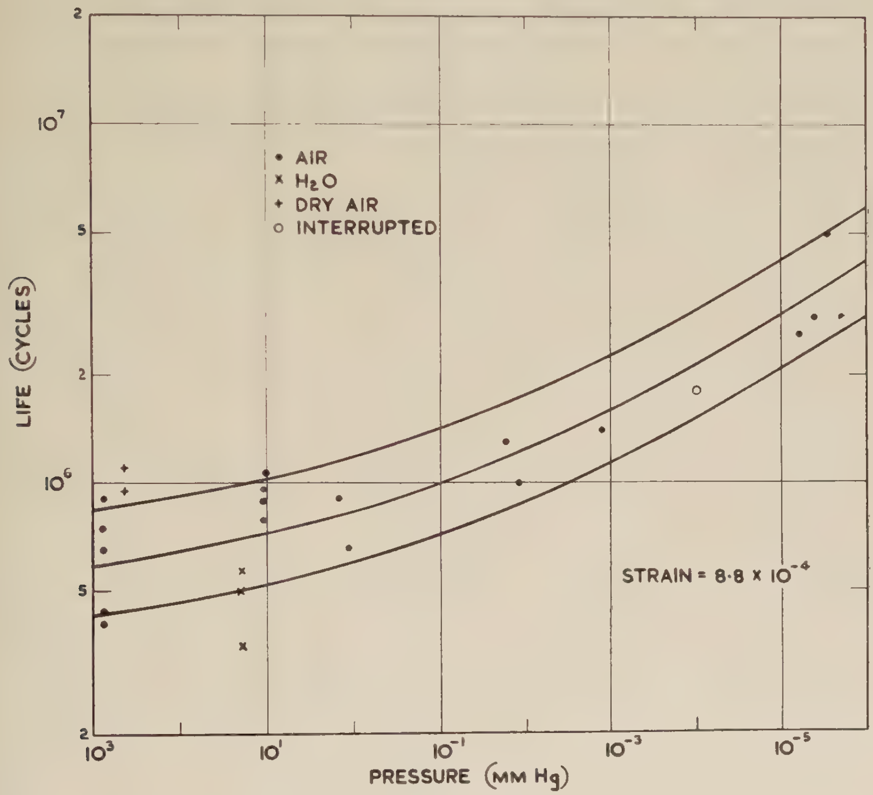

Aluminium. Fatigue life in various atmospheres.

4.1.3. *Gold*

Gold was chosen as a metal which was very much less reactive chemically than copper or aluminium. Five specimens were run at the same strain, three in air and two in vacuum. The results are shown in fig. 6. The specimens fatigued in air lasted slightly longer than those run in vacuum but it seems improbable that the difference is significant.

4.2. *Microscopical Observations*

4.2.1. *General*

Previous work on copper (Thompson *et al.* 1956) showed that early in the fatigue life some of the slip bands changed in such a manner that they were not removed by a short electropolish. Macroscopic cracks developed from these 'persistent' slip bands which only occurred on the surface.

Some of the specimens used in the present work were examined microscopically to investigate the fatigue process further, to determine on which stage of the fatigue damage the atmosphere had its main effect and incidently to establish the nature of the 'persistent' slip bands. The specimens were removed from the machine at intervals to allow this to be done.

Fig. 6

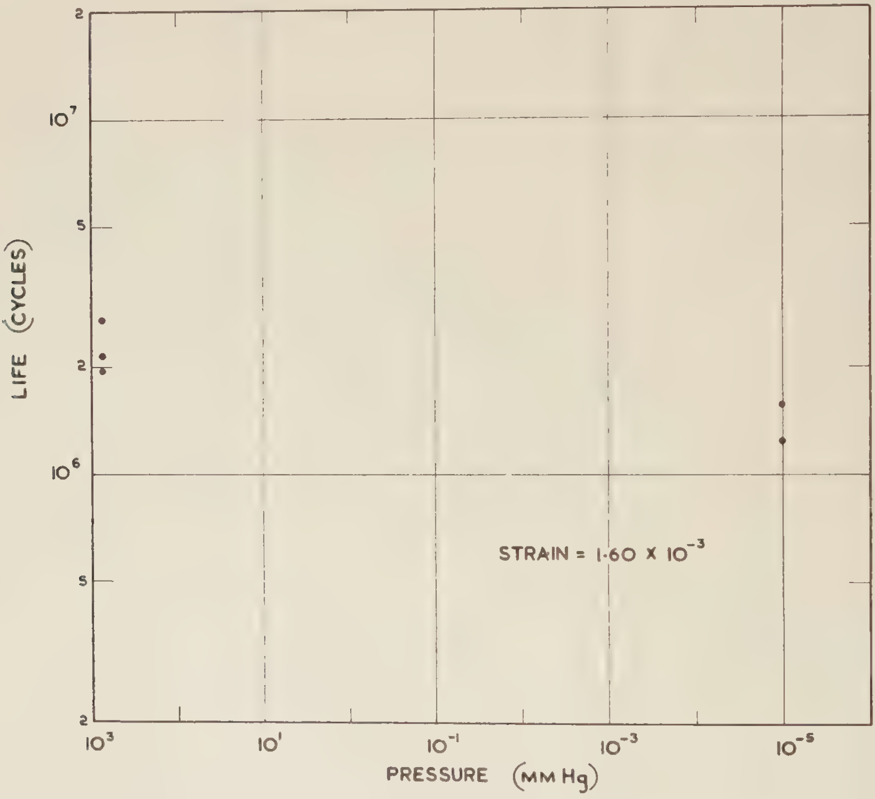

Gold. Fatigue life in air and vacuum.

4.2.2. *Copper*

Most of the observations were made on specimens strained at $1{\cdot}27 \times 10^{-3}$ giving lives in air of about 5×10^5 cycles.

During the test slip bands formed and became wider in the usual way. The surface of the bands was often quite rough and extrusions were common. Some extrusions formed after only a few thousand cycles and they frequently grew to heights of 5–7 microns after 10^5 cycles. When the specimen was lightly electropolished the fine structure of the slip band was smoothed off but the larger scale irregularities remained and the slip bands were visible as furrowed regions. The sloping surface of the slip bands caused them to appear dark under microscope objectives with a low acceptable angle but under high apertures the surface could usually be seen to be continuous. In a few cases however part of the bands appeared black even under high aperture objectives and the surface appeared to be discontinuous. These regions were rare after a thousand cycles but became increasingly common as the test proceeded. They formed in slip bands and also in twin boundaries and grain boundaries and spread slowly. The crack which eventually caused the failure of the specimen usually started from one of these 'cracks' in a grain boundary, and spread both across grains and along their boundaries. To see if these regions were in fact cracks as soon as the surface appeared to be discontinuous a specimen was fatigued for $1{\cdot}8 \times 10^4$ cycles to produce a number of them and was stretched. The strains used were much larger than those used by Thompson *et al.* (1956)—the specimens were pulled to fracture and the region near the neck was examined. Most of the black marks in the heavily strained region opened up showing that they were in fact shallow cracks. Figure 7, Pl. 80 shows a crack in a slip band. Most of the cracks were only one or two microns deep but a few were deeper, up to 12 microns. Thus some cracks had formed in slip bands and grain boundaries after about 1% of the life of the specimen and they were fairly common after 5%. Presumably the 'persistent' slip bands of Thompson *et al.* (1956) were in fact shallow cracks but the strains they used were insufficient to open them appreciably.

The specimens fatigued at the same stress in vacuum were examined and the same sequence of events was observed. After $1{\cdot}8 \times 10^4$ cycles at stress there were many cracks similar in appearance and the number to those found in a specimen fatigued in air for the same time. These developed in the same way as those in specimens fatigued in air but took much longer to do so. As a result the continuing slip roughened the surface much more and more surface cracks formed. Figure 8, Pl. 80 shows many slip band cracks in a specimen which had been fatigued to fracture in vacuum, electropolished and pulled.

Electron microscopical observations

In order to try to find more about the structure of the fatigue slip bands and, in particular, to investigate 'intrusion', a number of specimens were examined using the electron microscope.

Cottrell and Hull (1957) have shown that both extrusions and intrusions occur in fatigued copper at a small fraction of the total fatigue life. However they did not find the relative positions of the extrusions and intrusions and proposed a model which implies that they will form on different planes. Forsyth (1957), using AgCl, showed that they usually form on the same plane and near together but it was desirable to check this for a metal and find their relative positions.

It was difficult to strip replicas from specimens fatigued at a strain giving a life of about 5×10^5 cycles so a lower stress was used giving lives of 5×10^6 to 10^7 cycles. The specimens were fatigued to fracture to ensure plenty of cracks and then examined. A carbon replica was made (carbon was evaporated onto a stripped formvar replica which was then dissolved away), and this was shadowed with Au Pd at an angle of about $\tan^{-1} \frac{1}{3}$ from both sides in opposite directions. Thus extrusions would cast shadows in one direction while intrusions would cast shadows in the other. In this way both were clearly identified on the same replica. In the main it was found that small intrusions were more common than extrusions and sometimes occurred apparently by themselves. Figure 9, Pl. 80 shows one such area. In other places intrusions and extrusions occurred together although this was not very common. Figure 10, Pl. 80 shows such a place. The black regions, A, are end views of extrusions or intrusions which cast shadows (light on the print) at B and C respectively. In this case extrusions and intrusions occurred alternately along the slip bands. In a few places extrusions and intrusions occurred side by side in the same band. Figure 11, Pl. 81 shows this. Here the intrusion was considerably longer than the extrusion and its replica has folded over so it only casts a shadow at A while the shorter extrusion produces a shadow at B. These observations confirm that intrusion occurs in a similar manner to, and on the same planes as, extrusion. The intrusion appears to be rather the more common.

4.2.3. *Aluminium*

Smith (1957) has given a description of the metallography of fatigue damage in aluminium and showed that cracks had formed in both slip bands and grain boundaries after 10% or so of the specimen life. The aluminium used in the present tests behaved in a very similar manner. Slip and roughening were rather more pronounced than on copper specimens with similar lives. Slip band and grain boundary cracks were both common. The majority of the length of large cracks was within grains rather than along their boundaries.

If the specimens were examined a few thousand cycles after reaching stress they were seen to be covered with slip bands and often some extrusion was visible. Electropolishing removed the slip and showed that there were many cracks in the slip bands. Figure 12, Pl. 81 shows such an area after a tensile strain and shows that the marks were indeed cracks. An exactly similar sequence of events occurred when specimens were fatigued in vacuum. Cracks were already present by the time operating stress was reached. Thus it appears that in aluminium, as in copper, cracks form very early in the test and that the surrounding atmosphere only affects their rate of propagation.

4.2.4. *Gold*

Slip on gold occurred in much the same manner as on copper. Extrusion was often seen. The main difference was that the slip bands showed a tendency to develop into ditches often one or two microns deep and a few microns wide. Cracks formed at twin boundaries, grain boundaries and in slip bands. Figure 13, Pl. 81 shows slip bands and extrusion on a specimen fatigued for 3×10^4 cycles (about 1·5% of its life). Electropolishing removed the slip lines but left the roughness as before. Cracks could then be seen, particularly at twin boundaries. After pulling most of the cracks opened up as shown in fig. 14, Pl. 81.

Thus there were many cracks present after less than 2% of the life on the specimen and the vast majority of the fatigue life was spent in propagating cracks formed early in the test.

§ 5. DISCUSSION

This work has confirmed once again that in annealed pure metals the first fatigue cracks form very early in the fatigue life. They are demonstrably present and already some microns deep after a few per cent of the fatigue life of about half a million cycles. It seems probable that they actually form in the first few thousand cycles during the initial hardening period. There is still little evidence to show how the cracks start but since the surface of the slip band becomes rough and parts rise to a height of a micron or two quite quickly it seems plausible to suggest that other parts fall by a similar mechanism and form the initial crack. Figure 10 shows that intrusions of this type can occur and Cottrell and Hull (1957) have shown that intrusions occur quite early in the test.

The mechanism by which intrusion occurs is still obscure but it appears to be unaffected by the surrounding atmosphere as would be expected of a purely mechanical process. It is the rate of spreading of the small cracks to form larger cracks which is affected by the atmosphere. The effect of different gases on the rate of propagation depends on the metal being fatigued and indicates that chemical attack is involved. The corrosive substance must be present as a gas and while fatiguing is in progress. Neither oxide on the surface nor alternate applications of fatigue and air have any effect. This indicates that chemical attack at the root of the crack is necessary.

There is plenty of time for the gas to get to the tip of the crack even if the crack is completely closed during the compressive half cycle. If the gas molecules are not trapped on the walls then gas can diffuse a few tenths of a millimetre down a crack a few thousand angstroms across in a tenth of a cycle at the testing speeds used. A pressure of one atmosphere of an inert gas will not alter the diffusion rate appreciably.

Once the gas is at the tip of the crack it could assist propagation in two ways. It might attack the highly strained metal at the tip of the crack and so weaken it and help it to break. (A rate of attack of one atom layer per cycle would speed the early stages of the propagation considerably.) Alternatively a chemisorbed layer forming on freshly exposed surfaces as soon as they separated would make the separation irreversible and prevent the sides of the crack sticking together again on the compressive half cycle. It would be interesting to repeat the experiment at lower temperatures.

The form of the dependence of fatigue life on air (or oxygen) pressure is difficult to explain. Log life varies approximately linearly with log pressure over a pressure range of $10^8:1$. The change in life produced by this pressure range varies with the fatigue strain and the exact composition of the material being fatigued. For example at a strain giving an air life of 5×10^5 cycles the OFCH copper used in these experiments gave a factor of 20 : 1 while a few experiments on another, less pure, copper gave a larger scatter and a factor of about 10 : 1. Similarly Gough and Sopwith (1935) found the ratio of the endurance limit (3×10^7 cycles) in a vacuum of 10^{-3} mm Hg to that in air for four different coppers and obtained ratios of 1·02, 1·06, 1·06 and 1·13. Also Gough and Sopwith (1946) found that water vapour without oxygen had almost as large an effect on life as air did in contrast to the results reported here.

Clearly there must come a time when the fatigue life ceases to increase as the air pressure is reduced. Already, at 10^{-5} mm Hg, only 1% of the atom sites on the metal surface are hit by gas atoms in any one cycle. It would be interesting to find what is the smallest oxygen pressure needed to have any effect at all.

REFERENCES

COTTRELL, A. H., and HULL, D., 1957, *Proc. roy. Soc.* A, **242,** 211.
FORSYTH, P. J. E., 1957, *Proc. roy. Soc.* A, **242,** 198.
GOUGH, H. J., and SOPWITH, D. J., 1932, *J. Inst. Met.*, **49,** 93 ; 1935, *Ibid.*, **56,** 55 ; 1946, *Ibid.*, **72,** 415.
SMITH, G. C., 1957, *Proc. roy. Soc.* A, **242,** 189.
THOMPSON, N., WADSWORTH, N. J., and LOUAT, N., 1956, *Phil. Mag.*, **1,** 113.

The Occurrence of Stacking Faults in Metallic Systems†

By J. Spreadborough
Department of Metallurgy, The University Museum, Oxford

[Received June 19, 1958]

Abstract

A possible qualitative interpretation of the occurrence of stacking faults in metals and alloys is outlined, using an extension of the ideas of Altmann, Coulson and Hume-Rothery. The metals calcium, scandium and titanium, the ϵ-phase in iron–manganese, and the α-solid solutions of various B sub-group elements in the noble metals are treated as examples. The effect of temperature on hybrids is briefly discussed.

§ 1. Introduction

Altmann *et al.* (1957) suggested that the metallic bond had greater directional characteristics than had been previously assumed, particularly when there were many bonding electrons available. The purpose of the present work is to show that their ideas, with some extensions, provide a possible interpretation of the occurrence of stacking faults in metals and alloys and of the equilibrium diagrams in some simple binary systems.

Altmann *et al.* suggested that, whilst in metals there are not enough electrons to form chemical covalent bonds by using hybrid orbitals, if the hybrids are treated as being only *partly* occupied, then it may be justifiable to regard particular hybrids as determining the geometrical arrangement of atoms in metallic crystals. We may expect a metal to have a large number of resonating structures so that the weights of some of them may be very small. Some of these structures (e.g. the ionic ones) will have no marked directional properties, and Altmann *et al.* selected hybrids which would give directional character to the bonds, although because of their weight these hybrids might play only a minor part in determining other properties of the materials concerned. Qualitatively, the wave function is visualized as being expressed by several Slater determinants. Some of the energy terms will have no angular variation of significance, and some, corresponding to the selected hybrids of Altmann *et al.* will have considerable variation. The hybrids for the typical metallic structures obtained by these workers are given in table 1. Also listed are the s and p weights of these hybrids estimated in a similar way to the d weights of the above authors.

---

† Communicated by Professor W. Hume-Rothery, F.R.S.

The important things to note are that the p weights move in the opposite direction to the d weights as we go from b.c.c → c.p.h. → f.c.c., and that the s weights of the b.c.c. and c.p.h. hybrids are comparable.

Evidence for stacking faults in both close-packed structures has been obtained, and the fault parameter α, defined as the probability of finding a fault on any one close-packed plane, has been measured in some cases. There is a possibility of faults on $\{112\}$ planes in b.c.c. crystals (Hirsch and Otte 1957), but we shall not consider these. The x-ray theory treats faults as occupying whole planes in the crystal, and the observed diffraction effects are in accord with the theory. Qualitative arguments may be advanced which suggest that the narrow fault ribbons of extended dislocations would not give such effects and that wide faults are responsible (Christian and Spreadborough 1957). Support for this comes from electron microscope studies of thin foils, where the separation of partials to form wide faults was observed (Whelan *et al.* 1957). The force required to drive one partial from the other must exceed the restoring force due to the surface energy of the fault; the higher the surface energy, the harder it will be to produce a wide fault. Consequently it is thought that the measured α varies with the fault energy. Indirect arguments, based on the consideration of faults as thin twins, lead to the same conclusion.

Table 1

Structure	Hybrids	d weights	p weights	s weights
b.c.c.	(sd^3) (d^4) (d^3)	0·9	0	0·09
c.p.h.	(spd^4) (pd^5) (sd^2)	0·7	0·13	0·14
f.c.c.	(p^3d^3)	0·5	0·5	0

The suggestion is made that the tendency for a system existing as one close-packed structure to form either deformation or growth stacking faults is related to the difference in free energies of the two close-packed structures. (We cannot expect that the free energy of an effectively two-dimensional stacking fault will be the same as that for the bulk phase, for Brillouin zone effects, dependent on there being enough atoms present to give strong electron reflections, should be different for fault and bulk phase. However, in alloys, electrochemical effects which influence the shapes of free energy-composition curves should be the same for fault and bulk phase.) This is supported by work on the cobalt–nickel system, where it was found that the density of stacking faults introduced by deformation at room temperature in the f.c.c. alloys increased rapidly with cobalt content as the critical composition for the phase change f.c.c. → c.p.h. was approached (Christian and Spreadborough 1956). Further, Barrett and Massalski (1957) have observed that brass with a composition just beyond the alpha phase boundary transforms on cold work to a structure which is thought to be c.p.h. This suggests that there is a small difference between the free energies of the two close-packed structures. Deformed alpha-brass has been found to be heavily faulted (see § 4).

§ 2. CALCIUM, SCANDIUM AND TITANIUM

Altmann *et al.* suggested that it was reasonable to assume that at both ends of the Long Periods the d orbitals will be in an unfavourable position to enter into hybridization, and also that the d electrons tend to become atomic and non-bonding at an earlier stage in the First Long Period than in the later Periods. This view was suggested because of the correspondence between physical properties and predominant chemical valencies pointed out by Hume-Rothery *et al.* (1951).

Therefore on moving from calcium to titanium the d orbitals will play an increasing part and this leads to the close-packed hexagonal structure in Ti. Calcium transforms from f.c.c. to c.p.h. at ~450°C and it is possible to estimate the energy of a stacking fault, knowing the latent heat of transformation. This fault energy is found to be ~15 ergs cm^{-2} at room temperature, which is very low. So profuse stacking faults would be expected in deformed calcium. Deformed titanium contains large numbers of faults, with an estimated fault energy of ~10 erg cm^{-2} (Spreadborough, unpublished), and so we infer that the f.c.c. structure has energy not much higher than the c.p.h. In between Ca and Ti is scandium; from the above we should expect that it would have a transformation from one close-packed structure to the other near room temperature. Meisel (1939) reported that scandium existed as f.c.c. and c.p.h. at room temperature whilst Bommer (1939) and Spedding *et al.* (1956) found only c.p.h. at room temperature.

§ 3. THE ϵ-PHASE IN IRON–MANGANESE

To suggest an interpretation of this phase it is necessary to postulate that Mn does not follow the trend Fe–Mn–Cr of increasing weight in bonding because of the great stability of the Mn d^5 sub-group. (The effect of the stability of the d^5 sub-group on the properties of Mn was emphasized by Hume-Rothery *et al.*) Given this postulate, adding Mn to Fe will reduce the d weight of the system so that the hexagonal phase begins to have a stability comparable to, though lower than, the b.c.c., and so metastable ϵ-phase can be produced. This phase contains growth faults (Spreadborough, unpublished), and we should expect on the above reasoning that the growth faults would increase with Mn content. Finally, addition of sufficient Mn reduces the d weight to such an extent that the γ (f.c.c.) phase is stabilized.

§ 4. COPPER AND SILVER ALLOYS

An interpretation of the behaviour of these alloys at high noble metal content is possible if we take the Pauling view that the d-electrons in the noble metals contribute to the bonding. Let us then say that, in systems where Group B metals are dissolved in copper or silver, the part played by the d-orbital contributions from the copper or silver will be modified by progressive addition of solute.

Deformation stacking faults have been detected (and in some cases measured) in several alloys of copper and silver with B sub-group metals. The figure shows the curves for stacking fault parameter (α) versus electron concentration for four copper systems. The results for Cu–Sn, Cu–Ge and the low Zn content brasses are from Smallman and Westmacott (1957), those for high Zn content brasses from Warren and Warekois (1955) and those for Cu–Al, pure copper and a 30% brass from Christian and Spreadborough (1956, 1957). It appears that the curves shift to lower electron concentration with increasing valency of the added element.

Table 2

System	Hex. range	Size factor	Electrochem. factor	Notes
Cu–Al	(1·4)	+6·6	2·2	F β hex at low temp ?
Cu–Zn	1·7–1·85	+4·2	1·1	F
Cu–Ga	1·42–1·45	+6·6	0·9	F ?
Cu–Ge	1·35–1·5	−4·1	0·6	F
Cu–Si	1·32–1·42	−8·0	1·8	F high temp hex only
Cu–Sn	1·72–1·75	+9·6	0·5	F
Ag–Cd	1·5	+3·1	1·5	F
Ag–In	1·5	+2·1	1·2	F ?
Ag–Sn	1·37–1·6	−3·0	0·9	F*
Ag–Sb	1·35–1·65	+0·5	0·7	F*
Ag–Zn	1·7–1·85	−7·8	1·5	F

F = faults found and measured.

F* = faults observed qualitatively.

F ? = probably faults.

Hexagonal range in terms of electron concentration.

Electrochemical factor is difference in electrode potentials of the elements. Size Factor + denotes expansion of Cu, Ag lattice.

Now with reference to table 1, it is seen that the s weight of the hybrid regarded as determining the f.c.c. structure is zero, and that the s weights for c.p.h. and b.c.c. are roughly the same, with that for b.c.c. slightly lower. Let us take the case of adding Zn to Cu. The first effect will be to increase the s weight, and therefore to produce the b.c.c. structure first. However, this is also a step in the direction of stabilizing the c.p.h. structure, so we might explain the occurrence of faults in α-brass in this way. Further addition of Zn would tend to increase the p weight also, and the only way that both s and p weights can have non-zero values is for the system to adopt the c.p.h. structure. Now if we consider the series Zn,

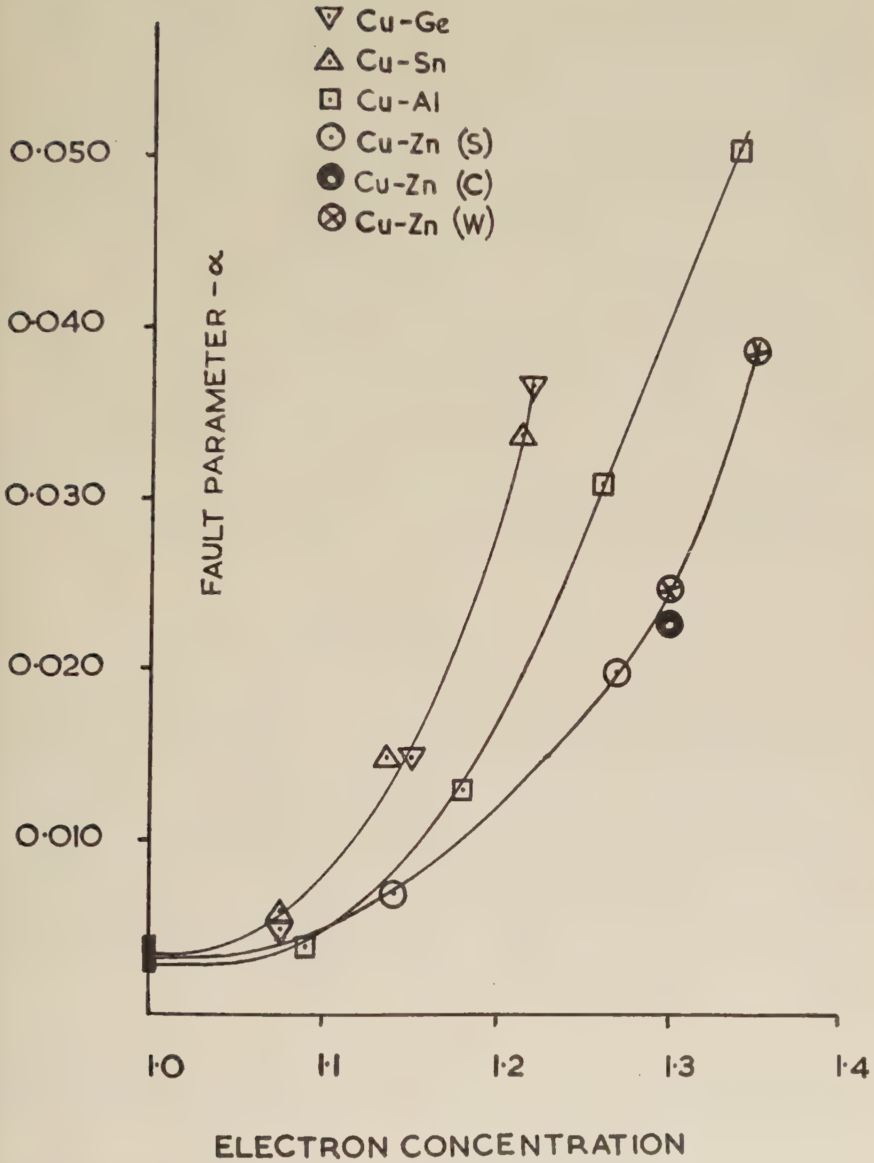

Deformation faulting versus electron concentration for some copper alloys.

(S) = Smallman and Westmacott.
(C) = Christian and Spreadborough.
(W) = Warren and Warekois.

Ga, Ge added to copper, the tendency will be for the p weight factor to occur earlier in Ga than Zn (i.e. at a lower electron concentration), and earlier in Ge than in Ga, and so we should expect the hexagonal phases to appear earlier in the equilibrium diagrams. Also, the tendency to form deformation stacking faults will move in the same direction.

Table 2 shows some systems where faults are found in copper and silver alloys. The hexagonal range column refers, in systems where more than one hexagonal phase is formed, to the first hexagonal phase going from the noble metal end of the diagram. The value (1.4) given for Cu–Al is because the β-phase transforms at low temperatures to a structure of hexagonal type. It is seen that the hexagonal phase appears at lower electron concentrations as we go from Cu–Zn → Cu–Ga → Cu–Ge.

In our discussion of the diagrams we neglected the size factor and electrochemical factor, both of which undoubtedly play an important part in the understanding of equilibrium diagrams. In the cases considered, however, the differences in these factors are probably not important, Similar arguments to the above may be used to interpret the silver systems Ag–Cd, Ag–In, Ag–Sn, but it should be said that the indications that the d-electrons in silver play a part in the binding are not so strong as for the case of copper.

§ 5. THE EFFECT OF TEMPERATURE ON HYBRIDS

It has been observed several times that the b.c.c. structure of an element is always the stable one at high temperatures. The usual interpretation is in terms of the large entropy of the b.c.c. structure (Zener 1948), but an interpretation is possible from our viewpoint. The d band in, say nickel, has a density of states over ten times greater than the s band; a roughly equivalent situation is expected for all the transition metals. It might be expected that the d band would broaden more with temperature increase than the neighbouring or overlapping p and s bands, consequently we should get greater participation by the d-hybrids as the temperature is raised. It is perhaps significant that the structure with the largest d weight is the b.c.c. structure.

ACKNOWLEDGMENT

The author would like to thank Professor W. Hume-Rothery, F.R.S. for his interest and encouragement.

REFERENCES

ALTMANN, S. L., COULSON, C. A., and HUME-ROTHERY, W., 1957, *Proc. roy. Soc.* A, **240,** 145.

BARRETT, C. S., and MASSALSKI, T. B., 1957, *J. Metals*, **9,** 455.

BOMMER, H., 1939, *Z. Elektrochem*, **45,** 375.

CHRISTIAN, J. W., and SPREADBOROUGH, J., 1956, *Phil. Mag.*, **1,** 1069 ; 1957, *Proc. phys. Soc. Lond.* B, **70,** 1151.

HIRSCH, P. B., and OTTE, H. M., 1957, *Acta cryst.*, **10,** 447.

Hume-Rothery, W., Irving, H. M., and Williams, R. J. P., 1951, *Proc. roy. Soc.* A, **208,** 431.

Meisel, K., 1939, *Naturwissenschaften*, **27,** 230.

Smallman, R. E., and Westmacott, K. H., 1957, *Phil. Mag.*, **2,** 669.

Spedding, F. H., Daane, A. H., and Herrmann, K. W., 1956, *Acta cryst.*, **9,** 559.

Warren, B. E., and Warekois, E. P., 1955, *Acta Met.*, **3,** 473.

Whelan, M. J., Hirsch, P. B., Horne, R. W., and Bollman, W., 1957, *Proc. roy. Soc.* A, **240,** 524.

Zener, C., 1948, *Elasticity and Anelasticity of Metals* (Chicago : University Press), p. 37.

The Magnetization of Cobalt–Aluminium, Cobalt–Silicon, Iron–Aluminium and Iron–Silicon Alloys†

By D. PARSONS, W. SUCKSMITH and J. E. THOMPSON
Physics Department, University of Sheffield

[Received July 1, 1958]

ABSTRACT

The rate of change of magnetic moment with composition in several ferromagnetic cobalt-rich and iron-rich alloys of these systems has been derived from measurements of the variation of spontaneous magnetization with temperature. The measurements were made on the high-temperature face-centred cubic phase of the cobalt alloys, the magnetic moments at absolute zero being obtained by a suitable extrapolation procedure. In the Fe–Al and Fe–Si alloys, the initial rate of change of moment with composition corresponds to a simple dilution of the iron by the solute element, and increases in the range of compositions where ordering is known to exist. In the Co–Al and Co–Si alloys, the rate of change of moment with composition does not correspond to the number of valence electrons normally associated with the solute elements.

§ 1. INTRODUCTION

OUR present knowledge of the structure of the incomplete shells of the transition elements arises largely from measurements of the ferromagnetic saturation intensities both of the ferromagnetic metals and of their alloys.

The effect of composition on magnetic moment of a number of nickel alloys has been studied by Alder (1916), Sadron (1932) and Marian (1937). In many cases, a linear decrease of the magnetic moment per atom with composition was found over a considerable range. It is convenient to express these, and other, results by giving the initial rate of change of mean moment with atomic composition, dp_B/dc (where c is the atomic concentration of the solute element and p_B is the mean moment per atom). Alder found dp_B/dc for the nickel–copper system to be $-1{\cdot}0$, and in other cases the reduction in moment per substituted atom is approximately equal to the respective number of loosely bound electrons, or effective valency number. The position with regard to the data on the effect of added elements on the magnetic moments of iron and cobalt is much less satisfactory than that for nickel alloys. Very few suitable elements dissolve in iron to any marked extent, and with cobalt, difficulties involving change of phase have, until recently, prevented sufficiently reliable data from being obtained. Recent work on the nickel–copper system (Ahern and Sucksmith 1956) indicates that the value of dp_B/dc is nearer $-1{\cdot}16$, and for the copper–cobalt system Crangle (1955) obtained a value for

---

† Communicated by the Authors.

dp_B/dc of $-2{\cdot}25$ (i.e. $-1{\cdot}13$ per added electron) suggesting that the simple theory of Mott (1935) calls for some modification. The aim of the present work is to supplement the work described, and to compare the behaviour of iron and cobalt when alloyed with the same element. In addition, if cobalt is also to be compared with nickel, it seemed desirable to make measurements on the face-centred cubic phase of cobalt, in order to compare ferromagnetic elements of the same phase.

§ 2. Previous Work

It is well known that in pure cobalt a change in phase occurs near 400°c, the equilibrium crystal structure being face-centred cubic above this temperature, and hexagonal close-packed below. This introduces a difficulty in determining the magnetic moment of the face-centred cubic phase of cobalt and its alloys. Myers and Sucksmith (1951) developed an extrapolation technique based on the similarity in shape in the graphs of the spontaneous magnetization against temperature which they found for face-centred cubic cobalt and for nickel. Crangle (1957) developed a technique for determining the magnetic moment of alloys, the reduced curves of which are not identical to that of nickel, and obtained measurements on the face-centred cubic and hexagonal phases of the cobalt–chromium and cobalt–manganese systems (1957), and on the face-centred cubic phase of the cobalt–copper system (1955).

Other measurements on the cobalt alloys were made by Sadron (1932), on the hexagonal phase of cobalt–silicon alloys containing up to 13·3% silicon, and by Farcas (1937) on the cobalt–chromium, cobalt–aluminium, cobalt–molybdenum and cobalt–tungsten systems. Farcas measured the Curie points and the magnetization of the alloys at room temperature, applying a correction which was dependent on the Curie point to the latter to obtain the magnetization at absolute zero. Furthermore, as it seems unlikely in the light of present knowledge that the alloys were all of single phase, the usefulness of the results seems open to some doubt.

Magnetic measurements on the iron–aluminium and iron–silicon systems were made by Fallot (1936), the alloys having been cooled slowly from 1050°c to room temperature. In both cases, it was found that the initial slope of the p_B against composition curve indicated a pure dilution of the iron by the solute atom, the curve falling more rapidly at compositions higher than about 10% of the solute. In particular, the iron–aluminium had a sharp minimum at 25% aluminium. Later, Sucksmith (1939) found no such minimum, but did find that in alloys containing greater than 20% aluminium, the spontaneous magnetization was sensitive to heat treatment. This was considered to be a consequence of an order–disorder reaction.

§ 3. Preparation of the Specimens

The alloys were made by two methods.

The iron–aluminium, iron–silicon and cobalt–aluminium alloys were prepared by melting in a high frequency induction furnace. Recrystallized alumina crucibles were used, the melting being carried out in an atmosphere of argon at a pressure of about 5 in. of mercury. The cobalt–silicon alloys were prepared in an argon arc furnace.

The materials used were as follows; the iron was Johnson-Matthey "H.S." iron, 99·9% pure, the aluminium was "super-purity" aluminium, the silicon, from New Metals and Chemicals, was 99·8% pure, and the cobalt, presented by the Société Général Métallurgique de Hoboken, Antwerp, was 99·9% pure.

Ingots prepared by both methods were subsequently heated for three days at about 1100°C *in vacuo*, to ensure homogeneity. In the iron alloys, where the effects of ordering were apparent, the specimens were sealed, after final machining, in thin quartz tubes, heated to about 900°C for two or three hours, and water-quenched to retain the disordered state.

The alloys were analysed chemically for the amount of solute element, and also spectrographically for the presence of impurities, the analyses being shown in the table. Any impurities were present in amounts of less than 0·01%.

System	% solute (weight)	% solute (atomic)	Curie temp. °C	p_B per atom (quenched)	p_B per atom (annealed)
Fe–Al	3·10	6·23	764	2·07	—
	3·65	7·20	765	2·05	—
	5·08	9·99	749	1·99	—
	11·50	21·20	655	1·64	1·60
	10·20	19·10	676·2	1·71	1·69
Fe–Si	3·55	6·83	749	2·06	—
	4·98	9·45	737·5	1·99	—
	8·44	15·50	674	1·70	1·68
Co–Si	2·23	4·57	957	—	1·49
	1·09	2·26	1042·5	—	1·62
Co–Al	0·94	2·03	1048	—	1·65
	1·58	3·39	994	—	1·57
	2·11	4·50	964	—	1·51

§ 4. EXPERIMENTAL METHODS

Measurements of magnetization in applied magnetic fields of between 3 and 17 kilo-oersteds were made using experimental methods which have now become standard in this laboratory, and the established extrapolation techniques were used to obtain values of the spontaneous magnetizations of the alloys at temperatures up to their respective Curie points (see Crangle 1955). The Curie points were estimated by plotting graphs of the squares of the spontaneous magnetizations against temperature, the parts with steepest slope being extrapolated to the temperature axis. The determination of the Curie point was estimated to be accurate to less than ±2°c.

The usual sequence for the cobalt–aluminium and cobalt–silicon alloys was to measure the magnetizations from about 700°c downwards to the temperature of the phase change, so as to obtain measurements on the face-centred cubic phase over the maximum possible range, and then upwards to the Curie point. In this way, trouble due to possible solute loss by preferential evaporation at the highest temperatures was reduced. For these cobalt alloys, since no low temperature measurements were possible on the face-centred cubic phase, the method for obtaining $\sigma_{0,0}$, the spontaneous magnetization at absolute zero, described by Crangle (1957) was employed. For each measured value of the spontaneous magnetization of the alloy, $\sigma_{0,T}$, the corresponding temperature, T, is reduced to T/θ, where θ is the Curie point of the alloy. From the graph of $\sigma_{0,T}/\sigma_{0,0}$ against T/θ for pure face-centred cubic cobalt, the value of $\sigma_{0,T}/\sigma_{0,0}$ corresponding to this value of T/θ is read off. Values of $\sigma_{0,T}$ for the alloy are then plotted as a function of the corresponding values of $\sigma_{0,T}/\sigma_{0,0}$ for pure cobalt having the same value of T/θ and the linear portion of the graph is extrapolated to $\sigma_{0,T}/\sigma_{0,0}=1$ to obtain $\sigma_{0,0}$ for the alloy.

The magnetization of the iron–silicon and iron–aluminium alloys was measured heating from −200°c to above the Curie point of the specimen, and then as the temperature was slowly reduced to room temperature. The measurements below room temperature, at liquid air and solid CO_2 temperatures, were then repeated. In this way, changes in magnetization due to order–disorder phenomena could be followed, starting with the disordered state. For these alloys, the spontaneous magnetizations in the temperature range $0<T/\theta<0{\cdot}3$, where θ is the Curie temperature of the alloy, were plotted as a function of both T^2 and $T^{3/2}$, the better linear extrapolation to absolute zero of the two being used to obtain $\sigma_{0,0}$ for the alloy.

§ 5. RESULTS

5.1. *The Cobalt–Aluminium System*

According to Schramm (1941), the solubility limit of aluminium in cobalt at 400°c is about 4%, rising to about 10% at 1100°c. The addition of aluminium to cobalt causes the equilibrium temperature of the hexagonal to face-centred cubic phase change to fall from over 400°c to about 350°c at the solubility limit. The change is sluggish, and on cooling from high temperatures, the face-centred cubic phase can be retained in a non-equilibrium state for a significant range of temperatures below the equilibrium phase change temperature.

The variation of magnetic moment with composition for this system is shown graphically in fig. 1. This graph extrapolates to zero magnetic moment at a composition of 33% aluminium, and the slope gives a value of dp_B/dc of $-5{\cdot}3\ \mu_B$ per solute atom. The shape of the $\sigma_{0,T}$ against T curves for the alloys containing 8·86% and 10·24% Al was dependent on heat treatment. This was assumed to be a consequence of the simultaneous presence of both face-centred cubic and hexagonal phases. The extrapolation graph to obtain $\sigma_{0,0}$ for the alloy containing 6·99% aluminium consisted of three distinctly separate linear portions, and so it was assumed that this alloy was also of mixed phase.

Fig. 1

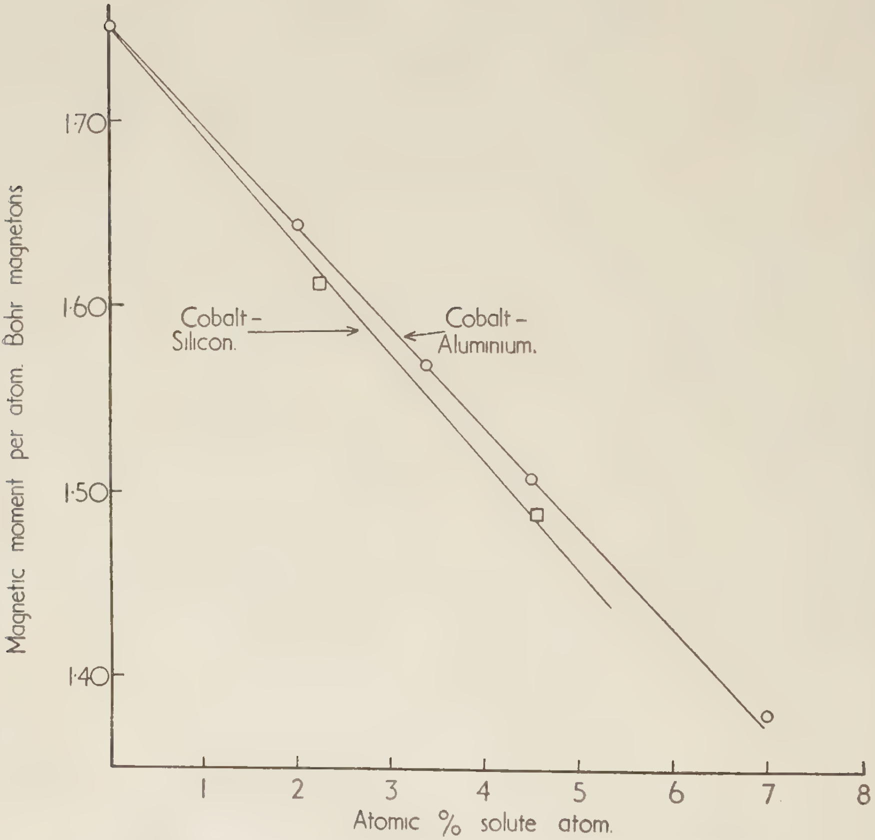

Magnetic moments of the cobalt–aluminium and cobalt–silicon alloys, plotted as a function of composition.

5.2. *The Cobalt–Silicon System*

The addition of silicon to cobalt causes the equilibrium temperature of the phase change from hexagonal to face-centred cubic to rise (Hansen 1936), and so, as the Curie temperature of the alloy system falls with increasing silicon content, the face-centred cubic phase is not ferromagnetic above a composition of about 16% silicon.

The variation of magnetic moment with composition is plotted with the results for the cobalt–aluminium system in fig. 1, the straight line extrapolating to zero moment at a composition of 31% silicon, and having a slope, dp_B/dc, of $-5{\cdot}7\ \mu_B$ per solute atom. The alloy containing 6·59% silicon was disregarded, obviously being of mixed phase by virtue of the complexity of the $\sigma_{0,T}-T$ curve.

The Curie points of both the cobalt–aluminium and cobalt–silicon alloys lie on the same straight line in the range of compositions measured, the line extrapolating to the absolute zero at a composition of about 40% solute content.

The value of dp_B/dc for the cobalt–aluminium system obtained from the present work disagrees with the value obtained by Farcas by an amount which is much greater than present experimental error. On the other hand there is fair agreement between the value of dp_B/dc obtained for the cobalt–silicon system derived from present work and that obtained by Sadron.

5.3. *The Iron–Aluminium System*

Within the range of temperatures and compositions measured, the alloys are body-centred cubic (Hansen 1936), but there is a tendency for the Fe_3Al super-lattice to be formed. Bradley and Jay (1932) found, by x-ray methods, that the annealed alloys showed ordering properties at a composition of about 18% aluminium, and that, at 25% aluminium ordering was nearly complete.

The measurements on the two alloys of lowest aluminium content (6·23% Al and 7·20% Al) revealed no ordering properties, but the alloy containing 9·99% Al did suggest ordering on cooling slowly from 800°c. The change in magnetization at a particular temperature, however, was only of the order of 0·5 in σ, and so was of the same order of magnitude as the limits of accuracy of the measurements. In the case of the alloys of the highest aluminium content (19·10% Al and 21·20% Al), the values of $\sigma_{0,0}$ for the quenched specimens were markedly higher than the corresponding values of the specimens slow-cooled from the region of the Curie point. The $\sigma_{0,T}$ against temperature curves for these alloys, showing the effect of ordering on magnetization are shown in fig. 2.

A linear decrease of magnetization with composition was found for compositions up to about 10% aluminium, the value of dp_B/dc being $-2{\cdot}2$, indicating a dilution of the iron by the aluminium and being in good agreement with the results of Fallot and of Sucksmith. At higher aluminium content, in the range of compositions where order–disorder phenomena are observed, the results are much more diffuse and scattered, this probably being due to some extent to the degree of order of the specimens. Nathans *et al.* (private communication) using neutron

Fig. 2

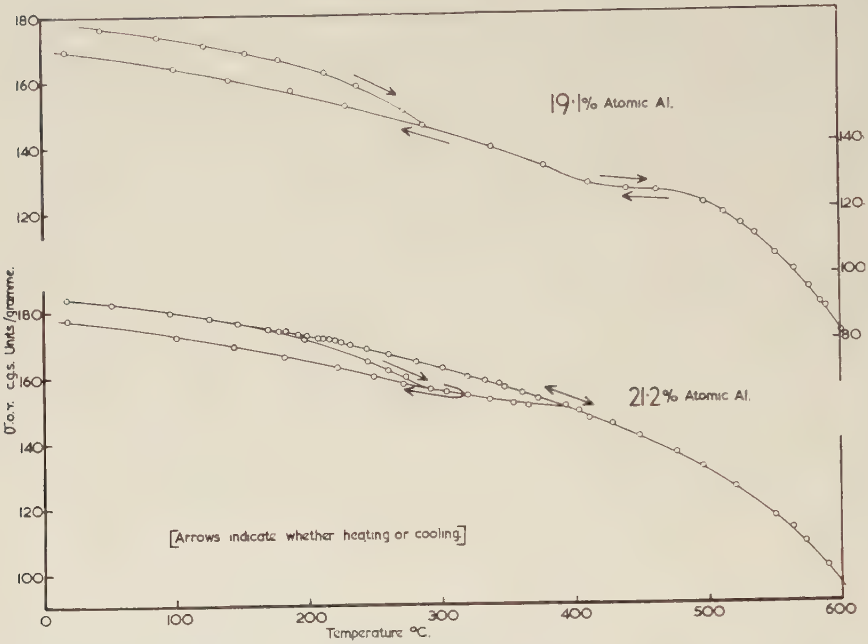

Spontaneous magnetization–temperature curves for iron–aluminium alloys containing 19·1 and 21·2% aluminium, showing the effect of ordering on spontaneous magnetization.

diffraction techniques, have measured the magnetic moments of the individual iron atoms on the two different sites in the ordered Fe_3Al lattice (fig. 3). They found that whilst the magnetic moment of an iron atom, the eight nearest neighbours of which are iron atoms (D sites), remains

Fig. 3

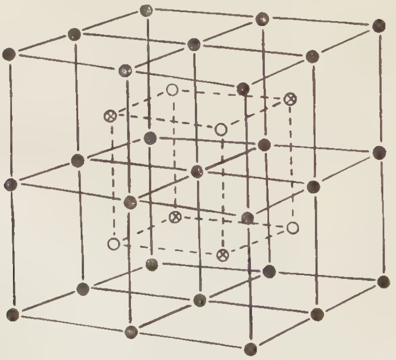

Unit cell of the ordered Fe_3Al structure.
- ● Iron atoms on A sites.
- ⊗ Iron atoms on D sites.
- ○ Aluminium atoms on B sites.

at 2·2 μ_B, the magnetic moment of an iron atom, the eight nearest neighbours of which are four iron atoms and four aluminium atoms (A sites), is only 1·6 μ_B. On this basis, the mean moment per iron atom of the ordered Fe_3Al structure is 1·8 μ_B, while the mean moment per iron atom of the disordered structure, where on the average, no iron atom will have a high proportion of nearest neighbour aluminium atoms, may be intuitively expected to be higher. Without any information from neutron diffraction observations, it is not possible to deal with the case of the ordered alloy containing 20% aluminium rigorously, as the moment of the iron atoms is known only for two types of environment. If, however, it is

Fig. 4

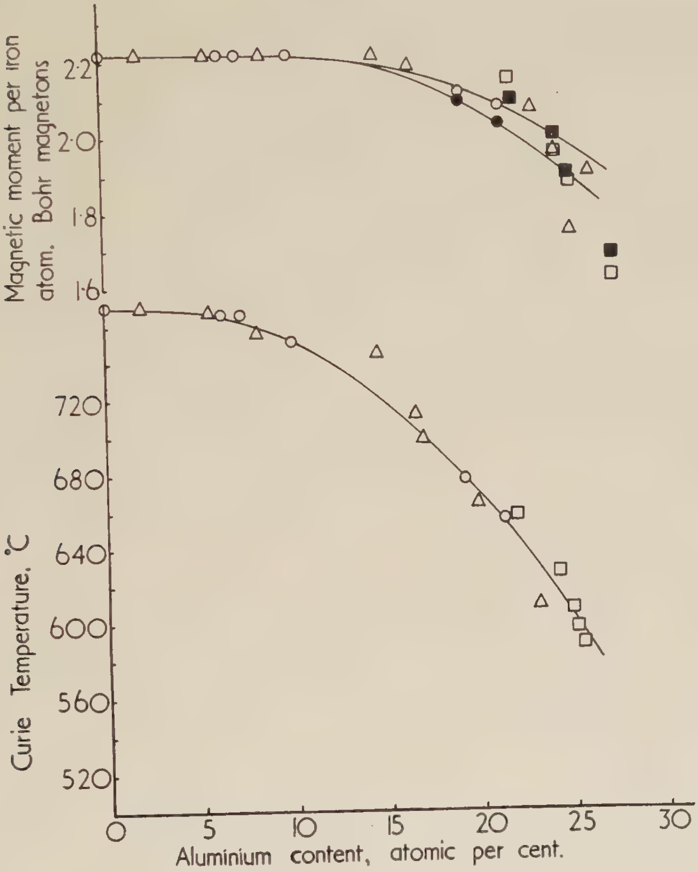

Magnetic moments and Curie points of the iron–aluminium alloys plotted as a function of composition. Triangles, Fallot; squares, Sucksmith; circles, present work. Open circles and squares indicate quenched alloys and closed circles and squares indicate annealed (slowly cooled) alloys.

assumed that for every aluminium atom there is an iron atom on a D site with a p_B value of $2{\cdot}2\ \mu_B$, and two iron atoms on A sites with p_B values of $1{\cdot}6\ \mu_B$, the remaining iron atoms having p_B values of $2{\cdot}2\ \mu_B$, then the mean moment per iron atom is $1{\cdot}90\ \mu_B$. Again the mean moment per iron atom of the disordered alloy might be expected to be higher, but not so much higher as in the 25% aluminium alloy. In order to compare the magnetic intensity measurements with the neutron measurements, the results of the present work together with the results of Fallot and of Sucksmith have been presented graphically in fig. 4, where the magnetic moment per iron atom has been plotted as ordinate against aluminium content as abscissa. The graph indicates that initially the mean moment per iron atom remains at about $2{\cdot}2\ \mu_B$ and then begins to fall off above 10% aluminium content. The interpolated experimental values from the present work of the mean moment per iron atom for an ordered and disordered alloy containing 20% aluminium are $2{\cdot}07\ \mu_B$ and $2{\cdot}10\ \mu_B$ respectively. At lower aluminium content, the environment of the iron atoms in the ordered and disordered states becomes less different, and so it would be expected that the difference between ordered and disordered magnetizations would become less. Hence the present results may be regarded as agreeing with the neutron diffraction evidence.

The reduced magnetizations, $\sigma_{0,T}/\sigma_{0,0}$, were obtained for each alloy, and plotted against the reduced temperature, T/θ where θ is the Curie point. Such reduced curves for this system, in common with several other binary alloy systems, tend to become less full with increasing solute content.

5.4. *The Iron-Silicon System*

The solubility limit of silicon in iron is about 25%, and so all the present work was carried out well within the solid solution region. (See, for example, Guggenheimer *et al.* 1948.) As in the iron–aluminium system, ordering takes place to form the Fe_3Si superlattice. According to Phragmén (1926), the ordering begins at a composition of about 13% silicon content.

The two alloys of lowest silicon content (6·83% Si and 9·45% Si) showed no ordering properties, but the alloy containing 15·5% silicon ordered easily at room temperature so that it was not possible to make reliable measurements on a completely disordered specimen of this alloy.

As with the iron–aluminium system, an initial linear decrease of magnetization with composition was found giving a value of dp_B/dc of $-2{\cdot}2$, indicating a dilution of the iron by the silicon. The magnetic moment per iron atom against silicon content is plotted in fig. 5, again stressing that the moment per iron atom remains unaltered at compositions below about 10% silicon content, but then falls off rapidly at higher compositions. There are no neutron diffraction data available to effect a direct comparison between the magnetic moments of the iron atoms on the D sites in the Fe_3Al and Fe_3Si superlattices.

The Curie points of the iron–silicon alloys, plotted as a function of silicon content (fig. 5) lie on a smooth curve, in marked contrast to the results of Fallot.

The shape of the reduced curves for the disordered Fe Si alloys varies in a similar way to the iron–aluminium alloys, and one may deduce that, in general, the two alloy systems have many features in common.

Fig. 5

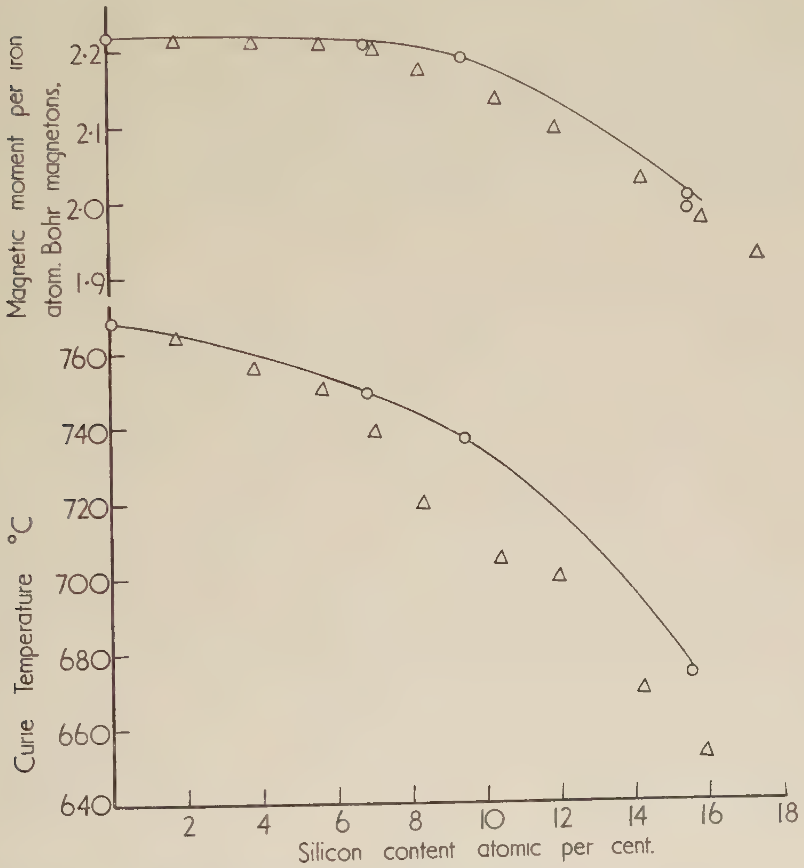

Magnetic moments and Curie points of the iron–silicon alloys plotted as a function of composition. Triangles, Fallot; circles, present work.

Acknowledgments

The authors wish to record their gratitude to Dr. J. Crangle for his helpful interest throughout the work, and to the Société Générale Métallurgique de Hoboken, Antwerp, for the gift of the pure cobalt on which some of the alloys were based. One of us (D. P.) wishes to acknowledge the award of an Ellison Fellowship by the University of Sheffield during the tenure of which some of the work described was carried out.

References

Ahern, S. A., and Sucksmith, W., 1956, *Proc. phys. Soc. Lond.* B, **69,** 1050.

Alder, M., 1916, Thesis, Zürich.

Bradley, A. J., and Jay, A. H., 1932, *Proc. roy. Soc.* A, **136,** 210.

Crangle, J., 1955, *Phil. Mag.*, **46,** 499; 1957, *Ibid.*, **2,** 659.

Fallot, M., 1936, *Ann. Phys., Paris*, **6,** 305.

Farcas, T., 1937, *Ann. Phys., Paris*, **8,** 146.

Guggenheimer, K. M., Heitler, H., and Hoselitz, K., 1948, *J. Iron St. Inst.*, **158,** 192.

Hansen, M., 1936, *Der Aufbau der Zweistofflegierungen* (Berlin: Springer).

Marian, V., 1937, *Ann. Phys., Paris*, **7,** 459.

Mott, N. F., 1935, *Proc. phys. Soc. Lond.*, **47,** 571.

Myers, H. P., and Sucksmith, W., 1951, *Proc. roy. Soc.* A, **207,** 427.

Phragmén, G., 1926, *J. Iron St. Inst.*, **114,** 397.

Sadron, C., 1932, *Ann. Phys., Paris*, **17,** 371.

Schramm, J., 1941, *Z. Metallk.*, **33,** 381.

Sucksmith, W., 1939, *Proc. roy. Soc.* A, **170,** 551.

Stripping at Low Energies†

By D. H. Wilkinson
Clarendon Laboratory, Oxford

[Received June 28, 1958]

Abstract

Deuteron-induced reactions of low Q-value show strikingly good stripping patterns at low deuteron bombarding energy (less than 2 MeV). High Q-values lead to bad stripping patterns. This is because, with a low Q-value, stripping can take place when the stripped nucleon is remote from its partner in the deuteron, and is therefore free from disturbing interactions.

It is usually said that deuteron reactions proceed predominantly by stripping at moderate deuteron energies (say 10 MeV) and predominantly by compound nucleus formation at low deuteron energies (say below 2 MeV). It is however clear that considerable compound nucleus formation usually takes place even at moderate deuteron energies because the dips in the experimental angular distribution are rarely as deep as simple stripping theory predicts and the cross section at backward angles is not small. The latter effect may also be associated with exchange contributions to stripping; however these are themselves due to a close approach to the bombarded nucleus of the exchanging nucleon so one may say that, one way or another, stripping patterns at moderate deuteron energies usually show evidence for the close approach to the target nucleus of both nucleons of the deuteron. It is also clear that the low energy interactions usually show some sign of stripping even though the angular distributions may be largely isotropic. There is, however, one class of low bombarding energy (d, p) reactions where the stripping pattern is very well developed‡ and where it sometimes becomes superior to those obtained with the higher bombarding energies where stripping is popularly supposed to enjoy its best successes. This class of reactions is those of low Q-value. It is also a strikingly recurrent phenomenon that in reactions where several excited states are reached those states with low Q-value (± 1 MeV or so) show good stripping patterns while the states of high Q-value show poor patterns. This effect is also seen in (d, n) reactions through much of the 1p shell; that in (d, p) reactions persists much further.

---

† Communicated by the Author.

‡ In the sense of the disintegration product nucleon appearing overwhelmingly in the forward hemisphere with a distribution which may be well represented for all angles by a Butler–Born pattern with a suitable choice of the effective stripping radius.

There is a simple qualitative explanation for this. If the deuteron energy is low and the Q-value is high the departing energetic proton—consider (d, p) - must derive its correspondingly high momentum chiefly from the deuteron ground state wavefunction since there is little in the bulk motion of the deuteron. This means that when it is stripped off it must be close to the neutron in order to be enjoying the strong interaction with it from which it gets high momentum. But stripping takes place when the neutron is at the nuclear surface so the proton which is near the neutron must also be near the nuclear surface; it is therefore likely to be interacting strongly with the nucleus when it is stripped off and so at best the stripping pattern will be badly distorted and at worst the nucleus will capture the proton as well as the neutron and we shall get compound nucleus formation rather than stripping. But if now the Q-value is low the proton needs little momentum, and it can find this from the deuteron ground state wavefunction even though its separation from the neutron is great. Momenta corresponding to a proton energy of the order of the deuteron binding energy are abundantly present when the neutron and proton are separated by the order of the relaxation length of the deuteron wavefunction (4·3 fermis). We must also ensure that the neutron's requirement for momentum for its attachment at the nuclear surface with the correct orbital angular momentum $l\hbar$ does not demand a closer neutron–proton approach at stripping. The semi-classical condition is: $l^2 < B/(\hbar^2/mR^2)$ where B is the deuteron binding energy and R is the stripping radius. If we insert $R = 8$ fermis which is a typical value found for low-energy, low Q-value, stripping this expression suggests that the present ideas should be adequate for $l = 0$, 1 and 2. So if the Q-value is low the departing proton need never approach within several fermis of the nuclear surface even as the neutron attaches; its interaction with the nucleus is therefore weak and a good stripping pattern results. Furthermore, compound nucleus formation is relatively discouraged because for that to happen the proton must get to the nuclear surface, and this involves it in several fermis' worth of further penetration through the Coulomb barrier beyond the point where it could have stripped off. The essential correctness of this picture is indicated by the angular distributions themselves which, even for as low a deuteron bombarding energy as $E_D = 1$ MeV are, for the low Q-value reactions, peaked predominantly forward in the centre of mass system. This shows that the deuteron is taking in considerable angular momentum. For a neutron attaching at 8 fermis with the proton one deuteron relaxation length away this angular momentum of the deuteron is about $3\sqrt{E_D}$ units if E_D is in MeV. So the qualitative features of the angular distribution are themselves enough to establish that the intermediate system is a very open one such as is proposed in the present model and bears no resemblance to the compound nucleus situation.

This relative favouring of stripping owing to the Coulomb barrier is not so pronounced in the case of a high Q-value because then the proton, as we have seen, must in any case approach close to the nuclear surface—even though it is going to strip. Also, if we are considering (d, p) reactions in which the ground state Q-value is low because the residual nucleus is of $T_z = +1$, the alternative (d, n) reaction to the $T_z = 0$ nucleus will have a high Q-value, and so if a compound nucleus should be formed it is much more likely to decay by neutron than by proton emission. This tends to keep the low Q-value (d, p) stripping uncontaminated by much compound nucleus contribution even if a compound nucleus is formed with good probability. In the case of the high Q-value reaction, however, not only is the stripping pattern likely to be poorer for the reasons given but also the contribution into that channel following compound nucleus formation is greater.

Another influence of the Coulomb barrier in improving the stripping pattern comes about because proton emission in the backward direction, owing to the finite linear momentum of the deuteron, requires a greater momentum to be found from the ground state wavefunction. The correspondingly closer approach of the proton to the neutron implies a deeper penetration by the proton into the Coulomb barrier and this will be discouraged.

These last considerations are not present in the reactions initiated by higher energy deuterons and so we can understand why the purest stripping patterns are indeed found for low, not high bombarding energies. More generally we might expect to find good stripping patterns when the momentum taken away by the proton is roughly equal to that which it had in the bulk motion of the deuteron, viz. when $E_D \sim -2Q$ or slightly higher to allow for the diminution of the deuteron's momentum due to the Coulomb field. It also explains why the present effect is most marked for (d, p) not (d, n) reactions especially for the heavier nuclei.

Another consideration which is related to the large proton–neutron separation at stripping is that when the Q-value is low the binding energy of the ingoing neutron in the residual nucleus is also low (greater than the Q-value by the binding energy of the deuteron). In this case the neutron wavefunction in the final state has a long relaxation length outside the nucleus and so stripping need not take place when the ingoing neutron is at the nuclear surface but can take place when it is anywhere in the long exponential tail. For example, for $Q \sim 0$, stripping when the neutron is 3 fermis from the nuclear surface is seen to be quite likely; at the same time the proton may, as we have seen, be 4 fermis further out still, a total of some 7 fermis from the nuclear surface and well outside the influence of the nucleus. As the Q-value increases the proton must approach the neutron and the neutron the nucleus so the nucleus rapidly begins to see the proton and simple stripping breaks down.

It is a clear prediction of this argument that the effective stripping radius for these low bombarding energy, low Q-value, reactions will be greater than for high Q-value reactions. This is due partly to the importance of the Coulomb repulsion and partly to the long tail of the neutron wavefunction in the final state. We also anticipate that, *ceteris* *paribus*, the effective stripping radius will be smaller the higher the Q-value of the ingoing neutron since the tails of the wavefunctions cut off the more sharply the higher their angular momentum. We should also expect the effective radius to increase as the deuteron energy decreases because the increasingly important Coulomb effect on the proton will make it profitable for the neutron to attach further out on the tail of what is to be its own wavefunction. The situation will be complicated by the other Coulomb effect on the proton, namely its simple deflection. This will tend to move the structure in the stripping patterns to larger angles and so tend to simulate a decreasing radius of attachment.

CORRESPONDENCE

Interactions of Antiprotons in Nuclear Emulsion

By G. B. Chadwick and P. B. Jones
Clarendon Laboratory, Oxford

[Received August 27, 1958]

Some preliminary results have been obtained from observations on the interaction of antiprotons in a stack of 160 pellicles of Ilford G.5 nuclear emulsion each 10 in. × 8 in. × $600\,\mu$ exposed to the January 1958 antiproton beam of the Bevatron at Berkeley. The flux of antiprotons, integrated over the time of the irradiation was $10\ \text{cm}^{-2}$. The background of minimum ionizing particles, 80% μ-mesons, was $1{\cdot}5 \times 10^5\ \text{cm}^{-2}$. The antiprotons were found by scanning along a line 1·5 cm from the side of the stack in which the beam entered. Tracks with normalized blob density in the range 1·5–1·8 were followed in to the point of interaction.

The energy of the antiproton beam, at the scanning line, was found to be 235 ± 10 Mev, determined from the residual range distribution for those antiprotons which come to rest and produce a capture star with $\geqslant 1$ prong. From this range distribution and from the distribution of the number of minimum ionizing particles produced by capture stars having no visible nuclear excitation, we conclude that 7% of the tracks followed were protons. We estimate that about three antiprotons come to rest and produce a capture star with no visible prongs, compared with 84 which give $\geqslant 1$ prong.

In the energy range 100–235 Mev we have observed 73 interactions in a total of 15·32 metres of antiproton track. This corresponds to a mean free path, for absorption, charge exchange and inelastic scattering by the complex nuclei, of $21{\cdot}0^{+2\cdot8}_{-2\cdot2}$ cm.

Two elastic scattering events with free protons were found, in agreement with the cross section of 41^{+10}_{-7} mb for this process in the energy interval 30–215 Mev found by Agnew *et al.* (1958) using a propane bubble chamber. Elastic scattering of antiprotons by the complex nuclei was observed in the energy range 100–235 Mev for scattering angles $\theta > 10^\circ$ in the laboratory system. In 15·32 metres of antiproton track six events were observed in the interval $12^\circ < \theta < 24^\circ$ and one event was observed with $\theta > 24^\circ$. Glassgold (1958) has shown that the model of the nucleon–antinucleon interaction proposed by Teller (1956) may be investigated by measurement of the elastic scattering cross section for $\theta > 24^\circ$. Combining our data with the results of Goldhaber and Sandweiss (1958) gives two such scatters in a total of 53·3 metres of antiproton track. Comparison with the predictions given in table 3 of the paper by Goldhaber and Sandweiss then suggests that the real part of the antiproton-nucleus optical model potential is not large and negative in sign.

Eighty-two capture stars produced by antiprotons coming to rest were examined, and all light tracks with normalized blob density $b^* < 2{\cdot}0$ and length $> 3{\cdot}0$ mm per plate were identified by measurements of b^* and of the multiple Coulomb scattering. This solid angle implies that 0·20 of all such particles emitted will be identified. A total of 32 tracks was identified. Of these, two were K-mesons of 151 and 148 MEV respectively. Both came to rest in the stack and were further identified by measurements of normalized grain density and residual range. One produced a capture star with a secondary π-meson, and we assume it to be a K^--meson. The other produced no visible secondary particle, but ended 2 microns from the surface of the plate. Careful examination of both parent stars revealed no further charged strange particles.

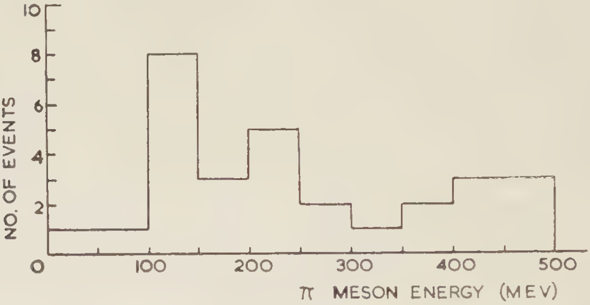

Energy spectrum of π-mesons from antiproton annihilations at rest in nuclear emulsion. Only flat tracks were identified and the energies determined by multiple Coulomb scattering.

The $\pi^{\pm}$-meson energy spectrum found is shown in the figure. The π-mesons have an average energy of 245 MEV. Comparison with the spectrum found by Barkas *et al.* (1957) shows that in our case there are more particles of higher energy and some suggestion that these form a distinct group. The possibility of such a π-meson spectrum has been suggested by Koba and Takeda (1958).

Goldhaber *et al.* (1957) have pointed out that the nuclear excitation in an antiproton annihilation star is a qualitative measure of the absorption radius. In the table the excitation is compared for antiproton capture stars with more than one prong and for interactions of fast antiprotons in the energy ranges 0–100 MEV and 100–235 MEV. Both the excitation and the multiplicity of direct interaction products are seen to be independent of antiproton kinetic energy. The results clearly indicate a larger absorption radius for the annihilation of antiprotons captured in Bohr orbits.

	Capture stars more than one prong	Fast $\bar{p}$ (0–100 MeV)	Fast p (100–235 MeV)
Number of events	45	11	41
Average number of particles of range $>2\cdot0$ mm	1·42	2·00	2·00
Average number of particles of range $<2\cdot0$ mm	2·04	3·54	3·49
Average total energy per star for particles of range $<2\cdot0$ mm	17·6 MeV	33·4 MeV	34·2 MeV

ACKNOWLEDGMENTS

We should like to thank Professor D. H. Wilkinson, F.R.S., for discussions on this work, Dr. E. J. Lofgren and Professor G. Goldhaber for making the antiproton beam of the Bevatron available to us, and Professor M. F. Kaplon for making the irradiation. We are indebted to our scanners, Mrs. G. Lowe and Miss J. A. Petts for finding most of the events. G. B. Chadwick would like to thank the Shell Petroleum Company, and P. B. Jones the Department of Scientific and Industrial Research and the Royal Commissioners for the Exhibition of 1851 for Studentships.

REFERENCES

AGNEW, L., ELIOFF, T., FOWLER, W. B., GILLY, L., LANDER, R., OSWALD, L., POWELL, W., SEGRE, E., STEINER, H., WHITE, H., WIEGAND, C., and YPSILANTIS, T., 1958, *Phys. Rev.*, **110**, 994.

BARKAS, W. H., BIRGE, R. W., CHUPP, W. W., EKSPONG, A. G., GOLDHABER, G., GOLDHABER, S., HECKMAN, H. H., PERKINS, D. H., SANDWEISS, J., SEGRE, E., SMITH, F. M., STORK, D. H., VAN ROSSUM, L., AMALDI, E., BARONI, G., CASTAGNOLI, C., FRANZINETTI, C., and MANFREDINI, A., 1957, *Phys. Rev.*, **105**, 1037.

GLASSGOLD, A. E., 1958, *Phys. Rev.*, **110**, 220.

GOLDHABER, G., KALOGEROPOULOS, T., and SILBERBERG, R., 1957, *UCRL Report*, 3914.

GOLDHABER, G., and SANDWEISS, J., 1958, *Phys. Rev.*, **110**, 1476.

KOBA, Z., and TAKEDA, G., 1958, *Progr. theor. Phys., Osaka*, **19**, 269.

TELLER, E., 1956, *Proceedings of the 6th Rochester Conference* (New York: Interscience Publishers Inc.).

BOOK NOTICES

L'Origine Photochimique de la Vie. By A. DAUVILLIER. (Paris: Masson et Cie.) [Pp. 214 + 27 figures.] 1300 fr.

Some Aspects of Multivariate Analysis. By S. N. ROY. (New York: John Wiley & Sons, Inc.; London: Chapman & Hall.) [Pp. vi + 214.] 64*s*.

Introduction to Multivariate Statistical Analysis. By I. W. ANDERSON. (New York: John Wiley & Sons, Inc.; London: Chapman & Hall.) [Pp. xii + 374.] 100*s*.

The Physicist's Conception of Nature. By W. HEISENBERG. (London: Hutchinson & Co. (Publishers) Ltd.) [Pp. 192.] 16*s*.

Chemistry of the Rare Radioelements. By K. W. BAGNALL. (London: Butterworths Scientific Publications.) [Pp. x + 177.] 30*s*.

The Development and Meaning of Eddington's Fundamental Theory. By NOEL B. SLATER. (Cambridge: University Press.) [Pp. xi + 298.] 40*s*.

White Dwarfs. By E. SCHATZMAN. (Amsterdam: North-Holland Publishing Co.) [Pp. 180.] 19 guilders.

Health Physics. Edited by KARL Z. MORGAN. (London: Pergamon Press Ltd.) [Pp. 95 + vi.]

An Introduction to Combinatorial Analysis. By JOHN RIORDAN. (New York: John Wiley & Sons, Inc.; London: Chapman & Hall.) [Pp. x + 244.] 68*s*.

Introduction to Difference Equations. By SAMUEL GOLDBERG. (New York: John Wiley & Sons, Inc.; London: Chapman & Hall.) [Pp. xii + 260.] 54*s*.

Reports on Progress in Physics. Editor A. C. STICKLAND. (London: The Physical Society.) [Pp. 383.]

Research Management. By The Industrial Research Institute. (New York: Interscience Publishers Ltd.) [Pp. 64.] Subscription $7.50 per year.

The Gyroscope Theory and Applications. By JAMES B. SCARBOROUGH. (New York: Interscience Publishers.) [Pp. xii + 257.] $6.50.

Electromagnetic Isotope Separators and Applications of Electromagnetically Enriched Isotopes. Edited by J. KOCH. (Amsterdam: North-Holland Publishing Company.) [Pp. xi + 315.] 26.50 guilders.

Transistor Technology. Edited by H. E. BRIDGERS, J. H. SCAFF and J. N. SHIVE. (London: D. Van Nostrand Company Ltd.) [Pp. xxxvii + 661.] 131*s*. 6*d*.

Il Tempo. Edited by ENRICO CASTELLI. (Milan: Cedam-Casa Editrice Dott. Antonio Milani.) [Pp. 248.] L. 2000.

Science Students' Guide to the German Language. By Miss A. F. CUNNINGHAM. (Oxford: University Press.) [Pp. xiii + 186.] 12*s*. 6*d*.

Theory of Dielectrics. Dielectric Constant and Dielectric Loss. By H. FROHLICH. (Oxford: University Press.) [Pp. vii + 192.] 30*s*.

Thermodynamics of One-Component Systems. By WILLIAM N. LACEY and BRUCE H. SAGE. (New York: Academic Press Inc.) [Pp. xi + 376.] $8.00.

Theoretical Physics. By F. W. CONSTANT. (Massachusetts: The Addison Wesley Publishing Company Inc.) [Pp. xiii + 364.] 64*s*.

[*The Editors do not hold themselves responsible for the views expressed by their correspondents.*]

Fig. 1

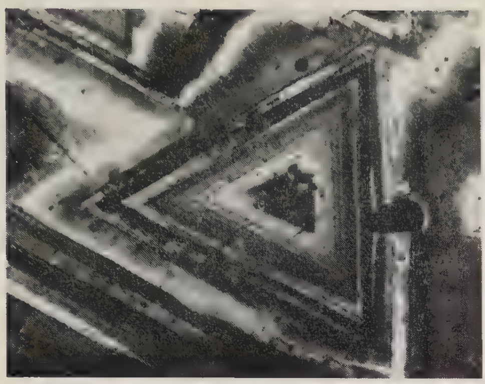

A growth pyramid showing the terrace. High dispersion multiple-beam interferogram (×13·75).

Fig. 2

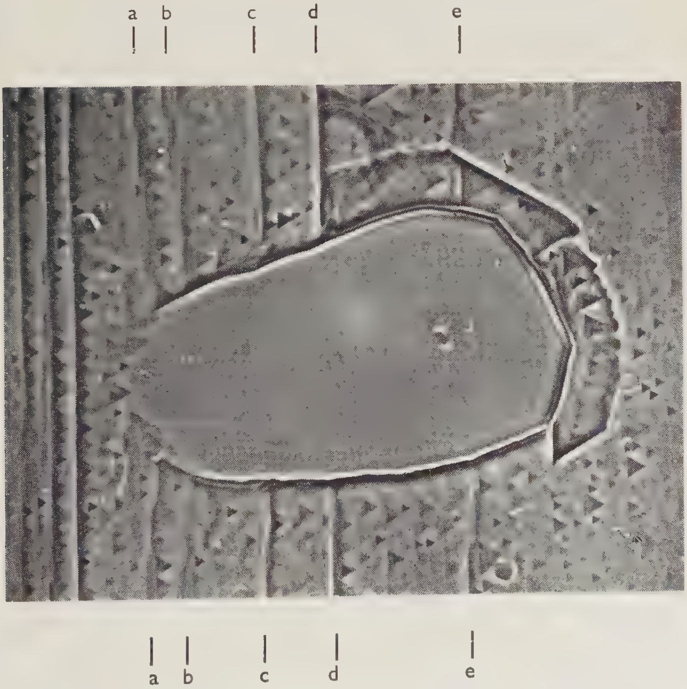

The same terrace at higher magnification. Phase contrast illumination (×133·75).

Fig. 3

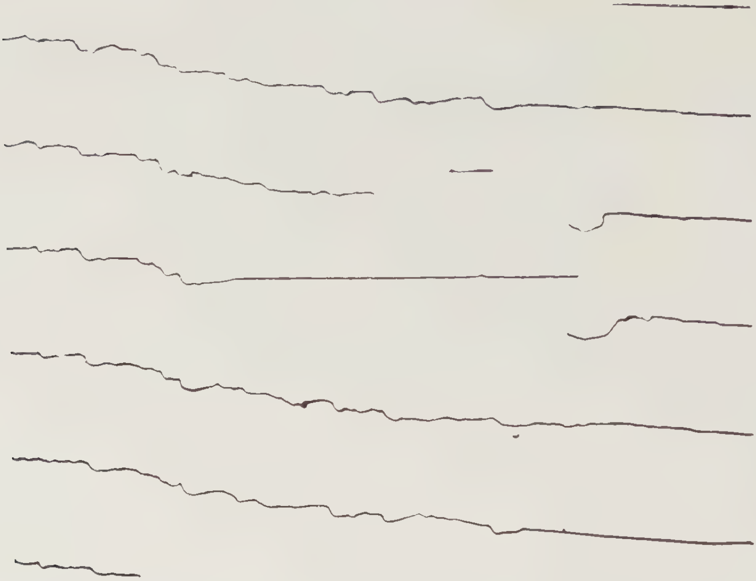

Multiple-beam fringes across the terrace (×106·75).

Fig. 4

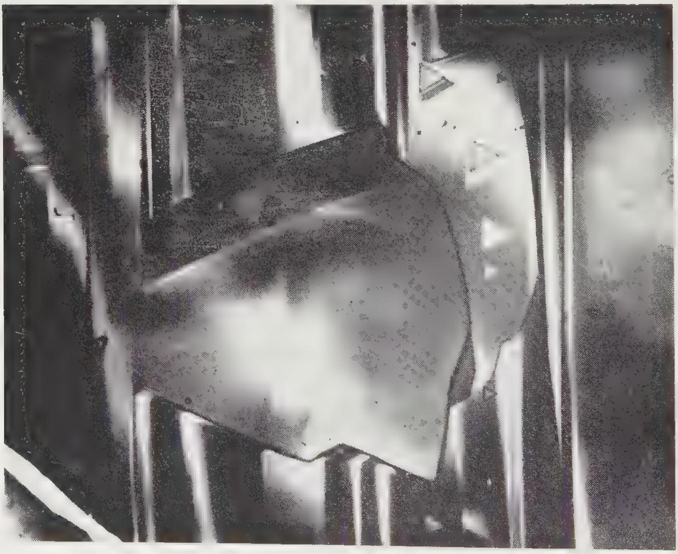

Another terrace. High dispersion multiple-beam interference (×226·75).

Fig. 1

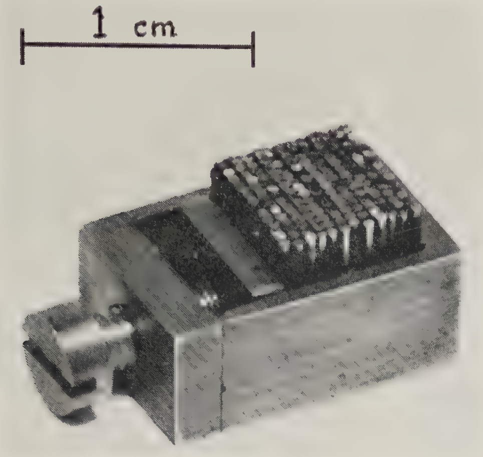

The domain model (12 × 15 magnetized wires).

Fig. 2

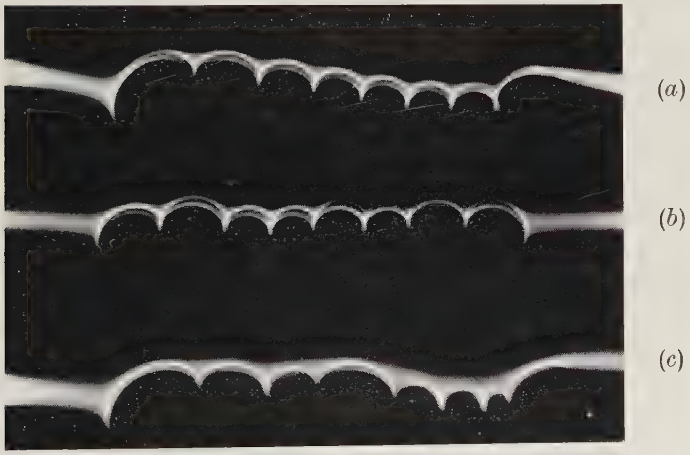

Shadow patterns from (*a*) a single row, (*b*) 2 rows, (*c*) 12 rows, each consisting of 15 magnetized wires. The direction of the electron beam is perpendicular to a line linking the magnetic poles in any one row.

Fig. 3

Shadow patterns from (*a*) a single row, (*b*) 2 rows, each consisting of 15 magnetized wires. The direction of the electron beam is parallel to a line linking the magnetic poles in any one row.

Fig. 4

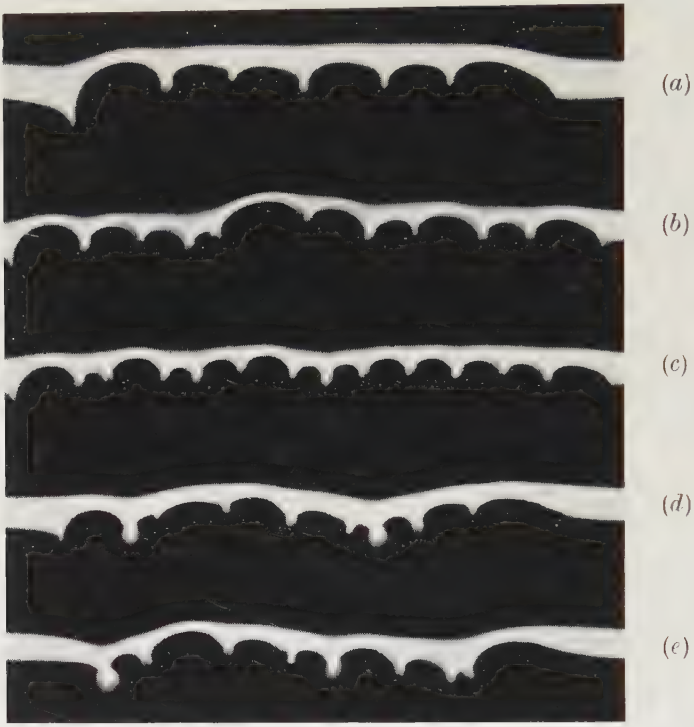

Shadow patterns from a 12 × 15 model rotated through various angles about an axis perpendicular to the direction of the electron beam, (*a*) 0°, (*b*) 30°, (*c*) 50°, (*d*) 75°, (*e*) 90°.

Fig. 5

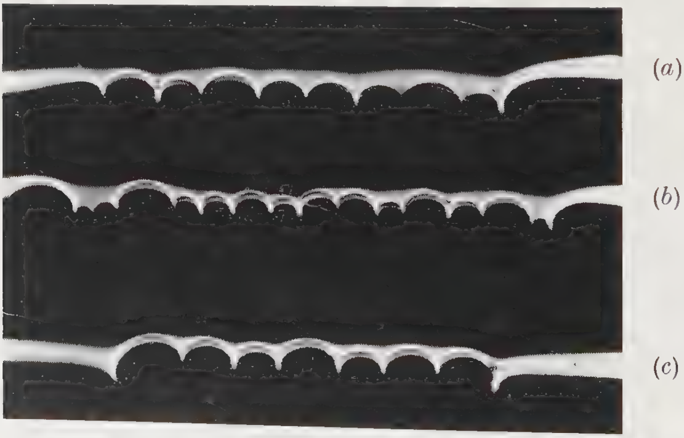

Shadow patterns from a 'peripheral' model rotated through various angles about an axis perpendicular to the electron beam, (*a*) 0°, (*b*) 45°, (*c*) 90°.

Fig. 6

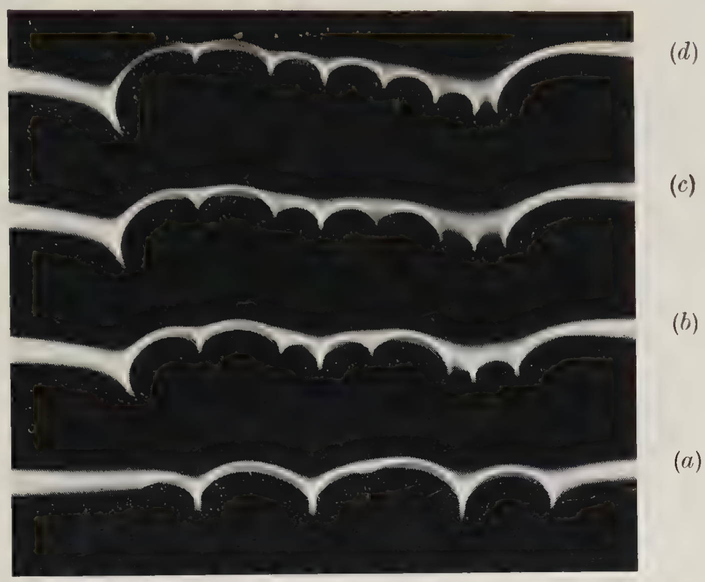

The effect on the shadow pattern of altering the spacing of the magnets in one of the inner rows of the extensive model. The angle of grazing incidence is (*a*) 0°, (*b*) 10°, (*c*) 20°, (*d*) 30°.

Fig. 7

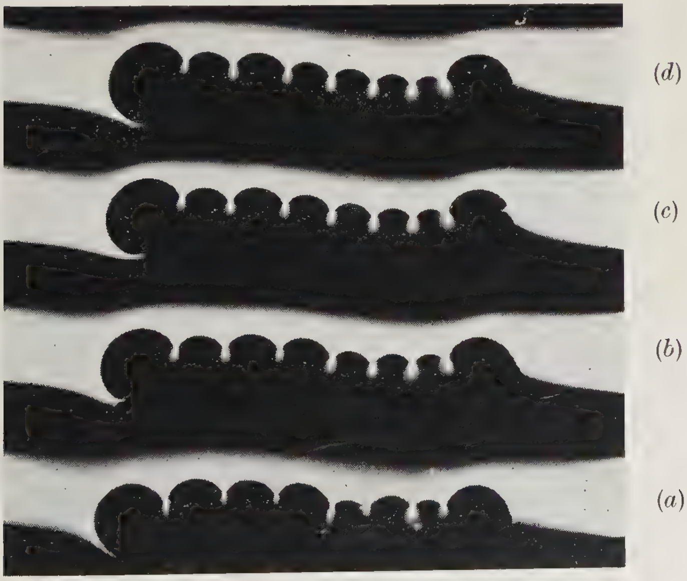

The effect of changing the (glancing) angle of incidence on the regular extensive model, (*a*) 0°, (*b*) 10°, (*c*) 20°, (*d*) 30°.

Fig. 8

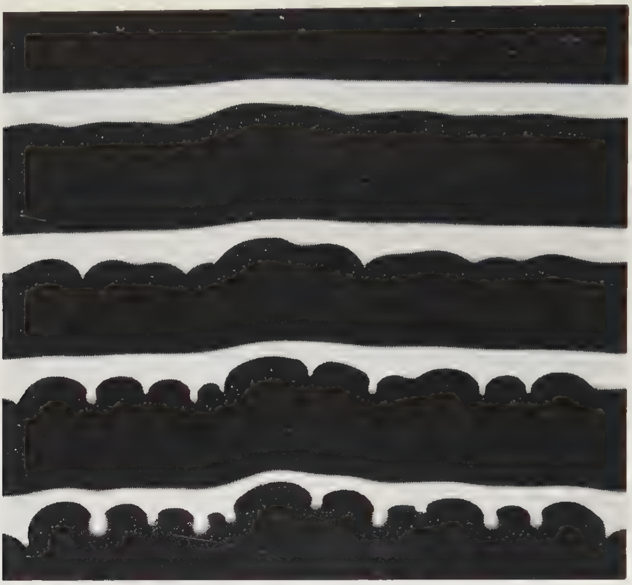

Patterns taken for various, progressively increasing, distances between the axis of the electron beam and the face of the extensive model. The uppermost photograph is taken at the greatest distance.

Fig. 9

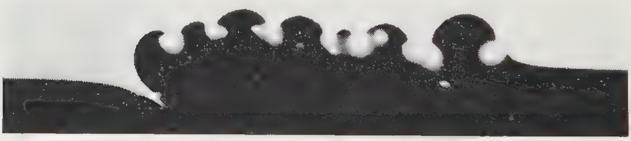

Additional features in the shadow pattern (spots and streaks) found when a large part of the electron beam is intercepted by the model.

Fig. 10

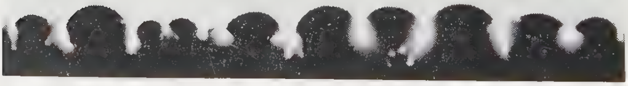

Shadow patterns from cobalt showing additional features.

Fig. 1

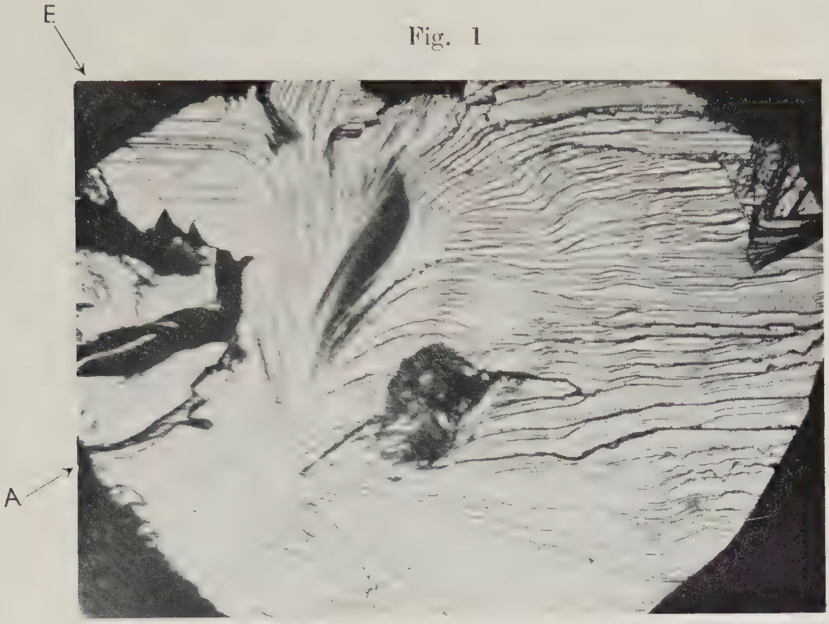

Photomicrograph of a type I cleavage surface. ×45.

Fig. 2

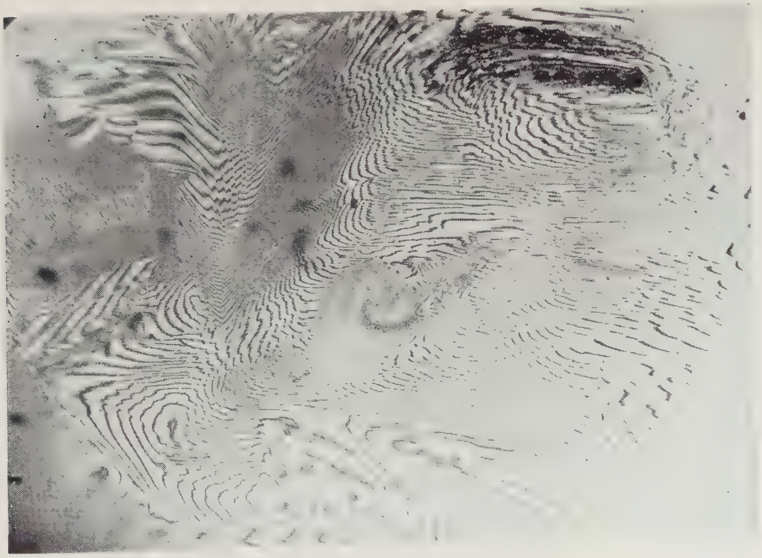

Reflection interferogram over the surface of fig. 1. ×45.

Fig. 3

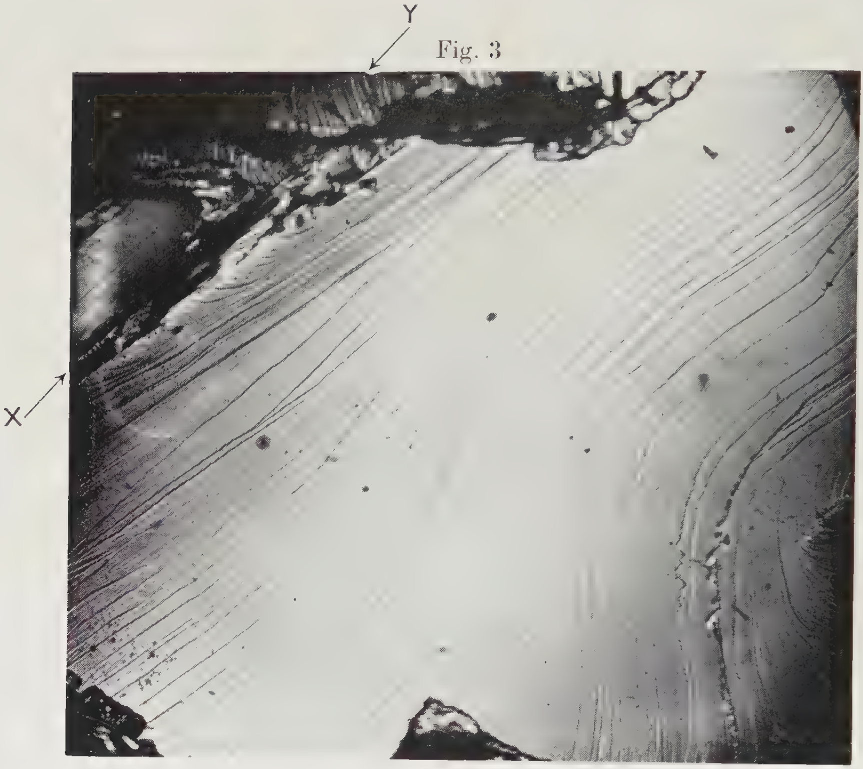

Photomicrograph of a type II cleavage surface. ×28.

Fig. 4

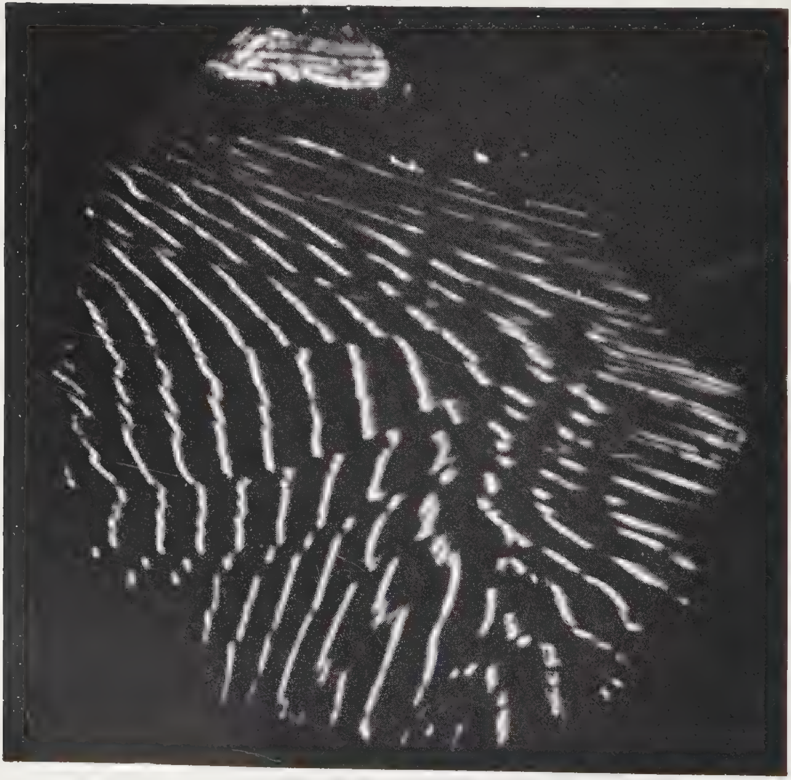

Transmission interferogram over the surface of fig. 3. ×28.

Fig. 6

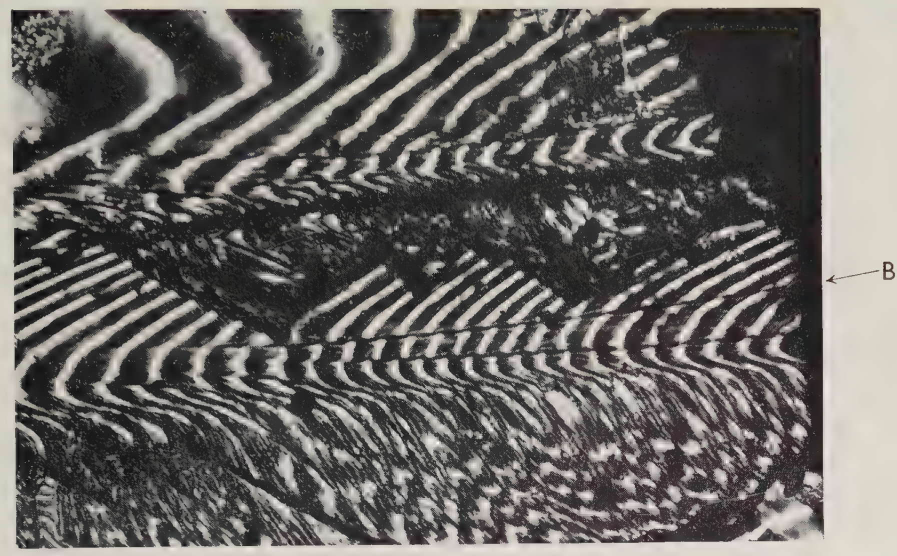

Transmission interferogram of part of a type I cleavage surface. The step height along the line B varies from zero to 2800 Å over a distance of 1·0 mm. × 100.

Fig. 7

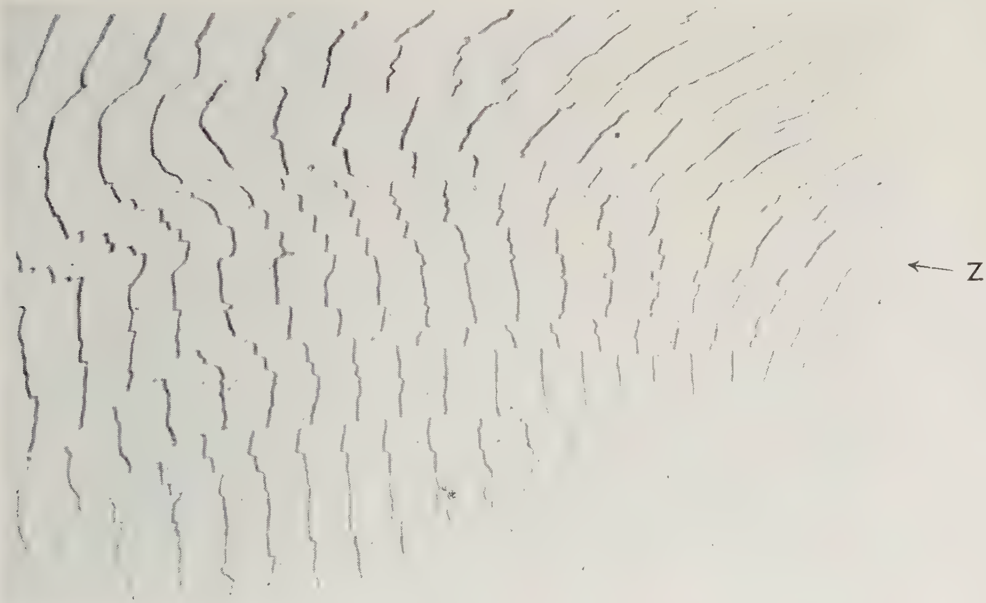

Reflection interferogram of part of a type II cleavage surface. The step height along the line Z varies from zero to 1100 Å over a distance of 0·4 mm. × 125.

Fig. 8

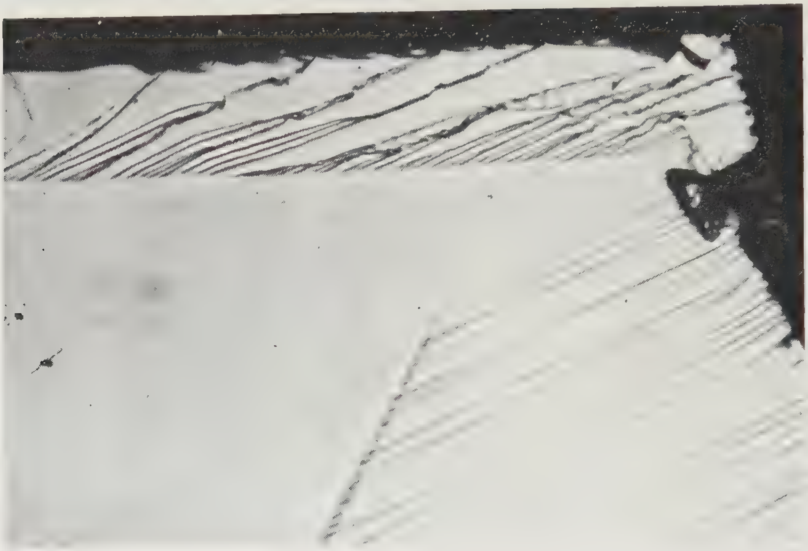

Photomicrograph of a type II cleavage surface showing 'river pattern' markings breaking out from a line boundary. ×120.

Fig. 9

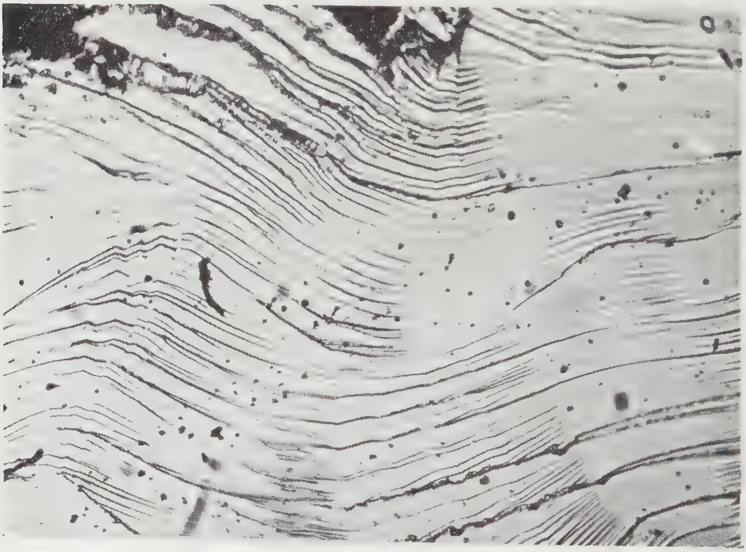

Photomicrograph of a type I cleavage surface showing systems of 'river patterns' beginning on curved line boundaries. ×50.

Fig. 10

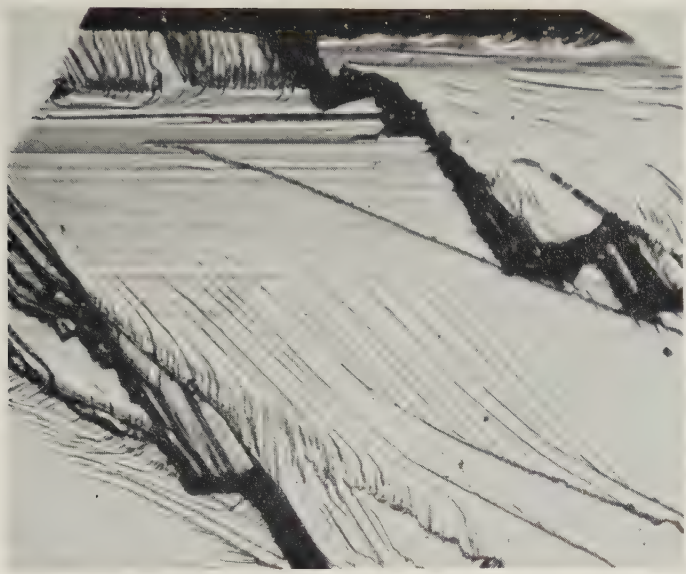

Photomicrograph of a type I cleavage surface showing 'river lines' beginning on separate line boundaries. ×120.

Fig. 11

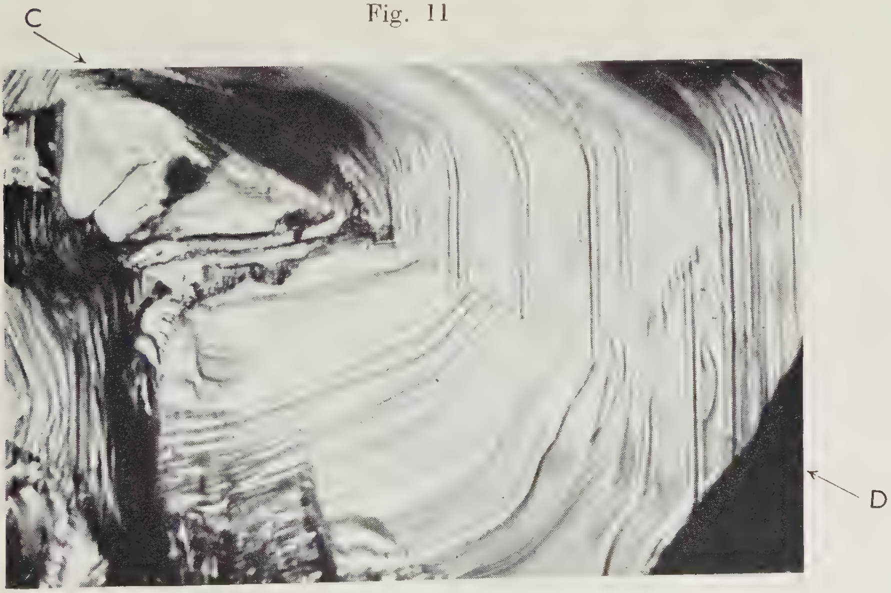

Photomicrograph of a type I cleavage surface showing a line boundary CD cutting across the 'river lines'. ×120.

Fig. 12

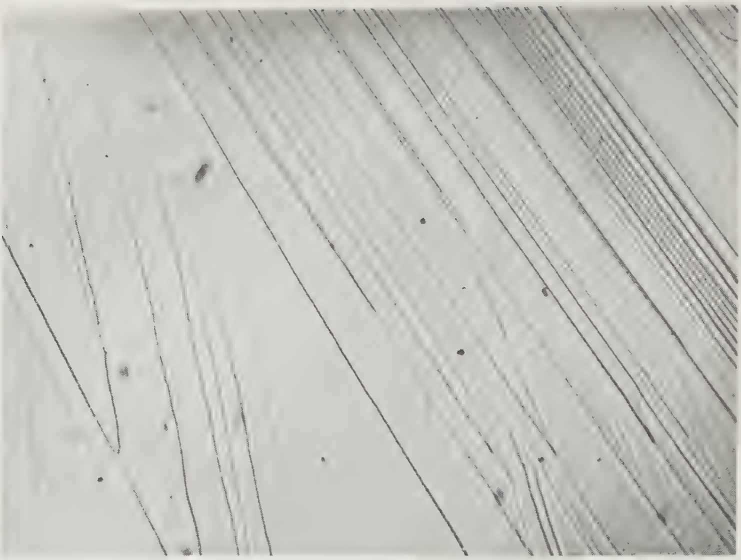

Photomicrograph of a type II cleavage surface showing straight cleavage lines. ×120.

Fig. 13

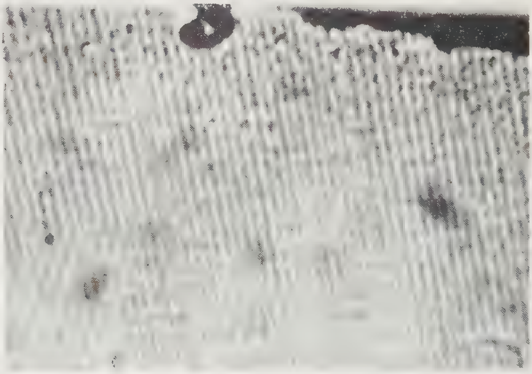

Photomicrograph of a section of the cleavage surface of a type II counting diamond showing straight cleavage lines. ×300.

Fig. 14

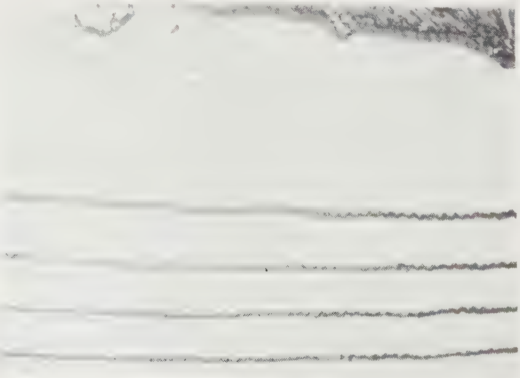

Reflection interferogram over the surface of fig. 13. ×300.

Fig. 4

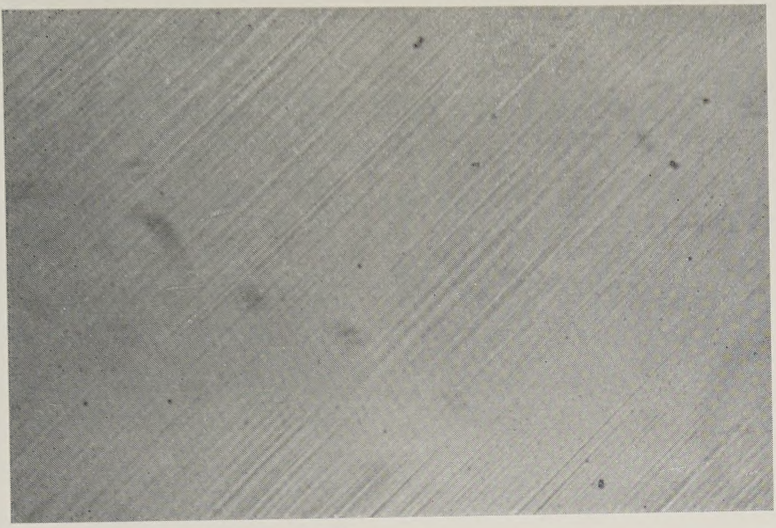

(*a*)

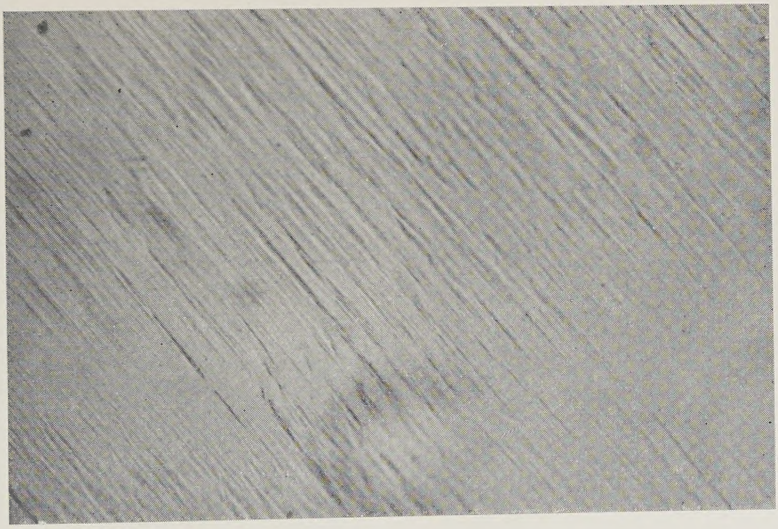

(*b*)

Slip markings observed on different regions of specimen M. (*a*) Slip bands having the appearance of tensile slip bands; (*b*) slip bands having the appearance of fatigue slip bands.

Fig. 7

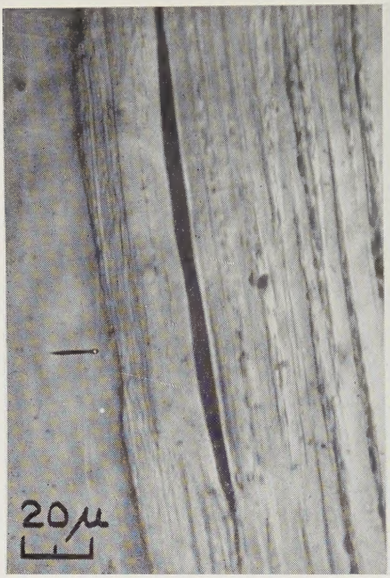

Crack in a slip band in copper fatigued for $1{\cdot}8\times10^4$ cycles in air and then pulled.

Fig. 8

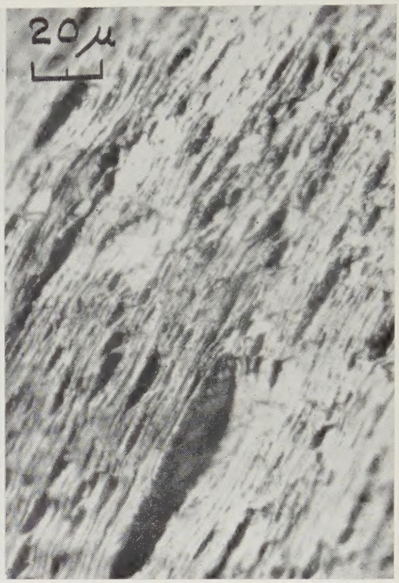

Cracks in slip bands in copper fatigued to fracture in vacuum and then pulled.

Fig. 9

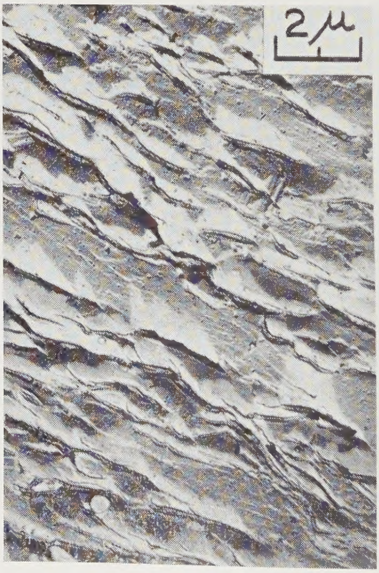

Electron micrograph showing intrusions in copper.

Fig. 10

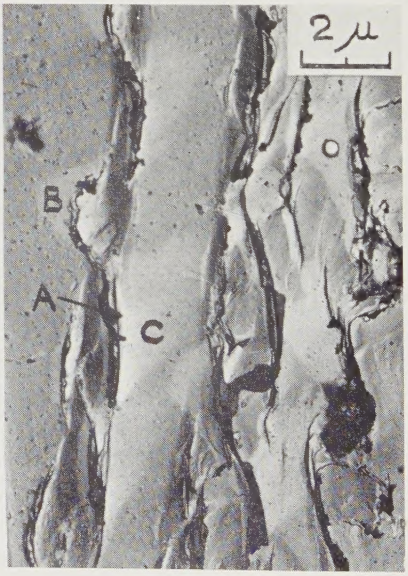

Electron micrograph showing extrusions and intrusions in copper. Extrusions cast shadows to the left as at B and intrusions to the right as at C.

Fig. 11

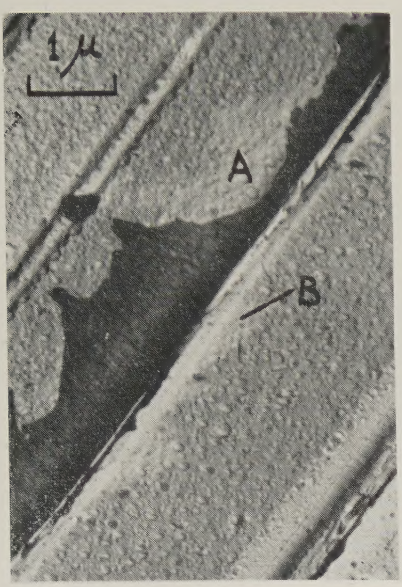

Electron micrograph showing intrusion and extrusion in copper. The intrusion casts a shadow at A and the extrusion at B.

Fig. 12

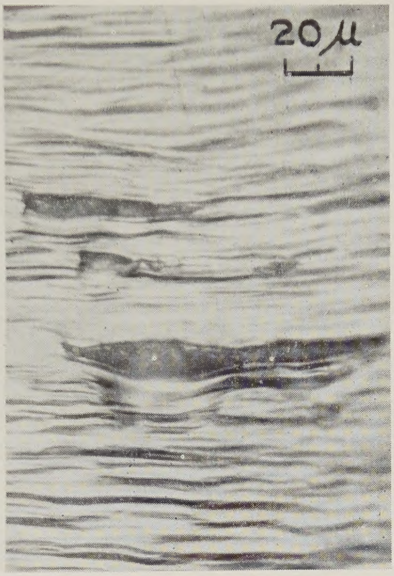

Cracks in slip bands in aluminium fatigued in air and then pulled.

Fig. 13

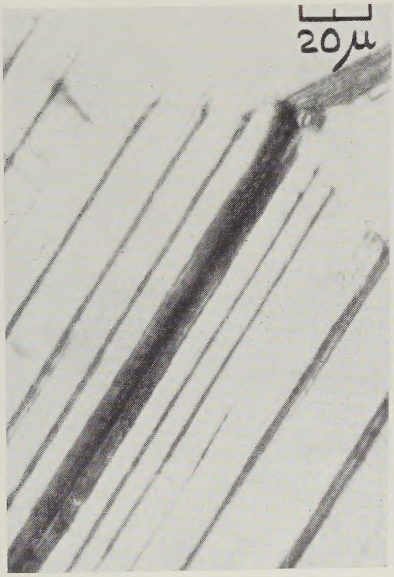

Slip bands and extrusion in gold fatigued for 3×10^4 cycles.

Fig. 14

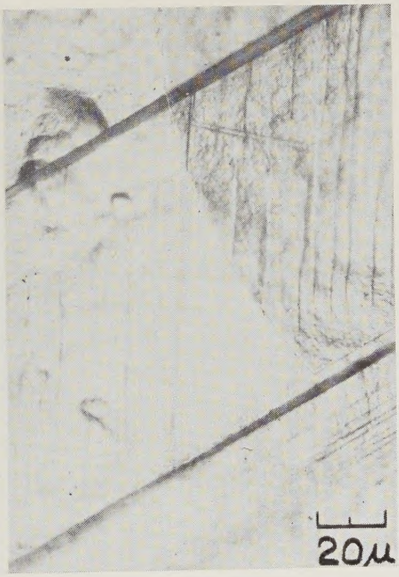

Cracks at twin boundaries in gold fatigued for 3×10^4 cycles, electropolished and pulled.